SYNTHESIS, CHARACTERIZATION AND 3D PRINTING OF LINEAR AND STAR-SHAPED POLY(PROPYLENE FUMARATE) FOR MEDICAL APPLICATIONS

A Dissertation

Presented to

The Graduate Faculty of The University of Akron

In Partial Fulfillment

of the Requirements for the Degree

Doctor of Philosophy

Yuanyuan Luo

August, 2019

SYNTHESIS, CHARACTERIZATION AND 3D PRINTING OF LINEAR AND STAR-SHAPED POLY(PROPYLENE FUMARATE) FOR MEDICAL APPLICATIONS

Yuanyuan Luo

Dissertation

Approved:	Accepted:
Advisor Dr. Matthew L. Becker	Department Chair Dr. Tianbo Liu
Committee Member Dr. Bryan Vogt	Dean of the College Dr. Ali Dhinojwala
Committee Member Dr. Eric J. Amis	Dean of the Graduate School Dr. Chand Midha
Committee Member Dr. Toshikazu Miyoshi	Date
Committee Member Dr. Chrys Wesdemiotis	

DEDICATIONS

This dissertation is dedicated to my lovely family, my teachers and all my friends who have helped, supported and encouraged me during my journey to science.

ABSTRACT

Advancements in additive manufacturing, or more commonly known as 3D printing techniques, and the development in synthetic polymers are enabling the fabrication of patient-matched medical devices. These are especially thriving in the regenerative medicine field where products with complex shapes are involved, such as cranial facial bone defect repair. However, before the release of such medical devices on market, they must be cleared by the Food and Drug Administration (FDA). The consistency of the starting material and final product built from 3D printing was incorporated into FDA's concern to guarantee the safety and effectiveness of a medical device. Such material consistency requires material specifications, which usually depends on the type of materials and 3D printing techniques. For the example of polymers, the purity, molecular weight, molecular mass distribution ($Đ_m$), glass transition temperature properties are generally required. The failing to reliably and reproducibly produce a material may cause final device failure in tests like mechanical, biocompatible and/or pre-clinical animal studies, let alone to pass FDA regulations. Poly(propylene fumarate) (PPF) is a non-toxic, amorphous, degradable, crosslinkable polyester, with tunable mechanical and degradation properties for regenerative medicines. However, previous academic researchers reported some limitations of using 3D printed PPF for medical applications and research on these polymers had stopped at the stage of small animal studies. The drawbacks mainly came

from unreliable molecular properties (e.g., $Đ_m$>2) and low yield (e.g., 35%) from traditional synthetic methods.

Herein, a reaction system was developed as shown in this dissertation to generate PPF from ring-opening copolymerization (ROCOP) of maleic anhydride and propylene oxide followed by a base catalyzed isomerization reaction. Then a continuous improvement in the yield (e.g., 65%-90%), a more reproducible synthesis (up to 1kg/batch), a better control over the molecular mass distribution (e.g., 1.1-1.6) of PPF with various functionalities were achieved. The following sections start with the story of the first attempt to synthesize 3D printable PPF using a ROCOP method with detailed chemical and physical characterizations on these PPF materials (Chapter III). Then, the viscosity evaluations and 3D printing of these PPF based resins were further explored, followed by mechanical tests (Chapter IV). These results demonstrated the potential of using such PPF-based materials in high resolution 3D printing techniques, such as continuous digital light processing (cDLP) for bone repair applications. The most recent innovation in synthesis of star-shaped PPF made it possible to efficiently obtain higher molecular mass PPF, which also showed lower viscosity than their linear analogues. These significant improvements in star-shaped PPF over linear PPF analogs from synthetic speed, viscosity for 3D printing to mechanical properties were later disclosed (Chapter V).

Currently, 3D printing of ROCOP synthesized PPF-based degradable resins with less solvent input, available functionalities for biological cues are possible, bringing a relatively wide range of mechanical and degradation properties of printed products. This work has been a preliminary study that has helped to gradually improve PPF properties to aid in 3D printing for patient and defect-matched regenerative medicine.

ACKNOWLEDGEMENTS

I would like to express the deepest gratitude to my research advisor, Dr. Matthew L. Becker, for all his unique insight in material science, constant, valuable and patient guidance for my research. Not only has he provided me with plenty of inspiration and support in scientific research, but also has he set a good example as a role who has been wearing many hats, as a diligent research investigator, an active and team player, a dedicated family member, a reliable community volunteer, etc. It's my great honor to have had the opportunity to work in the research I'm interested in with such an optimistic and determined professor. The interactions with him has gradually shifted my insight in philosophy and will continuously influence my future decisions in career and life.

I also would like to express big thank you to my dissertation committee: Dr. Bryan Vogt, Dr. Eric J. Amis, Dr. Toshikazu Miyoshi and Dr. Chrys Wesdemiotis, for their internets in my research, concerns and suggestions for my study. Without their time and efforts to understand my research and help to improve my work, this dissertation could not have been completed in time.

Starting a challenging research in a brand-new field at the beginning of graduate school, I would like to extend my thanks to all former and current students and researchers at The Becker Lab and The Dean Lab at The Ohio State University , for their sharing of technique research knowledge and skills for a wet-lab beginner, and continuous discussion

and encouragement during my research journey. I also want to thank John Page for his suggestions in GPC tests, Dr. Sahar Sallam and Dr. Jacob Alan Hill for sharing their knowledge in MALDI characterization, Dr. Paul Shiller for always being there, supporting my journey to rheology from initial experimental design to valuable scientific discussions, Dr. Jianning Liu, Yexin Zheng and Siqi Wu for training and help with mechanical tests, and Dr. Gaëlle Le Fer for sharing her skills and passion in polymer chemistry.

Last but not the least, my deepest thanks and love should go to my parents, who have moved our home address to achieve a better education for me three times during my childhood. I want to thank them for their endless understanding, trust, support, inspiration and sacrifice during my growing-up, especially this challenging journey in graduate school abroad. They told me the importance of education by practical action and formed my personality of persistence, optimism and responsibility.

TABLE OF CONTENTS

Page

LIST OF FIGURES

Figure Page

LIST OF SCHEMES

Scheme Page

LIST OF TABLES

Table Page

CHAPTER I

INTRODUCTION

1.1 Medical Applications Using 3D printing Techniques

1.1.1 What is 3D printing?

Additive manufacturing (AM), or more commonly known as 3D printing, is a type of fabrication process (shown in Figure 1.1.). The International Organization of Standardization (ISO) and The American Society for Testing and Materials (ASTM) define AM as "a process of joining materials to make parts from 3D model data, usually layer upon layer, as opposed to subtractive and formative manufacturing methodologies"[1]. Clearly, 3D printing is different from traditional subtractive methods, fabricating a product by removing excess material from a bulk material via milling, drilling and cutting methods[2] and formative manufacturing methods, using high volume of material and molds to fabricate an object, like injection molding and casting.[2-4] Each of these three manufacturing processes has its own advantages over the other depending on the size, complexity in 3D architecture, and material requirements for the final product. As 3D printing makes an object in a layer-by-layer format, subtractive manufacturing wins in producing larger

volume products with simple part details; and formative manufacturing may dominate in fabricating one piece of large product out of different materials at one time from molds at low cost. However, compared to subtractive manufacturing method, 3D printing can benefit in fabricating intricate and hollow-interior products with highly details in a cost-effective style, e.g., leaving fewer waste materials. 3D printing also has more flexibility in switching designs of products at less cost with computer-aided design (CAD), instead of spending more time and money on making lots of molds for product improvement via a formative manufacturing process.

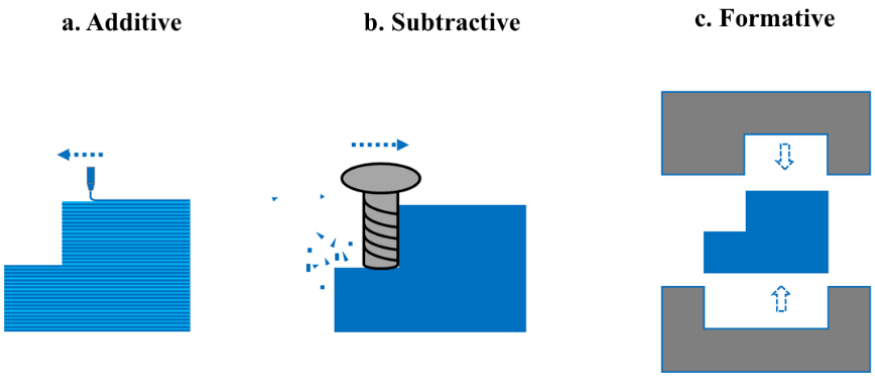

Figure 1.1. Three main types of manufacturing processes. a. additive manufacturing method where an object is built in a "layer-by-layer" style. b. subtractive manufacturing method where an object is built via removing excess material from a bulk object by machining. c. formative manufacturing method where an object is formed inside pre-fabricated molds

Compared with conventional manufacturing processes, 3D printing process better fits in efficiently and more cost-effectively fabricating products where precise control of internal architecture (like pore size, tortuousness, connectivity and porosity) and/or complex irregular exterior shape are required.[2] With the generation of a complex 3D model from either CAD or scanning of an object, slicing this 3D model into layers with a slicing software, printing of such a complex 3D object can be completed automatically using a 3D printer. For building of complex architecture products, 3D printing technology can not

only provide products with better resolution and matching with their designs but also can improve the fabrication efficiency as no extra molds or tooling processes are required.[2] For example, in 2013, the National Aeronautics and Space Administration (NASA) successfully built a rocket engine injector using 3D printing technique with two printed parts instead of manufacturing and assembling of 115 parts using conventional methods. Fabrication blades for gas turbines using a 3D printing method can reduce the manufacturing time from 44 weeks in a traditional fabrication method to four weeks.[5]

Since the invention of the 1st 3D printing system (a stereolithography apparatus developed by Charles W. Hull to fabricate a 3D object) in 1986[6, 7], modern 3D printing techniques have expanded rapidly during the past three decades. This change is highly dependent on the continuous development and breakthroughs in material science, 3D imaging, modeling and designing techniques, engineering fields, and more communication between researchers in these fields.[8, 9] 3D printing has gained exciting interests in both academic research and industrial applications from automobiles, commercial aerospace, consumer products to customer-specific healthcare sectors.[9-13]

1.1.2 3D printing for customer-matched medical applications

Customer-matched medical products have sprung up like mushrooms during the last two decades with these advancements from 3D printing, medical imaging and modeling techniques.[8, 14] Such applications namely, but not limited to, surgical diagnosing and practices[9, 15], wearable medical devices[9, 16], dental implants[9, 17], craniofacial surgical implants (e.g., periodontal complex regeneration, cranial implant)[11, 18, 19], bone tissue

engineering and regeneration[3, 20, 21], to drug delivery[5, 9, 22, 23], where small to medium size products with personalized designs are of high importance.

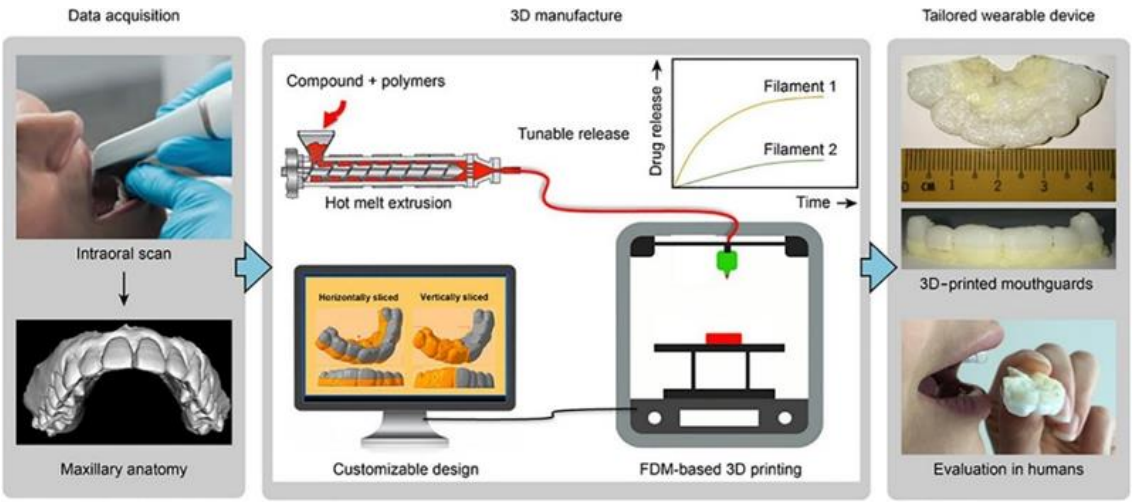

Figure 1.2. General 3D printing flow chart diagram of a wearable customized oral delivery mouthguard in a clinical case[16] Data acquisition, using a digital scanner to scan the customer's maxillary anatomy. 3D manufacture, using computer aided design and modeling software to guide an extrusion-based 3D printer print this product with desired compound. Last, performance evaluation of the customer-matched 3D-printed mouthguard on each customer. (Reprinted from Liang, K.; Carmone, S.; Brambilla, D.; Leroux, J.-C., 3D printing of a wearable personalized oral delivery device: A first-in-human study. *Science advances* **2018,** *4* (5), eaat2544. ©Liang, K.; Carmone, S.; Brambilla, D.; Leroux, J.-C., some rights reserved; exclusive licensee American Association for the Advancement of Science. Distributed under a Creative Commons Attribution NonCommercial License 4.0 (CC BY-NC) http://creativecommons.org/licenses/by-nc/4.0/)

3D printing can provide customer-matched medical devices and/or solutions in a more time efficient and manufacture reproducible style.[3, 5, 9] Surgeons have already embraced the advantages of 3D printing to make anatomical-matched guides, defect-fit tissue and/or organs, which have helped them to practice complex and challenging surgeries with models closer to each patient's case.[9] Surgical models can be used for surgical planning, and decrease the overall surgical complexity and time.[8] 3D printed patient-specific surgical guides can precisely help determine the optimal locations for drilling implants like screws.[15] Such availability to generate surgical models and guides according to each patient via 3D printing techniques has helped improve the overall

operation room success and customer satisfaction, which are significant for the patient's life quality.[14]

3D printed wearable personal devices in dental, hearing aids and drug delivery applications have also rapidly appeared on market. Figure 1.2 showed a general flow chart diagram for fabricating a customer-matched complex product, a mouthguard with sustained drug release capability to treat oral inflammation, and for using an extrusion-based 3D printing method.[16, 23] This process involved three steps, from the 3D digital data acquisition of the customer's maxillary anatomy using an intraoral scanner, computer aided design (CAD) for 3D printing, and final evaluation of the drug-loaded mouthguard on the release profile on human beings. As each person has a unique maxillary anatomy, 3D printing is versatile in providing mouthguards with more anatomic-matched characteristics according to these scanned data. What's more, compared to traditional treatment of oral inflammation, periodically applying high-dosed topical solutions or gels on the affected regions, higher treatment efficacy and less side effects can be achieved using this 3D printed drug-loaded mouthguard with sustained drug release profiles.[16]

Many small size tissue injuries can heal spontaneously in human body, while the repair of larger size tissue defects (critical size defect) generally requires external intervention, such as transplantation of a new tissue part to replace, repair the damaged tissue or regenerate functioning tissues[24-26] The shortage of available tissues for transplant[27, 28] remains a challenging in clinical treatment of such large amount loss of tissues due to trauma, diseases and/or aging.[5, 29] This demand on transplantable tissues in a safe, efficacious and cost-effective manner is expected to keep on growing with the continuous increase in global population.[30, 31] Tissue engineering approach tries to face this challenge

with a combination of proper cells, porous scaffolds and bioactive factors to improve, replace the damaged tissue or to regenerate new tissue with desired functions.[25] 3D printing has also penetrated into this area with extensive attentions and practices in embracing the idea behind tissue engineering.[32, 33] Compared to traditional porous scaffold fabrication method, like particulate leaching, solvent casting, gas foaming, electrospinning and freeze drying[2, 26], 3D printed porous scaffolds have better properties in terms of controlling the overall 3D geometry according to CAD designs and well-controlled internal pore characteristics such as pore interconnectivity and pore size to mimic the function of extra cellular matrix.[26, 31] Both of these two factors are essentials for reproducible and predictable scaffold properties and optimal scaffold functions, such as mechanical support or protection, transportation of nutrition, oxygen and waste products for cells to survive.[34] With these advantages over traditional scaffolds fabrications methods, 3D printed porous scaffolds have shown tunable mechanical properties for various hard and soft tissue applications, controllable degradation profiles for tissue regeneration, sustained release of bioactive molecules to guide and accelerate tissue repair with better reproducibility.[14, 35-37] What's more, the current emerging bio-printing technique makes it feasible to directly print complex scaffolds incorporated with cells and bioactive molecules using 3D printable bio-inks, which improves the uniformity of cell distribution throughout the scaffold without the extra cell seeding after scaffold fabrication.[25, 26]

1.1.3 Types of commonly used 3D printing methods and their medical applications

Several 3D printing techniques are currently used in academic and clinical research areas, among which some 3D printed products have received U.S. Food and Drug

Administration (FDA) approval and successfully been transferred into market to enhance human life quality. Based on how two layers are connected during 3D printing, these techniques can be classified into one of three categories which are discussed in detail below.

1.1.3.1 Extrusion-based 3D printing

Fused deposition modelling (FDM), invented in 1988 by Scott Crump who attempted to create a toy for his daughter using a glue gun, is one of the most commonly used and low cost extrusion-based 3D printing techniques[14]. As shown in Figure 1.3a, generally a thermoplastic filament is extruded through a high temperature above the glass transition temperature in a chamber and extruded out of a nozzle.[26] The extruded semi-flowable material is then immediately solidified on the platform (usually set at a lower temperature). The platform under the nozzle can move in the horizontal directions according to computer aided design to achieve the 2D pattern in each layer. After finishing the solidification of one layer, the platform lowers down for the deposition of the next layer on top of the previous layer. This process is then repeated until the completion of the product. Many resorbable polymers or composite materials have been used in preclinical studies using FDM technique to fabricate tissue engineering porous scaffolds and have shown excellent results for bone tissue regeneration *in vivo*.[9, 26, 38] Compared to traditional porous scaffold fabrication methods such as salt leaching, FDM printed 3D scaffolds showed significantly higher stiffness at similar porosity level.[39]

1.1.3.2 Ink-based 3D printing

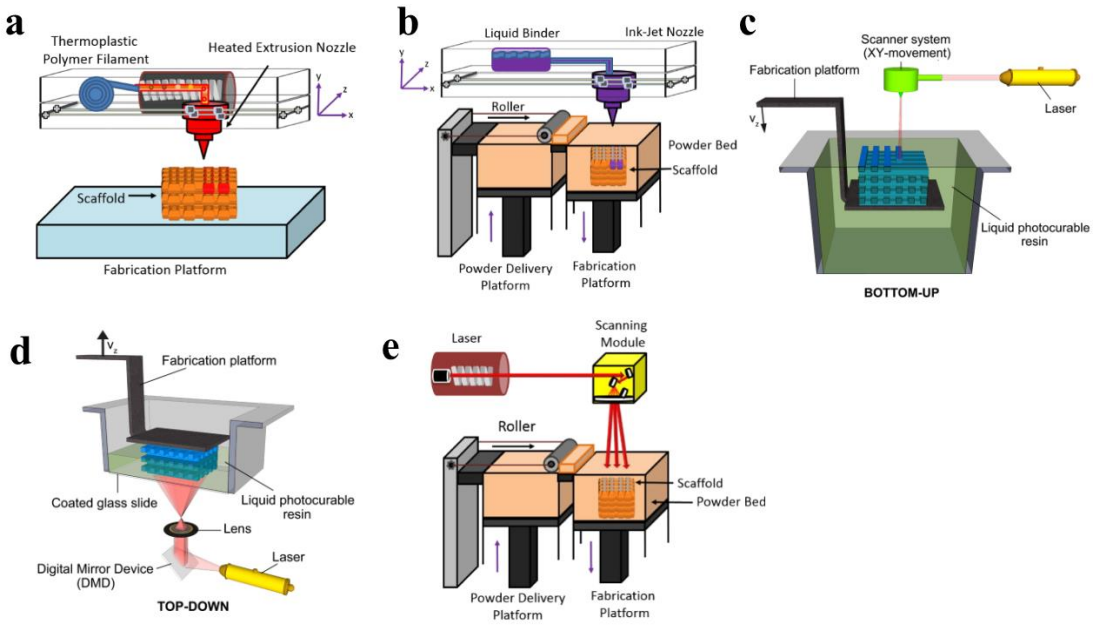

Figure 1.3. Diagrams of 3D printing techniques commonly used in research and clinical medical applications. a, extrusion-based 3D printing method known as fused deposition modeling.[26] b, One type of ink-based based 3D printing method, known as powder-binder 3D printing.[26] c, One type of light-based 3D printing method known as stereolithography.[40] d, one type of light-based 3D printing method known as digital light processing. (Figure 1.3.c and 1.3.d were reprinted from Biomaterials, *33*(26), Billiet, T.; Vandenhaute, M.; Schelfhout, J.; Van Vlierberghe, S.; Dubruel, P., A review of trends and limitations in hydrogel-rapid prototyping for tissue engineering, 6020-6041, Copyright (2012), with permission from Elsevier)[40] e, one type of light-based 3D printing method known as selective laser sintering. (Figure 1.3.a, 1.3.b and 1.3.e were adapted from Advanced Healthcare Materials, *4*(12), Do, A. V.; Khorsand, B.; Geary, S. M.; Salem, A. K., 3D printing of scaffolds for tissue regeneration applications, 1742-1762, Copyright (2015), with permission from John Wiley and Sons)[26]

Powder-binder printing is a type of ink-based 3D printing technique, where a liquid binder is used to connect two layers of powders.[26] As illustrated in Figure 1.3b, a liquid binder is dispensed through an ink-jet nozzle on the powder surface area of a fabrication reservoir monitored by the computer for one layer. Then, the fabrication platform lowers down, and roller processes a layer of fresh powders from the powder delivery reservoir into

the fabrication reservoir for the spread of the next binder layer. This process is repeated until the completion of the final 3D structure. This 3D printing method has been widely used in pharmaceutical research and applications to fabricate patient-specific drugs. In 2016, the U.S. FDA approved the use of powder-binder 3D printed Spritam® (levetiracetam) to treat epilepsy.[9] Compared to Spritam® tablets fabricated from conventional methods, these 3D printed tablets have the ability to achieve higher dose and faster dissolving properties for more patient-specific drug designs.

1.1.3.3 Light-based 3D printing

The combination of two layers in a light-based 3D printing technique is achieved with a light source (visible light, UV light, laser, or laser). The light source can induce chemical reactions of liquid resins or physical changes of metallic, ceramics or polymeric powders to join two layers.[8, 20]

As shown in Figure 1.3c, a photocurable liquid is usually placed in a deep vat in a stereolithography (SLA) 3D printing process. The surface of the liquid resin is first cured onto the fabrication platform *via* UV and/or visible lights which induce photo-crosslinking reactions. The platform subsequently lowers down at a designed distance according to CAD for the light cure of the next layer onto the previous layer. This process then repeats until the object is completed. A similar mechanism is behind the dynamic light projection (DLP) 3D printing technique. The main deviation is the light source delivery method where light is projected to the whole liquid layer with a pre-designed 2D pattern according to CAD *via* a digital mirror device (DMD). Thanks to the invention of DMD, which makes it faster to print an object, with less materials and less deep resin vat required as the DLP

printing pulls the object out of the liquid resin vat compared to traditional SLA process. Among most 3D printing methods, SLA and DLP are well-known for their high resolution control to provide a smoother finish of the final product.[36, 41]

DLP 3D printing has revolutionized how hearing aids were fabricated. It usually took over one week and nine steps to fabricate a hearing aid using traditional manufacturing methods which included earmold impression, molds casting, to final hearing aid shell trimming and electronic integration; without guarantees of the accuracy of the final product.[42] However, using a DLP technique shortened this process to one day. This could happen because 3D printing hearing aids only involve three steps. The scanning of the customer's ear, computer aided modeling and 3D printing of acrylate-based resins requiring less labor work. What's more, these hearing aids manufactured from 3D printing can also provide a better fit from customer to customer with the ability to fabricate numbers of hearing aids for multiple customers.[9, 42] The FDA has cleared the use of several materials for the fabrication of hearing aid devices and most manufactured hearing aids are 3D printed due to their better fit and comfort properties from high-resolution DLP 3D printing technique.[5, 9] Invisalign® is another example of how DLP 3D printing technique successfully transforms traditional clinical treatments.[9] Customized polymeric aligners can be 3D printed using DLP technique according to each patient's intra-oral anatomy. In some cases, these 3D printed removable aligners can provide patients with better appearance, faster treatment and more comfortability over conventional metal braces.

SLA and DLP 3D printings have also spurred along drug release design devices due to their high resolution and flexibility in device design.[9] Such high resolution control makes it possible to make drug delivery systems with various release profiles. Precisely

tuning the surface area to volume ratio of drug-loaded devices can be achieved, which is hard to achieve via traditional manufacturing processes.[37] Recent academic studies have shown the potential of using 3D printed microneedles in transdermal drug delivery applications. Using biodegradable photo-crosslinkable polymers, these 3D printed drug-loaded microneedles can maintain desired drug-release properties *in vitro*[43] and *in vivo*[44], plus causing less pain over traditional needles.[37, 44]

Instead of joining two layers via chemistry-induced photo-crosslinking reactions, selective laser sintering (SLS) 3D printing technique (Figure 1.3.e) uses a laser beam to fulfill the binding process. The scheme of SLS printer looks similar as that in powder-binder 3D printing technique (Figure 1.3.b) where powder materials are generally used. In 2013, U.S. FDA cleared the use of 3D printed polyetheretherketone (PEEK) material for cranial implant applications.[8] SLS processed medical grade titanium alloy devices also received U.S. FDA approval for use in surgical correction of hallux valgus deformities in 2015[45] and spinal implant applications in 2018.

1.2. Challenges in Using 3D Printing Technique for Implantable Medical Devices

Incorporating computer-aided design (CAD) and computer aided manufacturing (CAM), 3D printing techniques has shown it's potential to revolutionize the way to design and construct regenerative medical products where high customization is required for both esthetic and efficacy.[2, 29] Despite so many promising pre-clinical and some clinical results using 3D printed products for many medical applications illustrated above, adopting 3D printed products for regenerative medicine such as implantable devices for tissue regeneration, still lacks clinical applications due to many challenges. These challenges

mainly come from the regulatory aspect and limited good manufacturing practice (GMP) grade resorbable materials available for 3D printing to make regenerative tissues that fulfill the requirements for diverse tissue types.

1.2.1 Regulatory challenge

The U.S. FDA needs to evaluate the safety and effectiveness of a medical device before it reaches to public markets.[46] Although 3D printing can be beneficial to provide patient-specific implantable medical devices for tissue regeneration, few such medical devices have been cleared from FDA due to the regulatory complications.[5, 47] Such regulatory complications can come from the two following aspects.

On the one hand, there is a lack of regulation guidelines for 3D printed medical devices. 3D printed medical devices highlight their flexibility in fabrication of patient-specific devices, at various shape, function and size, where the FDA evaluates the final products.[5, 47] FDA regulations mostly compare the similarities rather than the differences. This diversity of 3D printed products increased regulatory complexity, which FDA has not faced before. After three decades since the invention of the 1st 3D printer in 2017, the FDA released the "Technical Considerations for Additive Manufactured Medical Devices" to help guide the regulations of current 3D printing industry for medicine.[48]

On the other hand, the path to make an implantable medical device can be costly.[46] Currently, the biomedical market is occupied with Class I medical devices (lowest risk medical devices like bandages), which require less efforts to be cleared by the FDA.[47] Most 3D printed wearable medical devices, like bone-conduction hearing aids and Invisalign fall in to the moderate risk medical device class (class II) category. The FDA commonly

requests a premarket notification (510k) submission before the release of Class II medical devices on market and human tests are generally not needed for this type of device.[46, 49] However, most implantable medical devices, like vascular stents, and implantable bone scaffolds are in the class III medical device category due to their highest risks to patients.[49] Before a class III medical device can reach the market, a premarket approval (PMA) is required by the FDA for a safety and effectiveness evaluation, typically requiring clinical tests with human participants.[46] Compared to 510k, PMA is a more costly process to make a medical device reach the market, which puts more hoops for such implantable medical devices to jump through. However, FDA has opened another pathway, humanitarian Use Device (HUD) program, to encourage research and applications of implantable medical devices to save patients' lives at severe conditions.[46] HUD is a special pathway designed for using high-risk medical devices without the requirement of efficacy data when patients are facing rare life-threating diseases or conditions.[46] One example of this case, was the famous 3D printed bioresorbable airway splint that saved a three-months-old infant's life in 2012 who suffered a severe tracheomalacia.[15]

1.2.2 Limited 3D printable resorbable materials for implantable medical device

FDA defined medical implants, as devices placed inside or on the surface of human bodies, which are used to replace the missing body parts, deliver medication, monitor organ functions or repair tissue and organ functions. The increasing orthopedic diseases and cardiovascular diseases require more implantable devices to treat such hard and soft tissue diseases.[50] This demand is expected to keep on growing with the prolonging life span and increasing elderly population as most of these diseases are age-related.[9, 50, 51] For example,

90% of populations with age over 40 showed joint diseases in late 20th century.[50] As orthopedic implants currently dominate the implantable device market[50], further discussions on this topic are displayed below.

Bone is the second most transplanted tissue to blood.[52] There were about 152 thousand total hip replacements procedures performed in 2000, and this number is estimated to double by 2030.[50] A small size bone tissue damage or fracture can heal itself, while larger size bone damages or fractures (critical-size) stemming from pathology, trauma or tumor resection require clinical intervention to guide the repair of damaged bone tissue. Globally, there are about two million bone graft procedures performed each year.[53] Based on the material source, bone grafts fall into three categories; autografts, allografts and synthetic bone grafts.[54, 55] An autograft is a bone material obtained from a patient's own bone source, such as distal tibia and iliac crest.[56] Current gold standard bone graft material is still an autograft due to the highest clinical success.[57,20, 41] However, using autograft can introduce 8.5-20% of complications such as extra blood loss, nerve injury, and extra pain at the donor site. Other challenges for a patient to use autograft include extra operation room cost coming from autograft harvesting surgery, limited amount, and difficulty in shaping autograft into irregular geometry to fit the wound site.[57] Allograft, a bone material donated from another person, has larger amount supply compared to autograft, but can bring risks like disease transmission and immune rejections.[58] These limitations of autograft and allograft materials emphasized the demand on other type bone graft materials to repair damaged bone tissue in a safe, cost-effective manner.[55, 58] This demand is expected to continuously growing with the increasing life expectancy of human

beings as bone fractures and diseases can happen more frequent among senior populations due to osteoporosis[53, 59].

Bone tissue engineering proposes to solve this shortage of bone graft materials problem by using engineered 3D scaffolds, together with cells and bioactive stimuli (e.g., bioactive molecule, mechanical factors) to temporarily maintain the normal functions at the wound site and gradually induce the patient's own bone tissue repair.[24, 54, 60, 61] This type of scaffold is expected to mimic the physiological characteristics of extracellular matrix for cells to live and eventually safely disappear (e.g., excreted, and/or resorbed) to provide a proper space for the regeneration of new bone.[62-64] A synthetic resorbable material is of great interests to be used as a scaffold material with the potential to be used in advanced scaffold making techniques, such as 3D printing.[8] Compared to traditional scaffolds fabrication methods, 3D printed porous resorbable scaffolds have better potential to be used for tissue regeneration.[3] These advantages include, better reproducibility in scaffold fabrication, the accurate control and flexible design external geometry and internal details such as pore properties.[26, 65] Pore architecture, size, interconnectivity and porosity are significant factors that influence the success of bone regeneration.[2, 9]

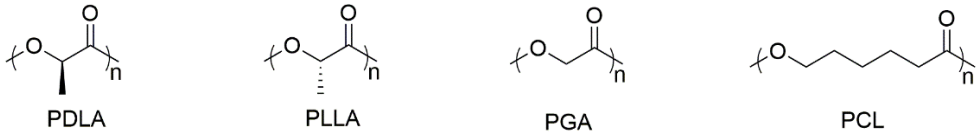

Figure 1.4. Chemical structures of some commercially available resorbable polymers. PDLA: poly(L-lactide acid); PLLA: poly(D-lactide acid); PGA: poly(glycolic acid); PCL: poly(ε-caprolactone).

Among these synthetic resorbable materials (ceramics, polymers, metals), polyesters are a class of degradable materials with wide applications in regenerative medicine due to their tunable chemical and physical properties.[60, 66, 67] These tunable

properties make them possible to be used for various tissues repair and regeneration, from soft tissues like cartilage, blood vessels and hard tissue like bone.[61, 63] Additionally, flexible processing abilities make them good candidates for different 3D printing techniques.[66, 68]

Several resorbable polymers have been clinically used for regenerative medical applications as they are non-toxic, can degrade in the human body at required rates and their degraded products can be safely cleared out from human body.[54, 68, 69]

Table 1.1. Physical properties of commercially available resorbable polyesters, examples of their applications in regenerative medicine and limitations of these materials to be used in 3D printing for patient-matched bone defect repair.[61, 66, 68, 71, 76, 77]

	PLLA	PCL	PDLLA	PGA
T_g (°C)	60-65	-65 to -60	50-60	35-45
T_m(°C)	170-200	58-64	Amorphous	225-230
Crystallinity (%)	37	30-50	0	30-55
Modulus[a] (GPa)	2.7-4.1	0.2-0.4	1.0-3.5	6.0-7.0
Degradation time[b] (months)	24-36	24-60	12-16	3-6
FDA cleared medical applications	Resorbable fixation pins, screws, tacks; Suture anchors	Resorbable suture; Drug delivery device	Suture anchors; Vascular stent;	Resorbable suture; fixation pins
Limitations to be used as 3D printed scaffolds for bone repair	Difficult to functionalize (e.g., too hydrophobic, causing poor cell adhesion and proliferation);			
	Degrade too slow, hinder patient's bone regeneration			Degrade too fast, causing inflammation of local tissues due to sudden accumulation of acidic products
	Too stable for bone surgery	Poor mechanical properties		

[a]Tensile or flexural modulus

[b]Complete degradation (rate may also be influenced on part shape, thermal history, and degradation medium)

These resobable polymers shown in Figure 1.4, poly(L-lactide acid) (PLLA), poly(D-lactide acid) (PDLA), poly(D, L-lactide acid) (PDLLA) (racemic mixture),

poly(glycolic acid) (PGA), poly(ε-caprolactone) (PCL), and their copolymers or blends have been heavily studied. Due to their non-toxic natural-existing degradation products[60, 62, 68], excellent mechanical properties[68, 70, 71] with the available GMP commercialization sources[72-74], some devices made from these polyesters have been developed and approved by the U.S. FDA for use in regenerative medicines in humans (Table 1.1).[66, 68, 75] Although these resobable polyesters have been clinically used in several degradable medical devices, they are not suitable for bone tissue regeneration due to some of their inherent physical and chemical properties (Table 1.1).

Generally a bone healing process can be completed in 4-12 months for most patients[20, 57, 78], which means the synthetic scaffolds are expected to degrade in sync with the new bone tissue growth. Using PLLA and PCL materials that have degradation times over two years for bone repair can hinder the successful bone regeneration or unwanted tissue responses due to the too slow degradation rate.[20, 79] Clinically implanted PLLA screws and plates for treatment of zygomatic bone fractures caused swelling issues for some patients after three years of implantation, requiring removal of the swelling.[80] This phenomena resulted from the remaining crystalline PLLA particles over three to six years.[80] On the contrary, PGA material is not beneficial for bone repair since it can lose strength within two months with complete degradation within six month, which cause insufficient mechanical support and protection of the local bone tissues and cause too short periods for cells to grow into the scaffold as a template.[81] Despite recent successful tuning of the mechanical, degradation properties of these polyesters by physical or chemical mixing from academic studies, the inherent hydrophobic property of these polymers make it challenging for cell adhesion and proliferation, let alone a successful bone tissue

regeneration.[63] Therefore, a new class of resorbable polymers with flexible functionalities, proper mechanical properties, ideal degradation frames and GMP synthesis routes is highly desired to be used in cost-effective and high-resolution 3D printing technique (e.g., DLP) for regenerative implants.

1.3. Poly(propylene fumarate) (PPF) and Its use in 3D Printing for Medical Applications

1.3.1. Compatible properties of PPF for use in regenerative medical applications

Since the birth of PPF in 1988[82], many reports have shown its excellent performance in biomedical applications such as hard tissue repair (e.g., bone substitutes)[82-84], soft tissue repair[83, 85-88], and controlled-release of biologically-active reagent (growth factors like peptides), cells and/or drugs.[20, 22, 41, 62, 82, 89-92] In general, PPF displays many characteristics which make it a suitable biomaterial for regenerative medical applications, namely 1) non-toxic degradation products, 2) compatible mechanical properties, 3) tunable degradation profiles, 4) facile loading of bioactive materials, and 5) flexible design in 3D-printed constructs.

1.3.1.1 Non-toxic degradation products

As shown in Scheme 1.1, PPF itself is an unsaturated polyester, whose degradation products are fumaric acid and propylene glycol, both of which are non-toxic and are easily cleared from the human body. Fumaric acid, a natural existing intermediate substance found in Krebs cycle,[20, 82, 90] is considered non-toxic and tolerated *in vivo*[20]. Propylene

glycol, a commonly used food additive and drug diluent,[89, 90] can be metabolized or excreted from the human body.[41, 67, 90, 93] These non-toxic and resorbable degradation products make PPF an ideal target for *in vivo* applications.[94]

1.3.1.2. Compatible mechanical properties

The unsaturated double bonds on PPF back bone can undergo radical induced crosslinking reaction with triggers like light and/or heat.[82, 89, 95] This crosslinking reaction can happen with PPF itself and/or with various other compatible monomers and/or polymers containing unsaturations.[41, 93] The ability of PPF to crosslink with both itself and reactive diluents (e.g., diethyl fumarate) allows for the tailoring of mechanical properties and degradation patterns of PPF based products for various applications.[35, 36, 41, 62, 82] For example, these mechanical properties can be tuned to the range for trabecular bone repair applications by varying the crosslinking density of PPF based resins[82, 84, 89, 96] This is important in bone tissue engineering applications as the mechanical properties of the bone or tissue substitute is expected to have similar mechanical property of the bone or tissue replaced to fulfill its function like skeleton protection. For instance, a minimal compressive modulus around 50 MPa for trabecular bone applications.[97-99]

1.3.1.3. Tunable degradation profile to promote new tissue in growth

The degradation rate of PPF-based material can also be tailored to meet the requirement of many medical device applications like controllable drug delivery[43, 82, 89, 90], or to meet the new-bone regrowth speed *in vivo*[20]. The scaffold degradation rate is a key to

the successful repair of bone tissue defects in tissue engineering.[100] Quick degradation rates may cause insufficient cell attachment and proliferation at the wound site, while a slow degradation rate may limit or hinder the rate of new bone remodeling, both of which can cause improper bone defect healing.[36, 79, 89, 101, 102]

1.3.1.4. Ability to carry bioactive molecules and drugs

Unlike conventional resorbable biomaterials PLA, PGA, and PCL, which lack reactive functional handles, PPF polyesters contain functional sites in their unsaturations. Various peptides have been successfully incorporated into PPF material to promote cell adhesion, proliferation, and differentiation *in vitro* and *in vivo*.[103-109] For example, as an inherent hydrophobic polymer[104], PPF-based material has limited ability to attract cell adhesion when used as a bone tissue engineering scaffold. Several studies have demonstrated that cell-adhesion promoting peptide RGD can be physically or chemically functionalized with PPF-based scaffolds, and results showed a significant improvement for cell adhesion[95, 104, 106].

At the same time, PPF-based materials can also be used as drug carriers to deliver drugs in sustained release profiles for injectable, transdermal, and implantable drug delivery.[22, 43, 89, 91, 110, 111] The various drug release profiles can be tailed by tuning the molecular mass of PPF used in the carrier formulation,[112] the crosslink density of PPF[110], and the concentration of the loaded drug in PPF matrix.[110]

1.3.1.5. Flexibility in 3D design for patient-specific medical applications

The unsaturated double bonds on PPF backbone also make it possible to be used in light-based 3D printing technique (e.g., SLA, DLP, and FDM with post-extrusion light curing system).[20, 113, 114] This advanced fabrication method has increased interest in using PPF for patient-specific cases such as bone tissue repair (e.g., cranial facial repair)[20, 115-120] and drug delivery system.[22, 43, 121] The ability of patient-specific treatment using 3D-printed PPF scaffolds makes it possible to provide more accurate scaffold according to the digital data obtained from the scanning of the wound site, and can reduce the overall operation room cost over an autograft treatment method.[41, 122, 123] DLP and FDM 3D printed PPF-based scaffolds have shown great mechanical and degradation properties that are suitable for bone regeneration applications.[36, 113, 114]

1.3.2. Introduction to synthetic methods of PPF

Various methods have been proposed and used to prepare PPF during the past several decades, and each has resulted in PPF with various polymeric properties.[20, 61, 90, 93, 124-126] From polymer chemistry point of view, these methods can be categorized into two types: i) step-growth polymerization and ii) ring opening copolymerization (ROCOP). Each of these synthetic approaches has a set of inherent advantages and disadvantages (will be discussed in the following part of this section), and so care must be taken when using PPF materials for desired properties or applications.

1.3.2.1. Step-growth polymerization to synthesize PPF

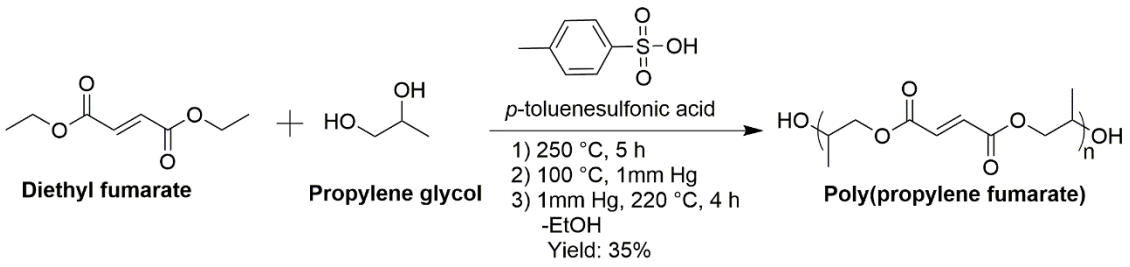

Scheme 1.1. Poly(propylene fumarate) transesterification synthesis method by Sanderson in 1988

One of the earliest PPF synthesis methods was patented by Sanderson in 1988[62] to be used in a bone replacement resin, which can be cured at physiological temperatures.

As shown in Scheme 1.1, in this transesterification method, diethyl fumarate (DEF) and propylene glycol were used as monomers at an equal molar ratio to synthesize PPF using *p*-toluene sulfonic acid as a catalyst. However, this reaction requires elevated temperatures (250 °C) and the removal of volatiles under 1mm Hg vacuum to obtain PPF in about 35% yield.[20, 62] After about 9 h of reaction, the final PPF was reported 90% molecular weight in the range of 1300 Da to 124000 Da. Sanderson later revised the reaction conditions by adding t-butyl hydroquinone as an antioxidant and a suspension of silicone oil to reduce saturation of double bonds and improve molecular mass. This revised reaction can be performed at a lower temperature range of 165-180 °C, but requires 158 h to complete on a 0.4 moles monomer input size; Once increasing the total monomer input value into 1.6 moles (197.64 g), this reaction took over 400 h to complete regarding the removal of larger amount of alcohol byproduct during the PPF chain propagation process and the removal of unreacted monomers at the end of the reaction. The number-average molecular mass ($\overline{M_n}$) of PPF was reported 17000 Da-20000 Da from these revised reactions.

Gerhart and Hayes developed another condensation method to get PPF for bone repair applications in 1989.[89] In their method, fumaric acid and propylene glycol were used as monomers, which was first heated at 145 ºC to remove water byproduct and then to 180 ºC to remove propylene glycol monomers to get PPF.[20] PPF synthesized from this method typically results in $\overline{M_n}$ between 500 Da and 1200 Da with molecular mass distributions between 3 and 4.[61, 62] Compared to Sanderson's method,[62, 82] the purification of PPF is relatively simple and less labor-intensive, since no catalyst or crosslinking reagent were used.[89]

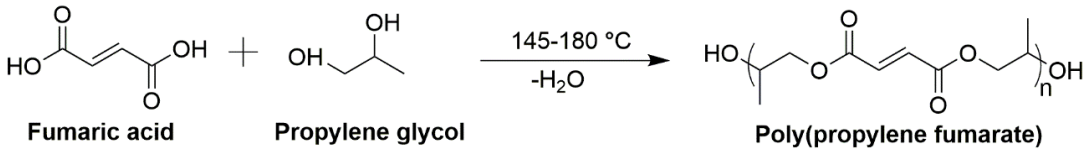

Scheme 1.2. Poly(propylene fumarate) condensation synthesis method by Gerhart and Hayes in 1989

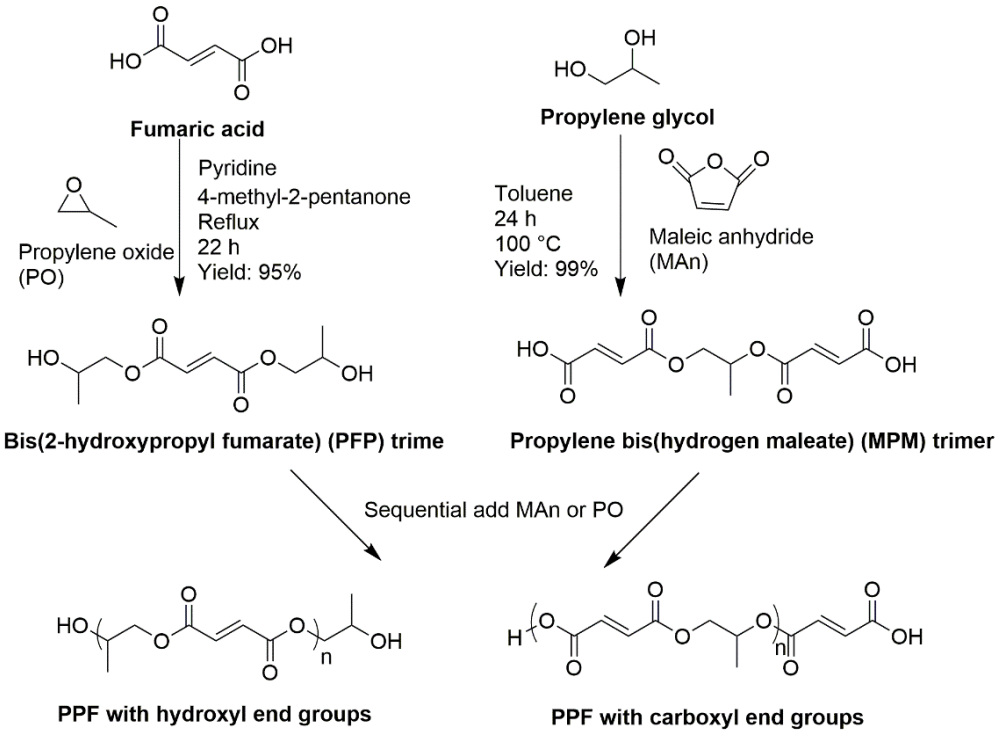

Scheme 1.3. Poly(propylene fumarate) condensation synthesis method by Domb in 1990

Domb also developed several methods to obtain PPF polyesters in 1990 for bone substitute applications.[62, 127] One of the most classic route was shown in Scheme 1.3, with the narrowing of the molecular mass distribution and a better control over chain-end of PPF oligomers (3-15 monomers). This synthetic method started from the preparation of two trimers, the bis-(hydroxypropyl) fumarate trimer and the propylene bis(hydrogen maleate) trimer, by reacting propylene oxide (PO) with fumaric acid or maleic anhydride (MAn) with propylene glycol, respectively.[20, 61] Each trimer reaction took about one day to complete. The purified two trimers were then reacted with MAn and PO monomers in sequence to produce PPF materials with either hydroxyl chain ends or carboxyl chain ends (Scheme 1.3). PPF synthesized from Domb's method usually had a number-average molecular mass in the range of 158 Da to 1320 Da with a molecular mass distribution ($Đ_m$) between 1.02 and 1.52,[20, 61, 127] which was the narrowest molecular mass distribution for PPF synthesized at the time. However, since this method required sequential additions of MAn or PO monomers into pre-oligomers with two hydroxyl chain ends or pre-oligomer with two carboxy chain ends, the reaction and purification became time-consuming, especially for higher molecular weight targets. (e.g., 6 days reaction time for $\overline{M_n}$ 2.0 kDa PPF plus purifications after each step).

In 1994, Yaszemski, et al. synthesized PPF through a transesterification reaction of bis(hydroxypropyl fumarate), obtained from an initial reaction of propylene glycol and diethyl fumarate. This transesterification reaction was usually performed at 145-220 ºC with antimony trioxide as a catalyst for five hours.[20, 61, 84, 126] The number-average molecular mass of PPF synthesized from Yaszemski's method were in the range of 500 Da to 2040 Da, and displayed very broad molecular mass distributions (e.g., the highest reported molecular mass for $\overline{M_n}$ = 2038 Da, $Đ_m$=5.85).[3,4]

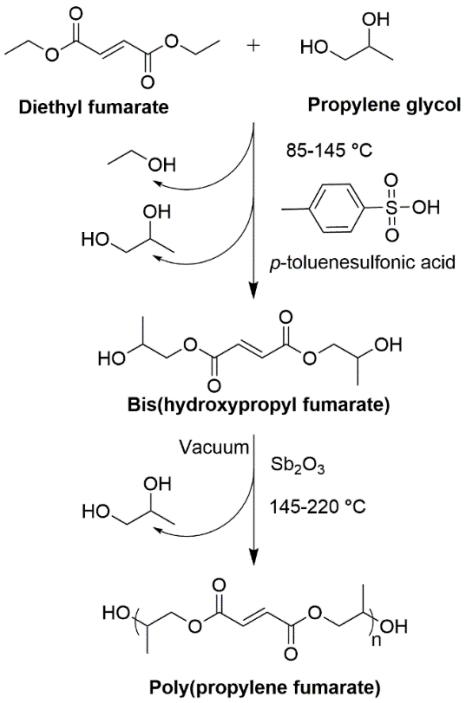

Scheme 1.4. Poly(propylene fumarate) condensation synthesis method by Yaszemski in 1994

In 1997, Kharas et al[128] widely studied catalysts' influence on condensation synthesis of PPF with relatively high molecular mass from diethyl fumarate and 1,2-propanediol monomers at high temperatures.

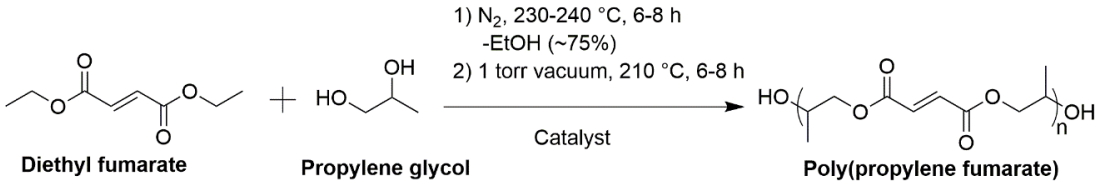

Scheme 1.5. Poly(propylene fumarate) condensation synthesis method by Kharas in 1997

As shown in Scheme 1.5, this ester exchange reaction happened at over 200 °C with two general stages. The first step included the formation of bis(hydroxypropyl) fumarate diester from diethyl fumarate and propylene glycol with the elimination of ethanol from the reaction system. The second step was polycondensation of bis(hydroxypropyl) fumarate at a

higher temperature to influence (like to drive the ester-exchange reaction to the completion direction and keep polymer in melt state during reactions) polymerization to get relatively higher molecular mass PPF.

Table 1.2. Polycondensation conditions and PPF properties from Kharas's method in 1997

Catalyst	**Time (h)**	**Max temp. (°C)**	**Saturated double bond[b] (%)**	**Yield (%)**	$\overline{M_w}^{SEC}$ **(kDa)**	$Đ_m^{SEC}$	T_g[c] **(°C)**
PTSA[a]	16	240	25-30	38	32.6	2.2	23
$AlCl_3$	16	230	3-5	42	13.7	2.3	14
$TiCl_4$	12	200	3-5	43	20.9	1.4	14
$Ti(OC_4H_9)_3$	12	200	3-5	65	15.2	1.4	16
$ZnCl_2$	12	200	3-5	68	26.6	1.9	16

[a]PTSA: *p*-toluenesulfonic acid; [b]Unsaturated fumaric double bonds became saturated via the addition reaction from hydroxyl end group from propylene glycol at high temperatures [c]Glass transition temperature determined by DSC 2920 with a heating rate of 5 °C/min in the temperature range of -30 °C to 120 °C

As shown in Table 1.2, various catalysts were used in this reaction to test their influence on the reaction, as well as the chemical and physical properties of PPF obtained. Although, PTSA, the strongest acid catalyst used in this study, showed the ability to generate PPF with the highest molecular mass and glass transient temperature, the degree of unsaturation decreased by 25-30%.[128] This was caused by the addition reaction by the hydroxyl groups from propylene glycol monomers, which generated several unexpected side products like uncontrolled branches of PPF.[129] When switching catalyst from the strong acidic PTSA to relatively less acidic $ZnCl_2$, $TiCl_4$ and a weak basic catalyst $Ti(OC_4O_9)_4$, the DEF monomer was found to favor ester formation with primary hydroxyl group on propylene glycol monomer, while only 3-5% of the fumaric double bonds were reported saturated from ^{1}H NMR spectra.

Based on these results from Kharas et al., Shung et al.[130] performed detailed kinetic studies in this step-growth polymerization of PPF to see the influence of temperature (130 °C, 150 °C, 200 °C) on the polymerization of DEF and propylene glycol with zinc chloride catalyst in 2001.

In addition to the method from Kharas, Shung et al. used hydroquinone in the reaction system to prevent possible crosslinking side reactions. They found as the polymerization temperature increased, the molecular mass of PPF increased. Reactions at 200 °C were found gelated at around 4 hours of polymerization, which demonstrated that a crosslinking side reaction dominated at the higher reaction temperature, with the highest detectable number-average molecular mass of PPF 3.3 kDa and a molecular mass distribution around 2.95. The overall highest $\overline{M_n}$ was found 4.6 kDa with a molecular mass distribution around 2.28 at 150 °C reaction temperature. The molecular mass distribution of PPF synthesized from these methods were found in the range of 1.6-3.0 before precipitation into ether.

In 2009, Kasper et al. modified the PPF synthesis reaction conditions from Shung et al. and under more mild reaction conditions [20, 93] In their method, propylene glycol and diethyl fumarate monomers were first reacted at a molar ratio of 3:1, with $ZnCl_2$ as the catalyst and hydroquinone as a crosslinking inhibitor, while gradually increasing reaction temperature from 110 °C to 130 °C to obtain bis(hydroxypropyl) fumarate diester. This diester intermediate was then used in the second step, a transesterification reaction to convert bis(hydroxypropyl) fumarate into PPF, with an increasing reaction temperature from 100 °C to 130 °C under a reduced pressure to remove propylene glycol volatile byproduct. They also showed the whole process should be able to be completed in 3 days with the number-average molecular mass of PPF in the range of 0.5-4.0 kDa.

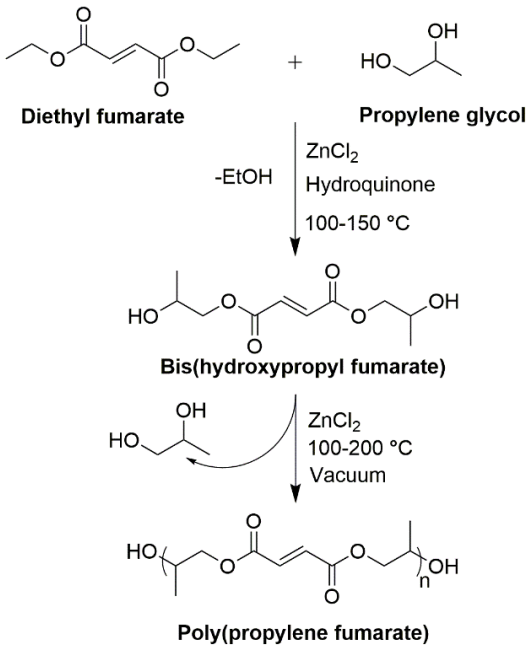

Scheme 1.6. Poly(propylene fumarate) condensation synthesis method by Shung in 2001

1.3.2.2. Ring-opening copolymerization (ROCOP) to synthesize PPF

Well-controlled synthesis of PPF using ring-opening copolymerization methods was recently reported in works from DiCiccio and Coates in 2011.[90] In their method, cyclic monomers, MAn and PO were reacted at 45 °C for 15 hours with a chromium(III) salen complex as a ring-opening catalyst to yield poly(propylene maleate) (PPM) intermediate polyester. Since the *cis*-alkene double bonds on PPM were not active enough for further radical crosslinking reactions to enhance the mechanical properties of this polyester for most bone-tissue engineering applications[20, 90], the intermediate PPM was generally isomerized with a basic amine catalyst to obtain PPF. As the number-average molecular mass and the molecular mass distribution maintain consistent in throughout the isomerization step[90], one can control the number-average molecular mass of PPF basically in the ring-opening copolymerization

step, that is the PPM synthesis step. PPM synthesis methods from literatures (2000-2013) were summarized in the following part.

1.3.2.2.1. Ring-opening copolymerization (ROCOP) to synthesize PPM

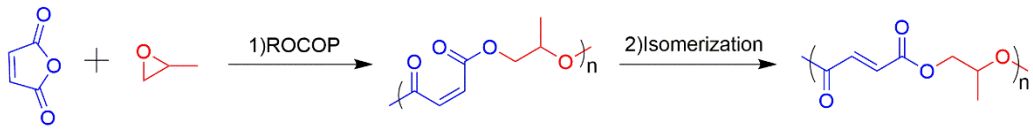

Scheme 1.7. General preparation of poly(propylene maleate) oligomers by ring-opening copolymerization of maleic anhydride and propylene oxide and a subsequent isomerization into poly(propylene fumarate).

Due to the extensive breadth of the available ring-opening copolymerization synthetic methods for polyester synthesis from cyclic anhydrides and epoxides monomers, the following section provides a brief summary of ROCOP methods used from previous researches to obtain PPM. The monomers used in this ring-opening copolymerization are MAn and PO as shown in Scheme 1.7.

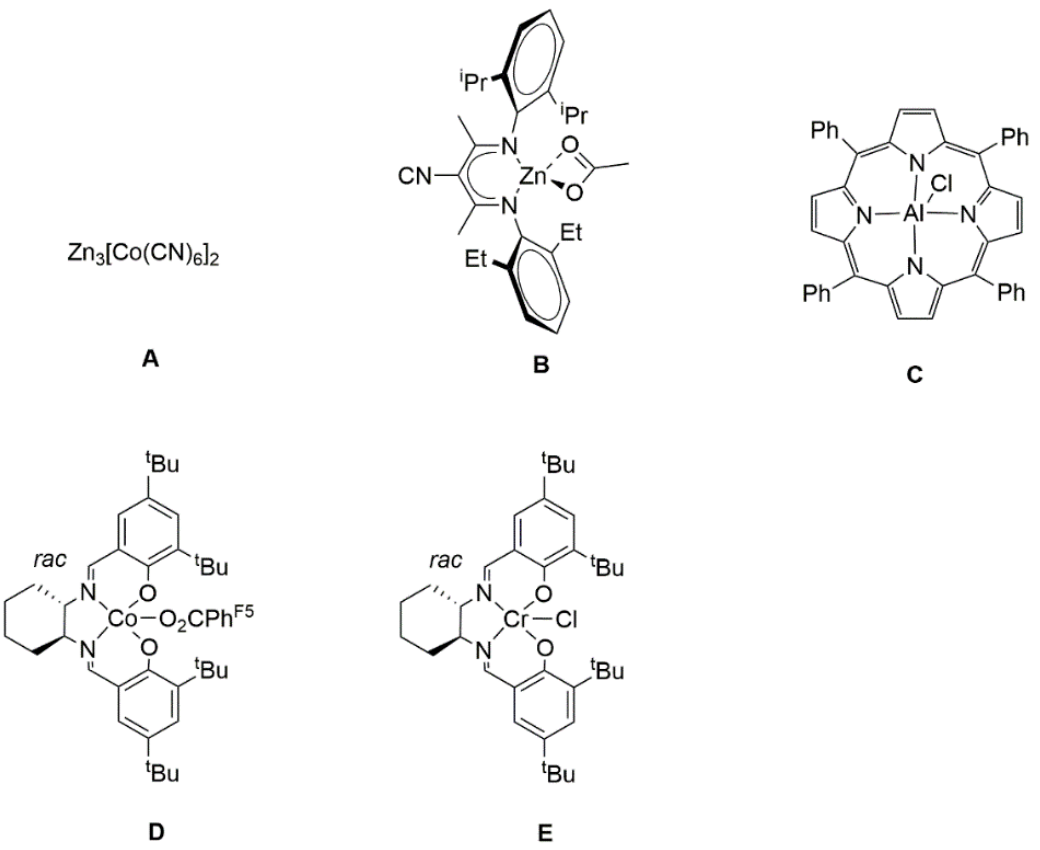

Figure 1.5. Catalysts used in ring opening copolymerization of MAn with PO from literature before 2013

To get PPM with target molecular properties for designed applications, various efforts have been put into studying the polymerization factors that influence the molecular mass. Such factors include types of solvent, catalyst, initiator, polymerization temperatures, polymerization durations, and so on.[41, 90, 125, 131-133] Several catalysts used in ROCOP to synthesize PPM before 2013 were listed in Figure 1.5.

As shown in Table 1.2, molecular mass properties of PPM synthesized from ring opening copolymerization can get significantly influenced and controlled by the polymerization parameters, such as polymerization temperature, monomer concentrations, polymerization time, types of catalyst, and initiator to monomer ratios.

Table 1.3. Ring opening copolymerization conditions in synthesis of PPM from MAn and PO

#	Catalyst [Cat]	[MAn]:[PO]:[Cat]	Solvent	[MAn] (M)	Temp (°C)	Time (h)	Conv[a] (%)	Ether[a] (%)	$\overline{M_n}$[b] (kDa)	$Đm$[b]
1	$Mg(OEt)_2$	122:122:1	Toluene	7.14	80	48	NA	5	4.2	1.17
2	A	25000:25000:1	THF	2.5	70	16	54.3	NA	2.2	1.72
3					80	16	73.5		2.7	1.66
4					90	16	95.1		3.4	1.38
5					100	14	98.2		3.0	1.42
6					115	14	99.6		2.7	1.69
7		37500:37500:1			90	16	59.2		2.7	1.76
8		20000:20000:1				16	98.2		2.9	1.68
9		10000:10000:1				14	99.6		1.3	1.96
10		5000:5000:1				14	99.6		0.8	2.23
11		25000:25000:1				8	21.5		2.2	1.72
12						12	67.3		2.7	1.35
13						20	98.7		3.4	1.34
14			THF	2.5		16	96.7	5	3.2	1.37
15			Acetone				92.8	NA	2.9	1.48
16			Cyclohexane				84.3		3.3	1.65
17			Diethyl ether				81.2		2.9	1.50
18			DCM				66.4		2.7	1.71
19	B	200:200:1	Toluene	8	45	15	5	86	5.0	1.20
20	C						7	50	14.0	1.10
21	D						12	<1	5.0	1.10
22	E						47	<1	6.0	1.30
23	E		Hexanes				>99	<1	17.0	1.60

[a]From NMR [b]From SEC

To the author's best knowledge, the first ring opening copolymerization of MAn and PO found in literature was the one performed by Takenouchi in 2002[125] (Table 1.3, No. 1). In this method, magnesium ethoxide was used as an initiator, which may also function as a catalyst to activate the monomers. This method demonstrated that the ring opening

copolymerization method can generate PPM with a well-defined molecular mass distribution at 1.17 at a number-average molecular mass of 4.2 kDa with a yield around 42%.

In 2004, Hua et al[131], showed various methods (Table 1.3, No. 2-18) to control the molecular mass, molecular mass distribution, and conversion in ring opening copolymerization of PPM using $Zn_3[Co(CN)_6]_2$ double-metal cyanide (DMC) based catalyst. Compared to reactions performed in bulk, they first noticed this ROCOP reaction can be completed faster with the use of a solvent.[131] They then investigated the influence of polarity of solvents (Table 1.3, No. 14-18) on the reaction and the product properties; higher conversions were seen with polar solvents (THF, acetone) compared to solvents of lower polarity (cyclohexane, diethyl ether). However, they did not explain why the relatively high-polarity solvent dichloromethane showed the lowest conversion among these solvents. Next, choosing THF as a model solvent, they studied influences of catalyst loading level, polymerization temperature, and reaction time on the molecular mass of PPM. The effects of catalyst loading levels are shown in Table 1.3 (No. 7-10). The highest number-average molecular mass was found to be 3.4 kDa with a conversion over 95% and a molecular mass distribution 1.38 at a moderate monomer to catalyst loading level (25000:1). The highest conversion was found over 99% when increasing the catalyst to monomer molar ratio from 1:25000 to 1:10000 (No. 9,10). However, increasing the catalyst loading ratio (from 1:25000 to 1:5000) showed a drop in $\overline{M_n}$ (3.4 kDa to 0.8 kDa) and a broadening in the molecular mass distributions (1.38 to 2.23) of PPM. The effects of polymerization temperatures are shown in Table 1.3.2.2.1, No. 2-6. The reaction conversion was found to increase when elevating reaction temperature from 70 °C (54.3%) to 115 °C (99.6%). A similar trend was found in the $\overline{M_n}$, however a broadening of the molecular mass distribution appeared at 115 °C. This increase in molecular mass distribution indicates that

depolymerization of the active polymer chains was preferred over the propagation reaction at a certain high temperature for this ROCOP reaction.[131, 134] The monomer conversion of this ROCOP reaction increased from 21.5% to 98.7% in an almost linearly trend during a reaction time of 8 h to 20 h (No.11-14), which denoted predictable $\overline{M_n}$ properties in general ROCOP reactions.[134]

In 2011, as shown in Table 1.3. (No. 19-23), Diccicio et al. reported that by using the chromium (III) salen complex in ROCOP synthesis of PPM, high $\overline{M_n}$ (17 kDa) and high conversion (>99%) can be achieved with well-controlled molecular mass distribution (1.6). In addition, they noticed that the choice of catalyst had an important effect on the percentage of ether linkage formed with PPM ester, denoting another parameter to that may influence properties of PPM.

1.3.2.2.2. Isomerization reaction to convert PPM to PPF

Several methods were previously reported to convert PPM into PPF in solution isomerization reactions.[90, 125, 135] Generally, PPM isomerization was performed in a variety of solvents using an amine-based catalyst. Propylamine, dipropylamine, morpholine, piperidine, and diethylamine were reported as effective catalysts to achieve >99% conversion. Among these catalysts, diethylamine was recently reported as the most efficient by DiCiccio and Coates in 2011.[90] This reaction was also found to complete faster at a higher reaction temperature.[135]

1.3.3. Summary of current challenges in PPF synthesis for medical applications

To sum up, from 1988 to 2009, various routes were used and developed in step-growth polymerization of diesters or diacids with diols to obtain PPF polyesters for biomedical applications.[62, 82, 84, 89, 132, 136] However, this synthetic approach generally needs long reaction time, removal of small molecule byproducts, such as alcohol or water to drive the condensation reaction. Polymerization at such high temperature also brought unwanted side products[129] like prematurely crosslinked polymers, which may hinder the application of PPF in medical applications which require with well-controlled properties.[41, 90] Although the unwanted crosslinking issues had been improved by adding crosslinking inhibitors into these step-growth reaction systems, further purification efforts and time were required to remove these inhibitors for biological applications.[93] Another main disadvantage of PPF synthesized from step-growth method was the relatively broad molecular mass distribution ($Đ_m$>2), which made it hard to control the physical properties (like viscosity, glass transition temperature, and mechanical properties) of PPF.[20] Although multiple fractional precipitation methods were previously used in academic researches to drop down the molecular mass distribution of PPF[62, 130, 137], it is still a challenge to reproducibly control this property for larger scale synthesis, let alone for commercialization. These drawbacks in step-growth PPF synthetic approach probably have hindered the industrial scale-up synthesis process of PPF and limited further researches of using PPF-based biomaterials in larger animal studies.[20, 41]

From 2000 to 2011, several ROCOP systems were developed to improve the PPF synthesis conditions and the corresponding polymer properties (purity, conversion, $\overline{M_n}$,

$Đ_m$).[90, 95, 125, 131] Compared to the traditional step-growth polymerization method[82, 93, 137], these ROCOP reactions were performed at reduced temperatures (<100 °C), provided higher atom economy, and resulted in a narrower $Đ_m$, a better control of number-average molecular mass, and less undesired crosslinked double bonds in the final PPF product.[20, 41, 95] Although, DiCiccio et al. demonstrated huge improvement in the control of molecular properties and the conversion of PPF polyesters using ROCOP methods, the Cr and Co metal catalysts used in their systems are relatively toxic for biomedical applications.[20, 41] The PPF synthesized from their methods were solid-like at room temperature with viscosities too high to be used in DLP type 3D printing.[41] The rest of these reported ROCOP methods used in researches using a relative less toxic catalyst (i.e., Mg- or Al-based) had their limitations such as large ether linkage and low conversions, and most of these ROCOP methods were performed in small scales (under 200 mL). Thus, it is still a challenge to reproducibly synthesize large scale PPF polyesters with properties suitable for medical applications. A scaleable method to reproducibly produce well-defined PPF for 3D printing is on-demand to push the researches on PPF-based products forward into larger animal studies. Solving this challenge may help pave the road of using PPF-based resorbable materials for medical applications bench-to-bed.

CHAPTER II

MATERIALS AND INSTRUMENTS

2.1 Material

All reagents were purchased from Sigma-Aldrich (St. Louis, MO, USA) and used as received unless otherwise specified. All organic solvents were purchased from Sigma-Aldrich (St. Louis, MO, USA) or Fisher Scientific (Hampton, NH, USA) as ACS Grade and used as received without any further purification unless otherwise specified. Irgacure 784 was purchased from Gelest (Morrisville, PA, USA). Propargyl alcohol was dried over calcium hydride for 24 h before vacuum distillation. *Meso*-erythritol was dried by azeotropic distillation before use.

Maleic anhydride (MAn): Sigma-Aldrich, 99%.

Propylene oxide (PO): Sigma-Aldrich, 99.5%.

Magnesium ethoxide: Sigma-Aldrich, 98%.

Toluene: Sigma-Aldrich, anhydrous, 99.8%.

Tetrahydrofuran (THF): Sigma-Aldrich, GR ACS.

Chloroform: Sigma-Aldrich, GR ACS.

Diethyl ether: Sigma-Aldrich, ≥ 99.7 %.

Hexanes: Sigma-Aldrich, 98.5%.

Sodium phosphate dibasic: BioXtra, ≥99.0%.

Sodium phosphate monobasic: BioXtra, ≥99.0%.

Sodium chloride: Sigma-Aldrich, GR ACS.

Calcium hydride: Sigma-Aldrich, 95%.

Diethylamine: Sigma-Aldrich, 99%.

Meso-erythritol: Sigma-Aldrich, ≥99.0%.

Propargyl alcohol: Sigma-Aldrich, 99%.

Diethyl fumarate: Sigma-Aldrich, ≥ 98.0%.

Phenylbis(2,4,6-trimethylbenzoyl)phosphine oxide (BAPO): Sigma-Aldrich, 97%.

Oxybenzone: Sigma-Aldrich, 98%.

2.2 Instruments

2.2.1 Nuclear magnetic resonance (NMR)

^{1}H NMR and ^{13}C NMR spectra were obtained using Varian NMR 300 MHz and 500 MHz Spectrophotometers. All chemical shifts were reported in ppm (δ) with solvent resonances (^{1}H NMR Chloroform-*d* 7.26 ppm; ^{13}C NMR Chloroform-*d* 77.2 ppm; ^{1}H NMR DMSO-d_6 1.50 ppm). Relaxation time of ^{1}H NMR was 2 sec and scan numbers were 64. Relaxation time of ^{13}C NMR was 2 sec and scan numbers were 1000. Abbreviations of s, d and m were used to represent singlet, doublet and multiple, respectively.

2.2.2 Attenuated total reflectance fourier transform infrared (ATR-FTIR)

ATRFTIR spectroscopy was performed using a Shimadzu (Kyoto, Japan) MIRacle 10 ATR-FTIR with a spectral range from 400 to 4000 cm^{-1}. Repetitive scans (32) were collected and averaged.

2.2.3 Size Exclusion Chromatography (SEC)

The relative number-average molar masses ($\overline{M_n}$) and the molar mass distributions ($Đ_m$) were determined by size exclusion chromatography (SEC) on a Tosoh Bioscience GmbH (Griesheim, Germany) EcoSEC HLC-8320GPC with TSKgel GMHHR-M columns in series at 45 °C. The sample concentrations were 10 $mg \cdot mL^{-1}$. Tetrahydrofuran (THF) was used as eluent flowing at 1.0 $mL \cdot min^{-1}$. The detector used in this determination was a refractive index detector (RI) and a series of polystyrene (PS) standards of narrow molecular mass distributions (with of $\overline{M_w}$ ($g.mol^{-1}$): 500; 578; 1010; 2420; 5970; 10200; 18100; 37900; 96400; 190000; 427000; 706000; 1090000; 2110000; 5480000) were used to determine the relative molecular mass.

2.2.4 UV-visible spectroscopy (UV-Vis)

UV-Vis spectra were collected using a Hewlett Packard 8453 UV-Vis Instrument at a wavelength ranging from 190 nm to 700 nm with a resolution of 2 nm.

2.2.5 Mass spectroscopy

The chemical structures of PPF samples were further analyzed by a Bruker (Billerica, MA, USA) Ultraflex III Matrix-Assisted Laser Desorption/Ionization Time-of-Flight (MALDI-ToF/ToF) mass spectrometer. The samples were dissolved in $CHCl_3$ or THF at a final concentration of 10 mg/mL. The sandwich method[138] was used with trans-2-[3-(4-tert-Butylphenyl)-2-methyl-2-propenylidene] malononitrile (DCTB) as matrix and NaTFA as salt 10:1. End groups were identified for absolute molecular mass characterization.

2.2.6 Thermal analysis

Differential scanning calorimetry (DSC) was performed using a DSC-TA Discovery DSC250 (New Castle, DE, USA) scanning a temperature range from -40 to 80 °C with heating and cooling ramps of 10 °C·min^{-1}, under nitrogen atmosphere with a flow rate of 40 mL·min^{-1}. The glass transition temperature (T_g) was determined from the midpoint of the transition in the second heating cycle.

2.2.7 Viscosity tests

The intrinsic viscosity of linear PPF samples at five molecular mass levels was measured in THF using an Ubbelohde viscometer at 35 ºC. Each PPF sample ($\overline{M_n}$: 0.7 kDa, 1.27 kDa, 1.86 kDa, 2.45 kDa, and 3.16 kDa) was weighed and diluted in THF in a volumetric flask (10 mL). Freshly distilled THF was added into the volumetric flask to the

10 mL mark with a 0.45 um filter and sealed. The capillary viscometer was cleaned with pure THF. A thermostat water bath was heated to maintain the temperature at 35 ^{o}C. The capillary viscometer was pre-equilibrated in the thermostat bath for at least 15 minutes to establish the thermal equilibrium. An injector was used to make the liquid fill up to more than one third of the top ball of the capillary viscometer and then allowed the liquid to flow down. A stopwatch was used to record the time when the liquid passed over the first line on the capillary viscometer and stopped recording when the liquid passed the second line on the capillary viscometer. The time of this period was recorded. The flow time was recorded at least five times. The capillary viscometer was refilled by a filter with 5.0 mL of the solution prepared of PPF and THF. The capillary viscometer was put back into the thermostat bath. The flow time was measured and recorded for at least three times as described above. Then 5.0 mL, 3.0 mL and further 1.8 mL or 2.0 mL (results dependent) of pure THF solvent was added into the capillary viscometer using a filter respectively, and the corresponding flow time was measured and recorded for at least three times each. The calculations and experimental details are noted in the supplemental information.

Complex viscosity properties of PPF:DEF solutions were measured using an AR-G2 rheometer TA Instruments (New Castle, DE, USA) at frequencies ranging from 0.1 Hz to 100 Hz (0.6 to 628.3 rad.s^{-1}) at 10 °C temperature intervals of 25 °C, 35 °C, 45 °C and 55 °C. Oscillatory shear measurements were conducted using a 40 mm 2° diameter steel cone with a truncation gap of 55 μm to measure the complex viscosity (η^*) and deduce the zero-shear viscosity (η_0) at 5 % strain.

2.2.8 3D printing

Tensile bars were printed from liquid resins using an EnvisionTEC Micro HR 279 printer and a computer-aided design (CAD) file of American Society of Testing Materials (ASTM) D638 type V model at a scale of 50 %. The exposure time was 120 s for each layer with a designed layer thickness of 50 μm. Each print was finished in about 4 h at 22-24 °C, after which the tensile bars were gently rinsed with acetone three times and dried with compressed air. The green tensile bars were then placed between two microscope slides for 20 min to post-cure in a full spectrum UV irradiation chamber (at ambient temperature (20 ± 2 °C). At least five tensile bars were 3D printed from each resin formulation for further characterization.

Gyroid scaffolds were printed from liquid resins with an EnvisionTEC (Dearborn, MI, USA) Micro HR 279 printer using a 405 nm LED UV light projector with an irradiance of 225 $mW \cdot dm^{-2}$ and the computer-aided design (CAD) models were digitally sliced into layers using the Perfactory software suite prior to manufacturing. The Perfactory P3 is an inverted system that projects upward through a transparent glass plate into a reservoir containing the resin. After each projection, the build platform moves vertically upward to allow resin inflow for the next layer. Prior to scaffold printing, cure tests of PPF-based resins were performed to determine the optimal printed layer thickness and UV exposure time depending on the resin formulation. 20 mg of resin was placed in the middle of the resin tray and after irradiation with UV for varying time durations (*i.e.*, 60, 120, 180 and 240 s), the uncured liquid resin was gently removed by tissue paper. The resulting film was peeled off the resin tray with a razor blade and the thickness of the cured film was measured

by a digital caliper (Marathon, Vaughan, Ontario, Canada) with 10 μm precision. Following these cure tests and printing tests, the layer thickness was fixed to 25 μm and projection time ranged from 60 s to 225 s depending on the PPF molar mass. Each scaffold was cylindrical with a prescribed diameter of 6 mm and height of 4 mm. After printing, scaffolds were immediately rinsed with acetone, 70 % ethanol (v/v), and distilled water for 15 s each. Finally, the "green" scaffolds were post-cured in a full spectrum UV irradiation chamber for 45 min or 90 min.

2.2.9 Mechanical testing

Tensile testing of 3D printed tensile bars was performed by an Instron (Norwood, MA, USA) 5543 Universal Testing Machine at room temperature (24 ± 1 °C). Following the guidelines from the ASTM standard D638-2014, the strain rate for the tensile test was chosen to be 0.1 mm/(mm·min) to give rupture within 0.5 to 5 min testing time for all 3D printed tensile bars. At least five tensile bars were tested in each group. As expected, these tensile tests resulted in failure at the narrow cross-section portion of the tensile bars. The data were reported as an average value of three individual measurements for each tensile bar. The elastic moduli were calculated as the slope of the initial linear portion of the stress-strain curve. The tensile strength was defined as the stress at failure carried by the specimen during a tensile test.

The mechanical properties of the gyroid scaffolds were studied by compression tests using an Instron 5566 Universal Testing Machine (Norwood, MA, USA). Force and displacement were zeroed prior to compression, with the top plate slightly above the surface of the sample. Samples were compressed at a constant crosshead velocity of 0.5

$mm \cdot min^{-1}$ at room temperature while stress and strain were monitored throughout the experiment. The compressive moduli were calculated using the slope of linear fitting in the linear regime. Compressive strength at fracture (if fracture occurred) was defined as the stress required to fracture the material. The reported results are average values from five individual measurements and the associated errors are the standard deviations.

2.2.10 Micro-computed tomography (μ-CT) analysis

The architecture of 3D porous scaffolds was characterized nondestructively by μ-CT Skyscan 1172 from Bruker (Billerica, MA, USA3D scanning of scaffolds was carried out using the following parameters: 40 kV voltage, medium camera (pixel size = 8.73 μm), no filter, 238 ms camera exposure preset time and 7.0 μm resolution.

2.2.12 Cell culture

Murine fibroblasts, L929 cell line (Sigma-Aldrich, St. Louis, MO), were used per recommendation by ISO Standard 10993-5, which outlines the standards for direct contact assays. L929 cells were cultured with Minimum Essential Medium (MEM) (Sigma-Aldrich, St. Louis, MO) containing 10% horse serum (Sigma-Aldrich, St. Louis, MO) and 1% Penicillin-Streptomycin (Life Technologies, Carlsbad, CA), as outlined by the manufacturer. Cells were plated at 75,000 cells per well into a 24-well polystyrene cell culture plate (Corning Life Sciences, Corning, NY). The cells were grown to ~80% confluence (2 days) prior to beginning the direct contact assay.

2.2.13 Cytotoxicity Assay

A direct contact test was conducted in accordance with ISO Standard 10993-5. Cytotoxicity was assessed at 24 hours. To initiate the test, the media was aspirated from the wells containing cells. Then, a thin film of PPF was placed on top of the cell monolayers in each well. Around 150 µL of media was then added back into each well- enough to cover the well, but keep the thin film from floating above the cell monolayer. The cells were then incubated at 37°C and 5% CO_2 for 24 hours. Afterwards, the cytotoxicity of the material was assessed through fluorescence staining and microscopy.

CHAPTER III

SYNTHESIS AND BIOLOGICAL EVALUATION OF WELL-DEFINED POLY(PROPYLENE FUMARATE) OLIGOMERS AND THEIR USE IN 3D PRINTED SCAFFOLDS

This work has been previously published as

Yuanyuan Luo, Courtney M. Dolder, Jason M. Walker, Ruchi Mishra, David Dean, Matthew L. Becker

Biomacromolecules, 2017, 17(2), 690-697

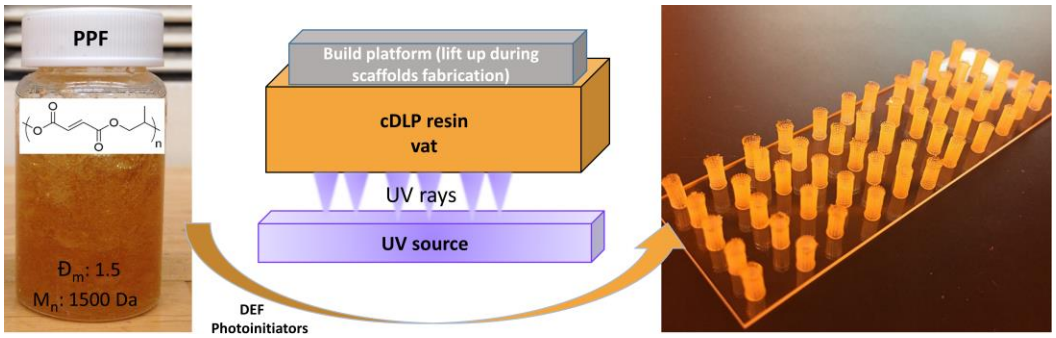

3.1 Abstract

A ring opening polymerization method for synthesizing oligomeric poly(propylene fumarate) (PPF) provides a rapid, and scalable method of synthesizing PPF with well-defined molecular mass, molecular mass distribution ($Đ_m$), and viscosity properties suitable for 3D printing. These properties will also reduce the amount of solvent necessary to ensure sufficient flow of material during 3D printing. MALDI mass spectrometry precisely shows the end group fidelity and size exclusion chromatography (SEC) demonstrates narrow mass distributions (<1.6) of a series of low molecular mass oligomers (700-3000 Da). The corresponding intrinsic viscosities range from 0.0288±0.0009 dL/g to 0.0780±0.0022 dL/g. The oligomers were printed into scaffolds via established photochemical methods and standardized ISO 10993-5 testing shows that the 3D printed materials are non-toxic to both L929 mouse fibroblasts and human mesenchymal stem cells.

3.2 Introduction

Additive manufacturing, also known as three-dimensional (3D) printing, has the potential to revolutionize regenerative medicine[139] and fundamentally alter how surgeons approach complicated reconstructive efforts to treat the results of pathogenesis, trauma, congenital deformity, senescence, or cancer. While numerous 3D printing methods have been reported, photo-crosslinking-based printing methods in particular have shown potential for reliable, high-fidelity rendering of solid-cured polymer scaffolds that are designed to fit defects visualized by medical imaging.[140] Advances in image projection via

digital light printing (DLP) technology have enabled the 3D printing of tissue engineering scaffolds with complex geometric designs coupled with very fine (<50 um) features.[141] However, there are numerous regulatory hurdles that must be overcome in order for this technology to gain approval and arrive at the clinic including the availability of good manufacturing practices (GMP) resins that are photo-crosslinkable (i.e., include photoinitiators, dyes, solvents, and other additives).[142]

While there are many inert photo-crosslinkable resins, very few are non-toxic, implantable and resorbable. The most explored resorbable materials include polylactides,[143] poly(ε-caprolactone),[144] and poly(propylene fumarate) (PPF).[145] With regards to resorption profiles, polylactides have occasionally been found to undergo rapid bulk degradation leading to a localized acidosis and inflammation..[61] Poly(ε-caprolactone) is known to degrade very slowly, sometimes over years,[61, 146] thereby limiting the necessary remodeling or vascularization of neo-tissues. Poly(propylene fumarate) (PPF) was invented in 1994,[147] in part, because of a desire to have a material which has safe and controllable degradation and properties expected to be useful for controlled drug release,[22] stents,[148] blood vessels,[85] nerve grafts,[83] and cartilage[87] tissue engineering, especially bone tissue engineering.[137, 149-151] Since its invention via the step growth polymerization method more than two decades ago, PPF has been investigated with much success as scaffolding materials for skeletal repair. Subsequent reports have improved upon the synthetic methods and resulting materials.

Although there have been many promising pre-clinical studies,[142, 151-156] there are significant barriers to moving PPF into mainstream clinical trials. The first challenge is inherent to the step growth polymerization process in the traditional synthetic method. Previously reported methods to synthesize PPF require high energy input, high vacuum, long reaction times, and result in low conversion (~ 35%)[61] with uncontrolled molecular mass distribution (*e.g.,* $\overline{M_n}$, 500-1200 Da, $Đ_m$ 3-4; $\overline{M_n}$ 750-1500 Da, $Đ_m$ 1.7-3)[61, 157], conjugate-addition side reactions, and unwanted cross-linking, all of which significantly influence the mechanical properties and degradation rates of the final product.[93] Since the viscosity of pure PPF oligomer at 40 ºC is above 24,000 cP,[137] which is significantly different from the ideal viscosity 200 cP[158] in photochemistry based 3D printing resins, diethyl fumarate (DEF) (>50% vol%) is usually added into PPF oligomeric resins to reduce the resin viscosity. Lowering the viscosity of PPF solutions for 3D printing undermines efforts to obtain the highest elastic modulus and fracture strength (which are close to those properties of trabecular bone) of DEF/PPF crosslinked scaffolds, so 25% DEF was suggested in previous reports.[151] And hence, the ideal PPF oligomers for 3D printing should have $\overline{M_n}$ range from around 1000 Da to 2000 Da[151, 158] to satisfy viscosity range of DEF/PPF resin for 3D printing and the mechanical properties of the final printed DEF/PPF scaffolds. However, PPF synthesized from previous reported step growth polymerization methods showed either low yield or wide molecular mass distribution at $\overline{M_n}$ range 1000-2000 Da. Fractional precipitation was often used to obtain PPF samples with molar mass distributions <1.6 for academic stuides.[137] In short, using step growth polymerization, despite clever modifications, it is difficult to reliably and reproducibly synthesize well-defined, low-molecular-mass oligomers on the scale required for widespread 3D printing

applications and commercialization. This more than any other factor has limited the availability of PPF to a select few investigators and limited the quantities of GMP-grade materials, i.e., materials which meet requirements implemented by the FDA. GMP PPF resin is required to push promising PPF-based 3D printed scaffolds forward into large animal models and pilot human trials. Herein we report a scalable method for synthesizing well defined poly(propylene fumarate) using a ring opening polymerization of maleic anhydride and propylene oxide coupled with a post polymerization isomerization reaction.

3.3 Experimental Section

3.3.1 Materials

Maleic anhydride (MAn) (99%) was purchased from Fluka. Propylene oxide (PO) (99.5%), magnesium ethoxide ($Mg(OEt)_2$) (98%), diethylamine (99%, extra pure), hydrochloric acid (HCl) (ACS, 37%), toluene (anhydrous, 99.8%), tetrahydrofuran (THF) (ACS grade), chloroform (ACS) grade, hexanes (98.5%), sodium phosphate dibasic (BioXtra, ≥99.0%), and sodium phosphate monobasic (BioXtra, ≥99.0%) were purchased from Sigma-Aldrich. All chemicals were used as received.

3.3.2 Characterization of chemical structure, molecular weight and thermal properties

^{1}H and ^{13}C Nuclear magnetic resonance (NMR) spectra were recorded with a Varian NMRS 300 MHz instrument. Deuterated chloroform ($CDCl_3$) was used as solvent. Chemical shifts, δ (ppm), were referenced to the residual proton signal.

The chemical structures of PPF samples were further analyzed by a Bruker Ultraflex III Matrix-Assisted Laser Desorption/Ionization Time-of-Flight (MALDI-ToF/ToF) mass spectrometer. The samples were dissolved in $CHCl_3$ at a final concentration of 10 mg/mL. The sandwich method was used with trans-2-[3-(4-tert-Butylphenyl)-2-methyl-2-propenylidene] malononitrile (DCTB) as matrix and NaTFA as salt 10:1. End groups were identified for absolute molecular mass characterization.

FTIR spectra were recorded for film samples cast on potassium bromide (KBr) disks from $CHCl_3$ solution by an Excalibur Spectrometer (FTS 3000 and FTS 4000 Series) with a wavenumber range from 400 cm^{-1} to 4000 cm^{-1}. The molecular mass and molecular mass distribution of each polymer was determined by size exclusion chromatography (SEC). SEC analysis in THF at 35 ^oC was performed on a Viscotek GPCmax VE 2011 GPC Solvent Sample Module with a Waters 2414 Reflective Index Detector, with polystyrene standards of narrow molecular mass distributions (with M_W (g/mol): 580; 1280; 3180; 4910; 10440; 21,810; 51,150; 96,000; 230,900). The thermal properties of PPF were characterized by DSC using TA Q2000 differential scanning calorimeter from -100 ^oC to 100 ^oC at a scanning rate of 10 ^oC /min in order to obtain the glass transition temperature (T_g).

3.3.3 Intrinsic viscosity measurements of PPF polymers

The intrinsic viscosity of PPF samples at five molecular mass levels was measured in THF using an Ubbelohde viscometer at 35 ^oC. Each PPF sample ($\overline{M_n}$: 0.7 kDa, 1.27 kDa, 1.86 kDa, 2.45 kDa, and 3.16 kDa) was weighed and diluted in THF in a volumetric flask (10 mL). Freshly distilled THF was added into the volumetric flask to the 10 mL

mark with a 0.45 um filter and sealed. The capillary viscometer was cleaned with pure THF. A thermostated water bath was heated to maintain the temperature at 35 ^{o}C. The capillary viscometer was pre-equilibrated in the thermostated bath for at least 15 minutes to establish the thermal equilibrium. An injector was used to make the liquid fill up to more than one third of the top ball of the capillary viscometer and then allowed the liquid to flow. A stopwatch was used to record the time when the liquid passed over the first line on the capillary viscometer and stopped recording when the liquid passed the second line on the capillary viscometer. The time of this period was recorded. The flow time was recorded at least five times. The capillary viscometer was refilled by a filter with 5.0 mL of the solution prepared of PPF and THF. The capillary viscometer was put back into the thermostated bath. The flow time was measured and recorded for at least three times as described above. Then 5.0 mL, 3.0 mL and further 1.8 mL or 2.0 mL (results dependent) of pure THF solvent was added into the capillary viscometer using a filter respectively, and the corresponding flow time was measured (n=3).

3.3.4 Representative synthesis of poly(maleic anhydride-co-propylene oxide)

Maleic anhydride (MAn), 70.06 g (714 mmol) and propylene oxide (PO), 50.00 mL (714 mmol) were dissolved in 100 mL of toluene in a 500 mL round-bottom flask at room temperature under a nitrogen atmosphere. After all of the monomers were dissolved in toluene with constant magnetic stirring, 272.34 mg (2.38 mmol, molar ratio of MAn/$Mg(OEt)_2$ = 300:1, $Mg(OEt)_2$ was added to the mixture and the flask was moved into a silicone oil bath equipped with a reflux condenser to initiate the polymerization at 80 °C. The polymerization was allowed to proceed, and aliquots were taken at defined time points

(3 h, 6 h, 18 h, 24 h and 48 h). Similar studies incorporating molar ratio of MAn/$Mg(OEt)_2$ = 200:1, 100:1 were also conducted. After the designated polymerization time, the system was cooled to ambient temperature under nitrogen, and subjected to reduced pressure conditions to remove the volatile materials. The residue was diluted with chloroform ($CHCl_3$) washed with water containing trace amount of hydrochloric acid (HCl) to remove the inorganic $Mg(OEt)_2$ compound. The organic layer was poured into hexanes following rotary evaporation, and the precipitated polymer mixture was re-dissolved in a minimal amount of $CHCl_3$. The residue was then concentrated by rotary evaporation. Poly(maleic anhydride-co-propylene oxide) was obtained after drying the product under vacuum overnight at ambient temperature to remove all volatiles, and then the molecular mass and mass distribution properties were characterized by SEC at each time point after ^{1}H NMR characterization. ^{1}H NMR (300 MHz, Chloroform-*d* δ ppm 1.13-1.41 (d, 3H, $OCH_2CH(CH_3)O$), 4.04-4.36 (m, 2H, $OCH_2CH(CH_3)O$), 5.23-5.30 (m, 1H, $OCH_2CH(CH_3)O$), 6.24-6.42 (m, 2H, C*H*=C*H* (*cis*-configuration)).

3.3.5 General procedure for the isomerization of poly(maleic anhydride-co-propylene oxide)

Diethylamine (0.15 equivalent) was added to poly(maleic anhydride-co-propylene oxide) after dissolving the polymer in $CHCl_3$ in a round-bottom flask at 55 °C for about 20 hours under a nitrogen atmosphere. The mixture was then concentrated by rotary evaporation and washed with phosphate buffer saline solution (0.5M, pH = 6) to remove the diethylamine. The organic layer was then precipitated into hexanes several times to remove impurities. The precipitate was collected and kept in vacuum overnight at room

temperature to remove all volatiles. Then, ^{1}H NMR was used for characterization. ^{1}H NMR (300 MHz, Chloroform-*d* δ ppm 1.11-1.43 (d, 3H, $OCH_2CH(CH_3)O$), 4.09-4.39 (m, 2H, $OCH_2CH(CH_3)O$), 5.21-5.35 (m, 1H, $OCH_2CH(CH_3)O$), 6.83-6.91 (m, 2H, C*H*=C*H* (*trans*-configuration)).

3.3.6 Thin film fabrication

The PPF resin was heated to ensure homogeneity. To create the thin films, a transfer pipette was used to place 5-7 drops of the resin in the middle of a glass slide. A second glass slide was slowly placed on top of the first slide, ensuring that no air bubbles formed while the resin was spread evenly between the two slides. The slides were placed in a UV chamber (3D Systems, Rock Hill, SC) for 30 minutes. After this time, the slides were removed, and a razor blade was used to peel the thin films of partially cross-linked PPF resin off the slides. The films were cut into squares that measured 1 cm along each edge. The cut squares were sandwiched between two slides, to prevent curling, and put back into the UV chamber for 7.5 hours to complete further cross-linking.

3.3.7 Photochemical 3D printing

3D scaffolds were printed using an EnvisionTEC Perfactory® 3 was calibrated to generate a UV mask with a nominal irradiance of 350 $mW \cdot dm^{-2}$. The scaffold geometry was chosen and the design files, which were previously created using SolidWorks software (Dassault Systèmes SolidWorks Corp., Waltham, MA), were obtained. We chose to impose the Schoen Gyroid scaffold pore geometry on cylinders with struts of 400 µm, pores of

1400 µm, and supports on the bottom. Fifty milliliters of resin was poured into the basement plate of the Perfactory® 3. The build file was sent from the computer to the printer using Perfactory® Software Suite 2.6 (EnvisionTEC, Dearborn, MI). The Perfactory® was operated using a 75 mm focal length lens. This allowed for a native resolution of 42 µm in the XY-plane. The enhanced resolution module (ERM), which allows for a native resolution of 21 µm in the XY-plane, was not used for this study. The printing job completed in 4 hours and 11 minutes. The temperature of the resin was approximately 25 °C. Once the scaffolds were finished, the build plate containing the attached scaffolds was removed from the printer. The scaffolds were washed, first with 70% acetone, to remove any uncured resin from within the pores of the scaffolds. The scaffolds were then briefly rinsed with 70% EtOH followed by a rinse with dH_2O. Compressed air was used to gently dry the scaffolds. The scaffolds were then removed from the build plate using a razor blade. The scaffolds were placed onto microscope slides, standing upright, and put into the UV chamber for an additional 8 hours to complete further cross-linking.

3.3.8 Washing protocol

Before beginning the direct contact assay, the thin films were washed. The washing protocol began with a 15-minute soak in Dulbecco's phosphate buffered saline (DPBS) (Life Technologies, Carlsbad, CA) to remove surface debris introduced during production. This was followed by three separate washes in 70% acetone for durations of 30, 20, and 10 min. Between acetone washes, the films were soaked in DPBS to remove excess acetone from the films and to prevent them from drying out. The protocol was finished by

completing two more washes in DPBS, 15 min each. After washing, the thin films were soaked in DPBS for 72 hours in an incubator at 37°C, 5% CO_2. The films were then soaked in fetal bovine serum (FBS) (GE Healthcare, Piscataway, NJ) overnight.

3.3.9 Cell culture

Murine fibroblasts, L929 cell line (Sigma-Aldrich, St. Louis, MO), were used per recommendation by ISO Standard 10993-5, which outlines the standards for direct contact assays. L929 cells were cultured with Minimum Essential Medium (MEM) (Sigma-Aldrich, St. Louis, MO) containing 10% horse serum (Sigma-Aldrich, St. Louis, MO) and 1% Penicillin-Streptomycin (Life Technologies, Carlsbad, CA), as outlined by the manufacturer. Cells were plated at 75,000 cells per well into a 24-well polystyrene cell culture plate (Corning Life Sciences, Corning, NY). The cells were grown to ~80% confluence (2 days) prior to beginning the direct contact assay.

3.3.10 Cytotoxicity assay

A direct contact test was conducted in accordance with ISO Standard 10993-5. Cytotoxicity was assessed at 24 hours. To initiate the test, the media was aspirated from the wells containing cells. Then, a thin film of PPF was placed on top of the cell monolayers in each well. Around 150 µL of media was then added back into each well—enough to cover the well, but keep the thin film from floating above the cell monolayer. The cells were then incubated at 37°C and 5% CO_2 for 24 hours. Afterwards, the cytotoxicity of the material was assessed through fluorescence staining and microscopy.

3.3.11 Microscopy

The scaffolds were imaged using an Olympus Stereoscope (Center Valley, PA) to depict the scaffold features and individually cured layers in greater detail. Live/dead staining was performed to assess the cytotoxicity of the PPF. A solution containing 2μM calcein AM and 4 μM ethidium homodimer-1 (EthD-1) was prepared in DPBS using a cytotoxicity kit (Life Technologies, Carlsbad, CA). Wells containing thin films as well as those serving as controls were incubated with 150 μL of live/dead solution at room temperature for 30 minutes in dark conditions. Cells that were cultured as mentioned previously and then incubated in 70% methanol for 30 minutes prior to incubation in live/dead solution were used as a positive, cytotoxic control. As a negative, noncytotoxic control, cells were cultured in normal conditions on polystyrene culture plates prior to live/dead staining and received no other treatment. After incubation with the live/dead solution, images were taken with an Olympus CKX41 fluorescence microscope outfitted with a 12.8 MP digital camera (Olympus, Center Valley, PA).

3.4 Results and Discussions

Recently, DiCiccio et al. reported the synthesis of PPF using a ring-opening copolymerization of maleic anhydride and propylene oxide with chromium salen as an initiator at 45 °C.[90] The resulting poly(propylene maleate) (PPM) was isomerized using diethyl amine at ambient temperature for 16 hours to yield poly(propylene fumarate). The solid PPF material possessed $\overline{M_n}$ ~17 kDa, molecular mass distribution of 1.6 and less than 1% ether linkage with 99% conversion. Compared with traditional synthesis step

growth methods[157, 159], the chain growth mechanism yields PPM with consistent mass and mass distribution properties, and the reaction is more reproducible. Upon isomerization, it is possible to produce PPF with well-defined properties for further mechanical, toxicity and degradation tests.

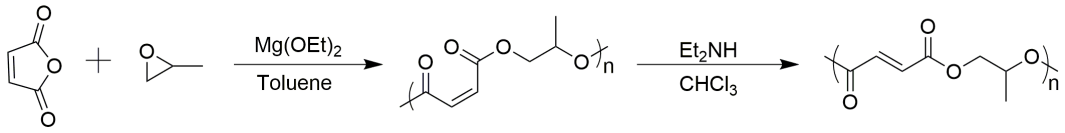

Scheme 3.1. PPF results from an isomerization reaction of PPM in the presence of diethylamine.

PPF synthesized using the methods of DiCiccio et al. results in solid high molecular mass polymers with high viscosity that are not suitable for 3D printing studies as discussed before. Comparing the known toxicity of Cr and Co metals,[160, 161] magnesium ethoxide was chosen as initiator in PPF synthesis in this study.[162, 163] PPM oligomers were synthesized through a chain-growth mechanism using magnesium ethoxide as the initiator. The molecular mass of the PPF can be controlled easily with time and temperature. Unlike other reports of molecular mass distribution which are a result of post precipitation fractionation[137], the molecular mass distribution of oligomeric PPM is generally less than 1.6 prior to precipitation. The catalytic byproducts are ethanol and magnesium oxide both of which are tolerated by biological systems[163], especially at concentrations noted in this method. Following purification, the PPF oligomers synthesized from this method possess well-defined properties including predictable molecular mass and narrow molecular mass distribution. The method is highly reproducible, scalable and amenable to a good manufacturing process (GMP) compared to the traditional step growth PPF synthetic methods. These characteristics may accelerate the application of PPF as a 3D-printable biodegradable synthetic polymer for use in clinical bone tissue engineering applications.

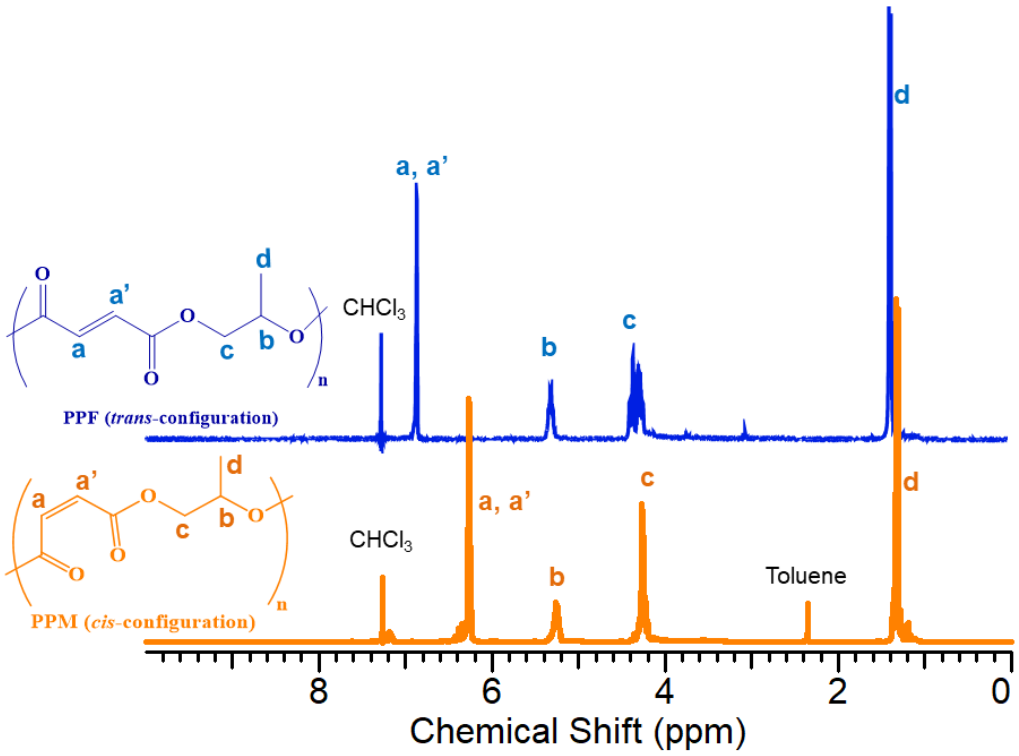

Figure 3.1. ^{1}H NMR for a poly(propylene malate) (PPM) intermediate (bottom) and poly(propylene fumarate) (PPF) (top) shows quantitative conversion from the *cis* stereochemistry to the *trans* configuration.

As shown in Scheme 3.1, poly(maleic anhydride-co-propylene oxide) (PPM) was synthesized via a ring-opening polymerization of maleic anhydride and propylene oxide in toluene using magnesium ethoxide as an initiator. Following purification, the intermediate PPM was further isomerized in chloroform with diethylamine as catalyst to yield PPF.

^{1}H NMR and ^{13}C NMR (Appendix) were used to confirm the known chemical structures of poly(maleic anhydride-co-propylene oxide) and poly(propylene fumarate). The residual solvent used in the purification step can be further removed with longer times under vacuum. The blue spectra in Figure 3.1 showed that PPM was successfully isomerized to PPF with the location of the resonances of the *cis*-alkene protons (δ = 6.2)

on C=C bonds shifting to the expected position for protons in the *trans*-configuration (δ = 6.8) similar to the resonances reported previously.

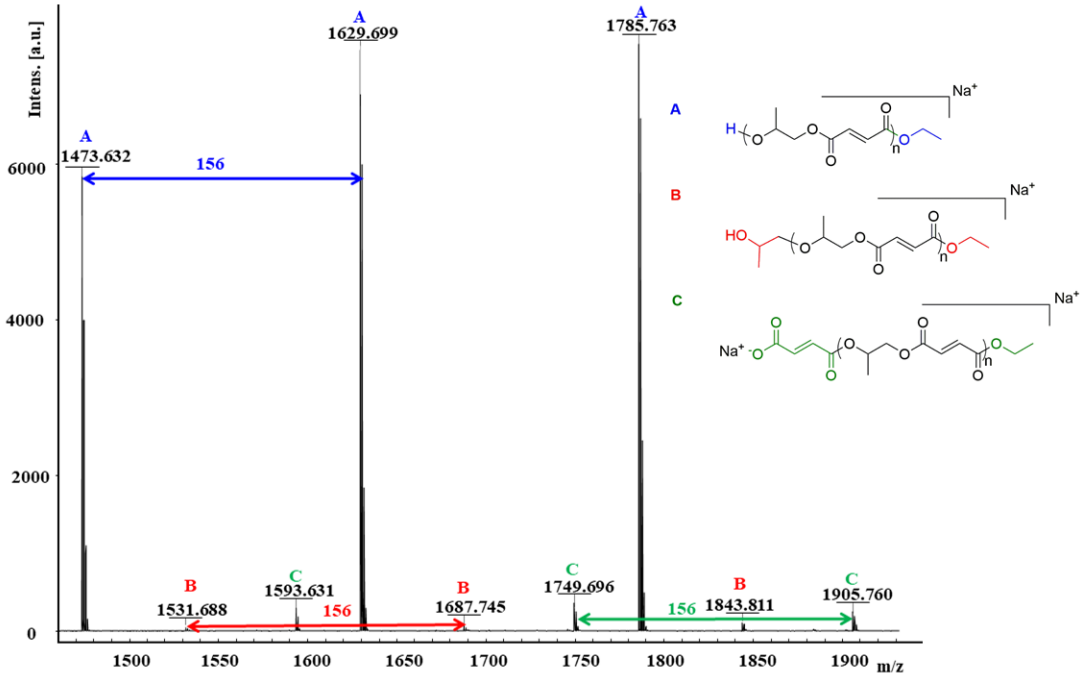

Figure 3.2. Enlarged portion of a MALDI-TOF mass spectrograph of PPF sample number 4 in Table 3.1 showing the repeat unit in PPF and the postulated end group chemistries, which correspond the individual peaks in the distribution depicted in the mass spectrometry data.

Matrix Assisted Laser Desorption Ionization (MALDI) mass spectroscopy was able to precisely determine the mass of the individual materials and the end group populations. At low molecular mass, MALDI was able to determine the molecular mass more precisely that size exclusion chromatography. As seen in Figure 3.2, there are three groups (labeled with A, B, C) of possible end groups in this sample (PPF sample number 4 in Table 3.1). The m/z=156 between two adjacent peaks shows the mass of repeat unit, which equals to the mass of maleic anhydride and propylene oxide. The predominant end group population is an ethoxy group and a proton(A). These characteristics support the successful synthesis of PPF coupled with end group populations. There is no evidence of residual metal from

the initiator in the purified materials. The MALDI spectra of PPF sample number 4 in Table 3.1 and other MALDI spectra of PPF sample number 2 in Table 3.1 are shown in the Appendix.

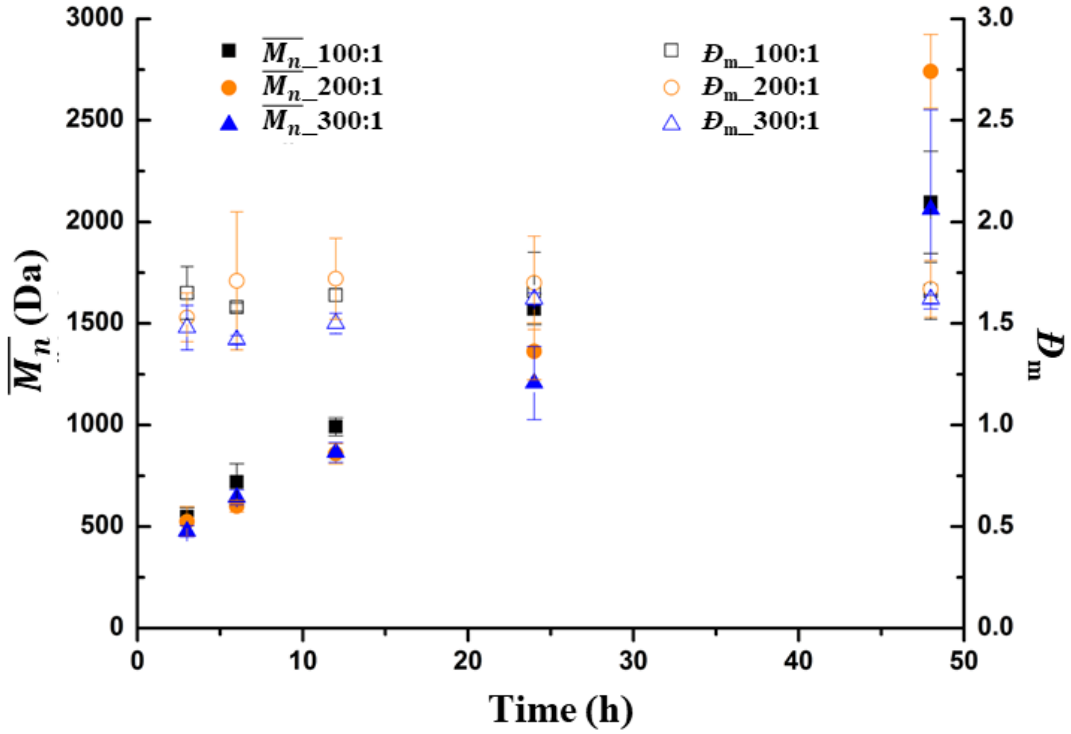

Figure 3.3. A kinetic plot showing the near linear growth of molecular mass with time. Number-average molar mass ($\overline{M_n}$) and molar mass distribution ($Đ_m$) as a function of reaction time for poly(propylene malate) (PPM) intermediates using monomer-to-initiator ratios of 100:1, 200:1, and 300:1.

In Figure 3.3,$\overline{M_n}$ of PPM increased in a nearly linear fashion as the polymerization time increased from 3 h to 48 h, supporting a chain-growth mechanism. The small deviations in$\overline{M_n}$ and $Đ_m$ over multiple reactions demonstrated the reproducibility of this reaction. The molecular mass distribution of all polymerizations was around 1.6 without fractionation. The chain growth method affords more precise control over molecular mass distribution compared to a step-growth mechanism where $Đ_m$ is usually 2 or higher. The yields for the reaction approach 65%, which is significantly greater than the yields for low

molecular mass oligomers in a step growth process. Herein we show this kinetic study can be used for large batch PPF synthesis to target specific molecular mass properties for 3D printing.

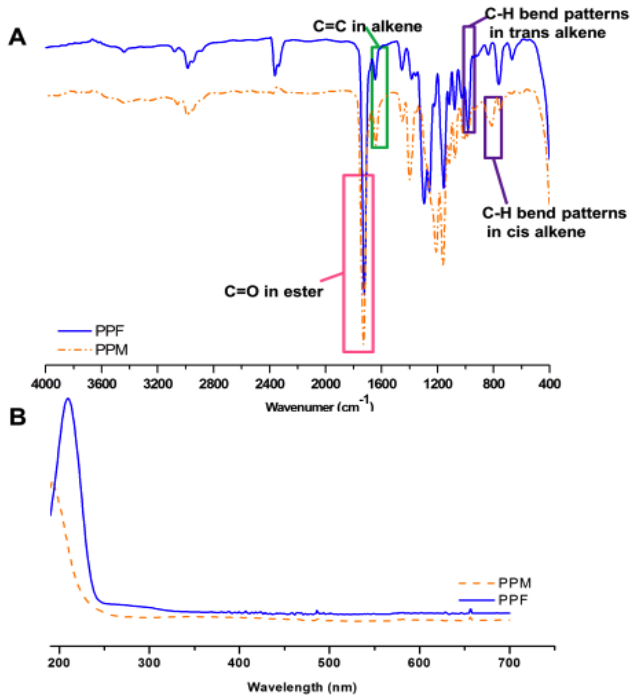

Figure 3.4. (A) FTIR spectra (film, KBr, $CHCl_3$, 400 cm^{-1} – 4000 cm^{-1}) for the PPM intermediate and PPF. The *cis* to *trans* conversion is seen in C-H stretches. (B) Ultraviolet–visible spectroscopy clearly shows (acetonitrile, 190 nm - 700 nm) for a PPM intermediate and PPF. The Stokes red-shift in the π-π* transition indicates the compete conversion of the *cis* to *trans* isomerization.

FTIR and UV-vis spectrophotometry were used to further support the chemical structures of PPM and PPF. In the PPM spectra in Figure 3.4A, the peak at 1715-1740 cm^{-1} represented the unsaturated C=O (ester) stretch, which demonstrated the formation of the ester bond in the PPM synthesis process. Stretches at 2988 cm^{-1}, 1642 cm^{-1}, 1162 cm^{-1}, 814 cm^{-1} showed C-H stretch, C=C (alkene) stretch, O-C (alkoxy) stretch, and C-H (*cis* alkene) bend (broad) patterns separately. In the spectra of PPF, the peak at 1715-1740 cm^{-1} represented the unsaturated C=O (ester) stretch peak. Stretches at 2986 cm^{-1}, 1646 cm^{-1},

1156 cm^{-1}, 984 cm^{-1} were C-H stretch, C=C (alkene) stretch, O-C (alkoxy) stretch and C-H (*trans* alkene) bend patterns respectively. The appearance of C-H (*trans* alkene) bending stretches at 960-990 cm^{-1} in the blue curve demonstrated the isomerization process. These characteristic signals supported the successful synthesis of PPM and isomerization of PPM to PPF.

Table 3.1. Polymer Data with Temp, time, ratios, $\overline{M_n}$,T_g, intrinsic viscosity.

PPF	MAn or PO (mol)	C (mol/ L)	Molar ratio of Monomer / $Mg(OEt)_2$	Time (h)	Temp. (°C)	Molar ratio of PPM/ DEA	Yiel d (%)	$\overline{M_n}$ (Da)	$Đ_m$	T_g (°C)	[η] (dL/g)
1	6.962	7.14	5.7	6	r.t.	6.67	51	700	1.6	-25	0.0288±0.0009
2	2.856	7.14	24	40	80	6.67	65	1270	1.5	-3	0.0490±0.0001
3	7.14	7.14	48	24	80	6.67	55	1496	1.5	-1	0.0513±0.0001
4	2.856	7.14	48	40	80	10	48	1860	1.6	0	0.0529±0.0013
5	2.856	7.14	200	42	80	10	NA	2450	1.6	6	0.0622±0.0006
6	0.714	7.14	200	138	80	6.67	NA	3160	1.7	12	0.0780±0.0022

In Figure 3.4B, the orange curve showed the UV-Visible spectra of PPM intermediate. There was a strong absorbance at 192 nm, which corresponded to the π-π* transition of *cis*-configuration C=C bonds in PPM. In the blue spectrum of PPF, there was a strong absorbance at 210 nm, which was the π-π* transition of *trans*-configuration C=C bond in PPF. The shift results from the conversion of a higher energy *cis*-configuration C=C bonds to a lower energy *trans*-configuration.

A series of PPF polymers having $\overline{M_n}$ of 0.7 kDa, 1.27 kDa, 1.86 kDa, 2.45 kDa, and 3.16 kDa were synthesized using the large batch PPF procedures described in the experimental section (Appendix) using the polymerization parameters set forth in Table

3.1. As shown in Table 3.1, when the number-average molecular mass of PPF increased from 0.7 kDa to 3.16 kDa, the glass transition temperature of PPF increased from -25 °C to 12 °C and the intrinsic viscosity of PPF at 35 °C increased from 0.0288±0.0009 dL/g to 0.0780±0.0022 dL/g. This clearly shows that the smaller molecular mass PPF possess lower glass transition temperature and lower the intrinsic viscosity as expected. At room temperature, PPF sample 1 had near fluid-like property, PPF samples 2-4 were sticky, viscous liquids, and PPF samples 5 and 6 were sticky solids.

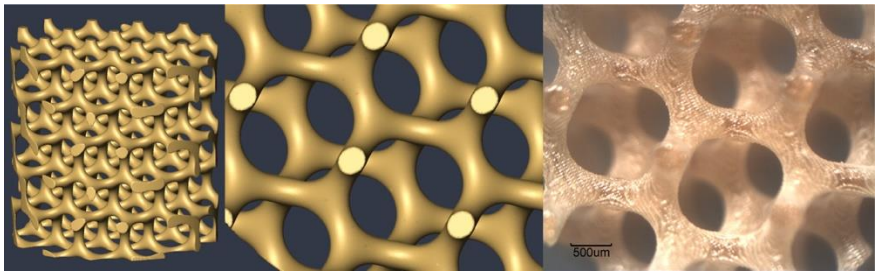

Figure 3.5. 3D printed porous scaffold. Left: CAD file was created in Matlab using the Schoen Gyroid triply periodic minimal surface with 400 μm strut thickness, 1400 μm pore diameter, and 88.2% porosity. Right: CAD file 3D printed as a PPF scaffold using a Perfactory P3 printer.

To ensure that resorbable PPF that was synthesized with the ring opening method could be 3D printed, we tested material with a molecular mass of 1500 Da for 3D printing tests in an EnvisionTEC (Dearborn, MI) Perfactory P3 photo-crosslinking-based device. Diethyl fumarate (DEF) (Sigma-Aldrich, St. Louis, MO) was added to the PPF in a 1:3 mass ratio in order to reduce the viscosity of the polymer. This mixture was then stirred and heated at 50 °C in a fume hood. A resin suitable for photo-crosslinking was then created from the 1:3 DEF:PPF mixture by adding the photoinitiators Irgacure 819 and Irgacure 784 (BASF, Ludwigshafen, Germany) as well as oxybenzone (Sigma-Aldrich), and additional DEF to bring the final resin composition to 1:1 DEF:PPF, 3% Irgacure 819, 0.4% Irgacure

784, and 0.7% oxybenzone. DEF was used as the solvent, along with heat, to dissolve the photoinitiators and oxybenzone prior to their addition to the 3:1 PPF:DEF resin.

A porous, cylindrical scaffold CAD file using the Schoen Gyroid triply periodic minimal surface pore geometry with 400 μm strut thickness, pore diameter of 1400 μm, and porosity of 88.2% was created in was created in Matlab (MathWorks, Natick, MA).[164] The CAD file was 3D printed using the previously described PPF-containing resin using an EnvisionTEC (Dearborn, MI) Perfactory P3 3D printer (Figure 3.5). No morphometric analysis of the scaffolds was done (those comparisons are currently underway); however the 3D printing accuracy was found on quick inspection with a caliper to be identical to scaffolds using PPF synthesized by the step growth method.

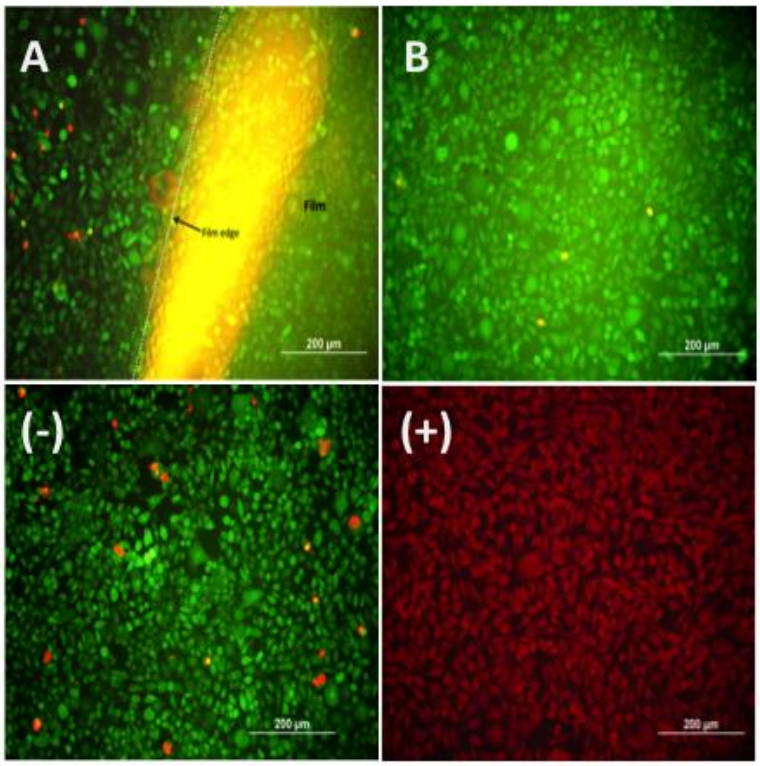

Figure 3.6. Direct Contact Assay. A cytotoxicity analysis was performed in accordance with ISO 10993-5 to confirm in vitro biocompatibility with L929 fibroblasts. Thin films prepared from 1500 Da PPF synthesized by the ring opening method were found to be nontoxic. (A) PPF film edge, (B) under PPF thin film, (-) negative control, (+) positive control. Scale bar = 200 μm.

The same material used for 3D printing was used to prepare 1 x 1 cm square thin films of PPF by placing PPF between two microscope slides and curing the material in a UV light box (Procure 950, 3D Systems, Rock Hill, SC). A direct contact test cytotoxicity test was conducted in accordance with ISO Standard 10993-5.[165] Cytotoxicity was assessed at 24, 48, and 72 h. To initiate the test, a PPF thin film was placed on top of a cell monolayer that was grown onto the coverslip. The cells and thin films were then incubated at 37°C and 5% CO_2 for 24, 48, and 72 h. Afterwards, the cytotoxicity of the material was assessed through fluorescence microscopy using a live/dead assay where calcein AM (green) identified live cells and ethidium homodimer (red) located dead cells. The data show near quantitative viability. The images shown are at 24h. The direct contact assay found this material to be nontoxic (Figure 3.6).

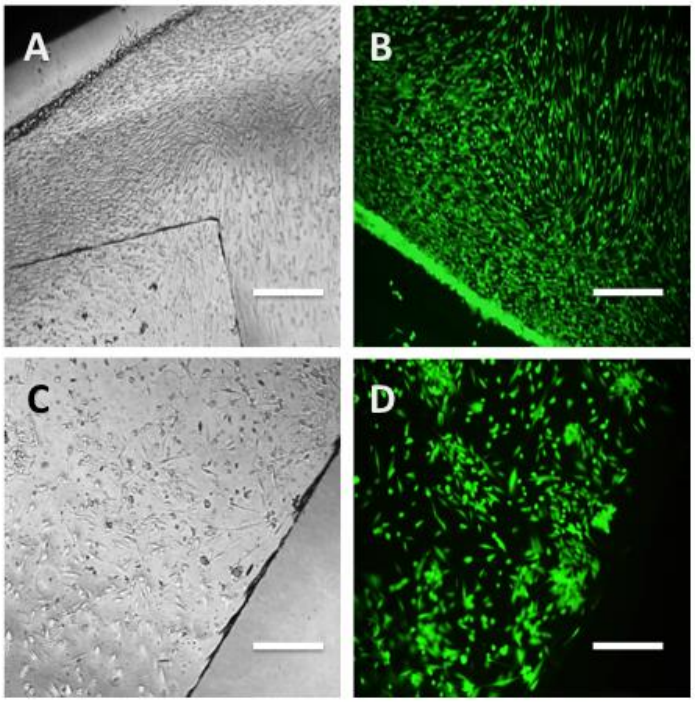

Figure 3.7. Cytotoxicity analysis was performed to confirm the in vitro biocompatibility of human bone marrow-derived human mesenchymal stem cells (RoosterBio, Frederick, MD). Bright field micrscopy images (A,C) and fluorescent (B,D) images of hMSCs in contact with PPF printed films using a direct contact assay (top) or cultured directly on the films. Scale bar = 500 μm.

The same PPF printed thin films used for the direct contact assay were also used as a substrate to culture cells that are used in our current application, bone tissue engineering. Those cells are bone marrow-derived human mesenchymal stem cells (hMSCs) obtained from RoosterBio (Frederick, MD). Again, no toxicity was observed in direct contact assays or when cultured on the films. The cells attached and proliferated well, as is the case with PPF synthesized by the step growth method (Figure 3.7).

3.5 Conclusions

The use of a ring opening method to synthesize PPF is significant in that it enables a scalable, translationally relevant method of PPF synthesis. In addition, the precisely controlled molecular mass, molecular mass distribution and viscosity properties facilitate a predictable pathway for GMP certification. Narrow molecular mass distribution and highly reliable viscosity should afford predictable and reliable mechanical performance and long-term resorption profiles for this material. Finally, narrow molecular mass distribution and reliable viscosity will allow for the reduction in the amount of solvent used to the minimum needed to ensure sufficient flow of material during 3D printing. Collectively these properties may bridge the resorption time gap in highly accurate, photo-crosslinked 3D printed materials between 1 and 2 months for many polylactides and 3-5 years for poly(ε-caprolactone)[166]. This is a critical window for the presence and absence of a scaffold biologically. Initially the presence of a scaffold facilitates either seeded and/or host cells and vasculature to infuse the tissue defect space. Thereafter, in tissues that require remodeling to take on their adult function, the absence of scaffolding material is essential.

Studies covering the molecular mass dependent mechanical and degradation properties of 3D-printed PPF scaffolds are ongoing.

3.6 Acknowledgement

Partial support was provided by the Akron Functional Materials Center and the Army, Navy, NIH, Air Force, VA, and Health Affairs to support the AFIRM II effort under award No. W81XWH-14–2-0004. The US Army Medical Research Acquisition Activity is the awarding and administering acquisition office for award No. W81XWH-14–2-0004. Opinions, interpretations, conclusions, and recommendations are those of the authors and are not necessarily endorsed by the US Department of Defense.

CHAPTER IV

3D PRINTING OF POLY(PROPYLENE FUMARATE) OLIGOMERS: EVALUATION OF RESIN VISCOSITY, PRINTING CHARACTERISTICS AND MECHANICAL PROPERTIES

This work has been previously published as

Yuanyuan Luo, Gaëlle Le Fer, David Dean and Matthew L. Becker

Biomacromolecules, 2019, 20(4), 1699-1708

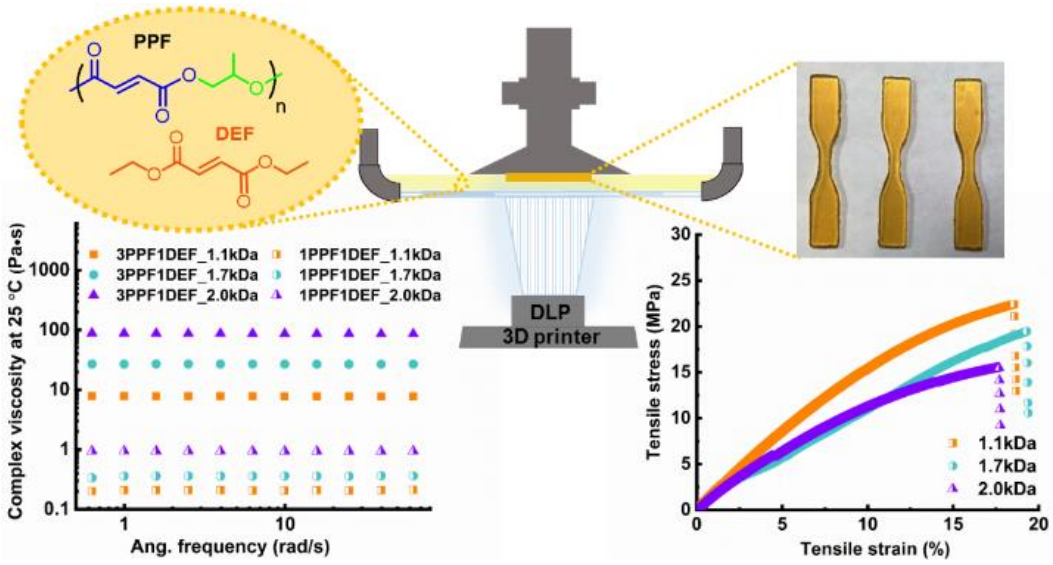

4.1 Abstract

Complex three-dimensional (3D) pore geometries, useful for tissue engineering scaffolds, can be fabricated *via* photo-crosslinking of resorbable poly(propylene fumarate) (PPF) resins using stereolithography (SLA) and/or continuous digital light processing (cDLP) methods. Physico-chemical parameters inherent to 3D printable resin design, include viscosity, polymer concentration, degree of polymerization, and resin printing temperature. We report here on our study of these parameters and their influence the cDLP 3D printing process and the resulting mechanical properties. A series of PPF oligomers were synthesized by the ring-opening copolymerization (ROCOP) of maleic anhydride and propylene oxide followed by a base-catalyzed isomerization. The resin viscosities were measured as a function of number-average molecular mass ($\overline{M_n}$) of the PPF oligomers (1.1 kDa, 1.7 kDa and 2.0 kDa), concentrations of PPF in the reactive diluent diethyl fumarate (DEF) (50 and 75 wt. %) and resin temperature (25 °C to 55 °C). The zero-shear viscosity (η_0) of the resins was found to be temperature-dependent and follow a linear Arrhenius relationship. Tensile tests demonstrated mechanical properties within the range of trabecular bone, with the ultimate strength at break above 15 MPa and elastic moduli between 178 and 199 MPa.

4.2 Introduction

Precise pathways to fabricate three-dimensional (3D) scaffolds for bone tissue engineering are evolving rapidly with advances in 3D printing techniques and synthetic methods to generate polymeric biomaterials.[26, 39, 167-172] Compared to traditional porous

scaffold fabrication methods including salt leaching, gas foaming, and phase separation, 3D printing affords significant flexibility in the design of complex, patient-specific scaffold geometries (*e.g.*,for craniofacial defects), and control over internal pore and strut size, porosity, and pore interconnectivity, all of which are important to physiological response to the scaffold at the wound site.[158, 173, 174] Selection of materials with appropriate resorption time and Computer Aided Design (CAD) geometries influence mechanical properties that are important and interdependent for bone tissue engineering.[35, 175]

The use of continuous digital light processing (cDLP), also known as dynamic mask photolithography, is a high resolution photochemical printing modality where a photosensitive liquid resin is solidified with a DLP (Digital Light Processing) projector chip *via* UV and/or visible light in a layer-by-layer process.[170, 173, 175, 176] Compared to other 3D printing techniques such as fused deposition modeling (FDM) or stereolithography (SLA), cDLP printing methods are relatively fast and possess lateral resolution at 10-100 μm scales.[41, 173, 175] Recently, new materials are emerging as alternatives to previously studied resorbable polymers for cDLP printing.[175] One such resorbable polymer is poly(propylene fumarate) (PPF), an unsaturated polyester which degrades in the body into a Krebs-cycle constituent (fumaric acid) and a food additive (propylene glycol).[177] PPF was synthesized for the first time in 1994 by Mikos and co-workers[178] and has been used widely in cDLP-based 3D printing.[20, 179] This polymer has been used in a number of medical applications, such as controlled drug release,[180, 181] vascular stents,[88] nerve grafts,[83] blood vessel engineering,[85] hydrogels,[182] cartilage[87, 183] and bone tissue engineering.[96, 113, 184-186] Unlike previous reports which used oligomeric resins from a step growth polymerization process, we recently reported the synthesis of PPF and PPF copolymers

using a ring-opening copolymerization (ROCOP) method that provides precise control over molecular mass and molecular mass distribution ($Đ_m$).[41, 107] Molecular mass and mass distribution have significant effects on viscosity properties.

In cDLP-based 3D printing, it is important to keep the viscosity of the printable resin low (*e.g.*,0.25 Pa·s for a pentaerythritol tetra-acrylate resin, 5 Pa·s for ceramic suspensions, and ~10 Pa·s for polymer with carbon nanotube composites) to avoid print failures.[187, 188] Lower viscosities are necessary for rapid printing to allow a new layer of liquid resin to flow into the small gap between the bottom surface of the resin tray and the previous cured solid layer and to maintain dispersion of resin additives.[167, 175, 188, 189] PPF, by itself, at a molecular mass relevant to tissue engineering (<3500 Da), is a viscous polymer (*e.g.*,for a $\overline{M_n}$ = 1.5 kDa, $Đ_m$ = 1.7 PPF, the zero-shear viscosity at 40 °C is 2370 Pa·s).[137] A resin formulation containing pure PPF cannot be used for photochemical-based 3D printing without dilution in a solvent because the high viscosity hinders precise layer thickness control and increases curing time.[145, 158] A light-reactive or non-reactive solvent is added to the resin to reduce the viscosity in many cDLP 3D printing studies.[173, 189] Nevertheless, there is a maximum amount of solvent that can be added into a resin before network structures are significantly altered, mechanical properties are dramatically reduced, or 3D printing fails entirely.[96, 167, 173, 179] To consistently and efficiently 3D print PPF-based scaffolds using photocrosslinking-based cDLP methods, there is an overarching need to understand the factors that reduce the viscosity of the PPF resin while maintaining sufficient flow during printing, resin additive dispersion, and the intended scaffold's mechanical strength.

Several studies[35, 176] have shown that the compressive mechanical properties of PPF-based polymeric scaffolds and PPF-based composite scaffolds are comparable to those of human trabecular bone. In studies where the PPF oligomers used were synthesized using step growth polymerization methods, the material is known to have a relatively broad molecular mass distribution (*e.g.*, $Đ_m > 2$).[97, 190-194] As the $\overline{M_n}$ of PPF oligomers and the scaffold geometry have been shown to significantly influence the degradation profile of 3D printed porous PPF scaffolds in accelerated degradation conditions,[35] it is important to understand the mechanical property changes of 3D printed materials as a function of the molecular mass distribution and $\overline{M_n}$ of the PPF used.

Herein, we evaluate the effect of temperature, PPF to the reactive diluent diethyl fumarate (DEF) mass ratio and degree of polymerization (DP) of PPF on resin viscosity, print layer thickness, and the mechanical properties of fully-processed (*i.e.*, cleaned and post-cured) scaffolds. The incorporation of DEF between the crosslinks formed between PPF chains is likely to dramatically affect 3D printing time as well as the scaffold's resulting mechanical properties. Three PPF oligomers (1.1 kDa, 1.7 kDa, and 2.0 kDa) were used to formulate printable resins at different PPF to DEF ratios (1:1 and 3:1) and printing temperatures to assess the influence of the $\overline{M_n}$ of PPF, if any, on the 3D printing process. Additionally, FTIR measurements and swelling tests were performed to evaluate the crosslinking density of 3D printed tensile bars as a function of the $\overline{M_n}$ of PPF. Finally, the corresponding mechanical properties were measured to assess their potential use for trabecular bone tissue engineering scaffolds.

4.3 Experimental Section

4.3.1 Materials

Maleic anhydride (MAn) (99 %), propylene oxide (PO) (99.5 %), magnesium ethoxide ($Mg(OEt)_2$) (98 %), diethylamine (99 %, extra pure), toluene (anhydrous, 99.8 %), tetrahydrofuran (THF) (ACS grade), chloroform ($CHCl_3$) (ACS grade), diethyl ether (≥ 99.7 %), sodium phosphate dibasic (BioXtra, ≥ 99.0 %), sodium phosphate monobasic (BioXtra, ≥ 99.0 %), diethyl fumarate (DEF, ≥ 98.0 %), phenylbis(2,4,6-trimethylbenzoyl)phosphine oxide (BAPO) (97 %), and oxybenzone were purchased from Sigma-Aldrich (St. Louis, MO, USA). Irgacure 784 was purchased from Gelest (Morrisville, PA, USA). All chemicals were used as received.

4.3.2 Methods

Proton (^1H) NMR experiments were performed in $CDCl_3$ at 25 °C using a Varian (Palo Alto, CA, USA) Mercury NMRS 300 spectrometer. All chemical shifts were recorded in parts per million (ppm) relative to the reference peak solvent: chloroform at δ = 7.26 ppm.

The relative molecular masses and the molecular mass distributions ($Đ_m$) of PPF oligomers were determined by size exclusion chromatography (SEC) on a Tosoh Bioscience GmbH (Griesheim, Germany) EcoSEC HLC-8320GPC with TSKgel GMHHR-M columns in series at 45 °C. The sample concentrations were 10 $mg \cdot mL^{-1}$. Tetrahydrofuran (THF) was used as eluent flowing at 1.0 $mL.min^{-1}$. The detector used in

this determination was a refractive index detector (RI) and a series of polystyrene (PS) standards of narrow molecular mass distributions (with of $\overline{M_w}$ (g·mol^{-1}): 500; 578; 1010; 2420; 5970; 10200; 18100; 37900; 96400; 190000; 427000; 706000; 1090000; 2110000; 5480000) were used to determine the relative molecular mass.

MALDI-ToF mass spectra were recorded on a Bruker (Billerica, MA, USA) Ultra-Flex III MALDI-ToF/ToF mass spectrometer equipped with a Nd:YAG laser emitting at 355 nm. The instrument was operated in positive ion mode. All samples were dissolved in chloroform at a final concentration of 10 mg·mL^{-1}. Trans-2-[3-(4-tert-butylphenyl)-2-methyl-2-propenylidene] malononitrile (DCTB) (20 mg·mL^{-1}) served as a matrix and sodium trifluoroacetate (NaTFA) (10 mg mL^{-1}) as a cationizing agent. These materials were prepared and mixed in a ratio of 10:1. Matrix and sample solutions were applied to the MALDI-ToF target plate by the sandwich method. FlexAnalysis software was used to analyze MALDI-ToF data.

The thermal properties of PPF oligomers were characterized by differential scanning calorimetry (DSC) using a TA Instruments (New Castle, DE, USA) Q200 instrument from -30 to 30 °C at a scanning rate of 10 °C·min^{-1}, under nitrogen atmosphere with a flow rate of 40 mL·min^{-1}. The glass transition temperature (T_g) was determined from the midpoint of the heat flow transition in the second heating cycle.

4.3.3 Complex viscosity of PPF:DEF solutions

PPF oligomers from Table 4.1 were diluted in DEF to reduce the viscosity. The viscosity properties of two mass ratio resins, 3:1 and 1:1 (PPF:DEF), were investigated by

performing complex viscosity measurements. Linear viscoelastic properties of PPF:DEF solutions were measured using an AR-G2 rheometer (TA Instruments) at frequencies ranging from 0.1 Hz to 100 Hz (0.6 to 628.3 rad·s^{-1}) at 10 °C temperature intervals of 25 °C, 35 °C, 45 °C and 55 °C. Oscillatory shear measurements were conducted using a 40 mm 2° diameter steel cone with a truncation gap of 55 μm to measure the complex viscosity (η^*) and deduce the zero-shear viscosity (η_0) at 5 % strain.

4.3.4 Resin formulation for 3D printing

Photoinitiators phenylbis(2,4,6-trimethylbenzoyl)phosphine oxide (BAPO), Irgacure 784 and a radical scavenger oxybenzone (HMB) were added to the PPF:DEF solutions at 3 %, 0.4 % and 0.7 % by weight, respectively. The resins were heated at 50 °C under continuous magnetic stirring to fully dissolve the two photoinitiators and the radical scavenger.

4.3.5 Cure tests of PPF-based resins for 3D printing

Cure tests of PPF-based resins were performed to determine the optimal printed layer thickness and UV exposure time and to investigate the effect of the molecular masses ($\overline{M_n}$) of PPF oligomers on these paramaters. Formulated resin (20 mg) was placed in the middle of the resin tray on an EnvisionTEC (Dearborn, MI) Micro HR 279 3D printer which uses a 405 nm LED UV light projector with an irradiance of 225 mW/dm^2. After irradiation with UV for varying time durations (*i.e.*, 45, 60, 90, 120 and 180 s), the uncured liquid resin was gently removed by tissue paper. The resulting film was peeled off the resin

tray with a razor blade and the thickness of the cured film was measured by a digital caliper (Marathon, Vaughan, Ontario, Canada) with 10 μm precision.

4.3.6 Photochemical 3D printing of tensile bars

Tensile bars were printed from liquid resins using an EnvisionTEC Micro HR 279 printer and a computer-aided design (CAD) file of American Society of Testing Materials (ASTM) D638 type V model at a scale of 50 %. The exposure time was 120 s for each layer with a designed layer thickness of 50 μm. Each print was finished in about 4 h at 22-24 °C, after which the tensile bars were gently rinsed with acetone three times and dried with compressed air. The green tensile bars were then placed between two microscope slides for 20 min to post-cure in a full spectrum UV irradiation chamber (at ambient temperature (20 ± 2 °C). At least five tensile bars were 3D printed from each resin formulation for further characterization.

4.3.7 Fourier transform infrared spectroscopy (FTIR)

FTIR spectra were recorded using a Shimadzu (Kyoto, Japan) MIRacle 10 ATR-FTIR with a spectral range from 400 to 4000 cm^{-1}. Repetitive scans (32) were collected and averaged. Three tensile bars made from each resin group were tested. FTIR spectra were shown in absorption mode. Ratios of the alkene C=C stretching signal (1665 cm^{-1} to 1615 cm^{-1}) to carbonyl C=O asymmetric stretching signal (1800 cm^{-1} to 1665 cm^{-1}) before and after 3D printing of PPF:DEF resins were compared using the differences in the area ratio of these two characteristic stretches using OriginPro™ 2017 software.

4.3.8 Swelling test

The crosslinked samples (*i.e.*, films from curing test and tensile bars) was submerged into a capped glass vial with 20 mL of toluene for 24 h on a shaking bed (70 rpm) at ambient temperature (20 ± 2 °C), and the mass of each sample (W_s) was recorded. Then the sample was dried under vacuum for 24 h and the final dried mass of the sample (W_f) was recorded. The swelling degree (SD) is defined by the following equation:

$$SD = \frac{W_s - W_f}{W_s} \tag{4.1}$$

A balance with precision of 0.1 mg was used to obtain the mass information.

4.3.9 Tensile mechanical test

Dimensions (*i.e.*, length overall (LO), width overall (WO) and thickness (T)) of each tensile bar were measured using a digital caliper with a 0.01 mm precision. Tensile testing of 3D printed tensile bars was performed by an Instron (Norwood, MA, USA) 5543 Universal Testing Machine at room temperature (24 ± 1 °C). Following the guidelines from the ASTM standard D638-2014, the strain rate for the tensile test was chosen to be 0.1 mm/(mm·min) to give rupture within 0.5 to 5 min testing time for all 3D printed tensile bars. At least five tensile bars were tested in each group. As expected, these tensile tests resulted in failure at the narrow cross-section portion of the tensile bars. The data were reported as an average value of three individual measurements for each tensile bar. The elastic moduli were calculated as the slope of the initial linear portion of the stress-strain

curve, by linear fitting of the data from the strain range from 0 % to 0.1 %. The tensile strength was defined as the stress at failure carried by the specimen during a tensile test.

4.3.10 Statistics

Statistical analysis was performed using one-way analysis of variance (ANOVA) with Tukey method to assess significance of the layer thickness variation seen in the cure tests, external dimensions of tensile bars, swelling tests, FTIR test and tensile properties using OriginPro^{TM} 2017 software. A p-value < 0.05 was considered significant. All tests were performed in triplicate unless otherwise noted. Quantitative values provided are mean ± standard deviation of the mean.

4.3.11 Synthesis of poly(propylene maleate) (PPM) oligomers by ring-opening copolymerization

The route to synthesize PPF oligomers has been described previously.[41] As shown in Scheme 4.1, MAn and PO were dissolved in toluene at room temperature. Then, a designated amount of $Mg(OEt)_2$, used both as initiator and catalyst, was added to the solution and the copolymerization was performed at 80 °C, with constant stirring and under an inert atmosphere. After the desired polymerization time, the mixture was cooled to room temperature and the poly(propylene maleate) (PPM) was recovered by precipitation in diethyl ether and then dried under vacuum to afford a viscous orange polymer.

4.3.12 Procedure for the isomerization of PPM

PPM oligomers were isomerized (from *cis* to *trans*) thereby creating poly(propylene fumarate) (PPF). Briefly, PPM was dissolved in chloroform, to reach a concentration of 1 mol·L^{-1} of double bond residues. Diethylamine (Et_2NH) (0.15 eq/double bond residue) was added and the solution was heated at 60 °C, for 24 h, under an inert atmosphere. The organic layer was washed with 1 M sodium phosphate aqueous solution (pH = 6) and the copolymer was recovered by rotary evaporation and dried under vacuum to afford a viscous orange polymer. In this way, the desired series of three PPF oligomers were synthesized with number-average molecular masses ($\overline{M_n}$) of 1.1 kDa, 1.7 kDa and 2.0 kDa, as determined by SEC in THF. Detailed synthesis conditions and molecular characteristics are summarized in Table 4.1.

^{1}H NMR of PPF oligomers (300 MHz, 298 K, $CDCl_3$) δ (ppm) = 1.11−1.43 (d, 3H, $OCH_2CH(CH_3)O$), 4.09−4.39 (m, 2H, $OCH_2CH(CH_3)O$), 5.23−5.35 (m, 1H, $OCH_2CH(CH_3)O$), 6.83−6.92 (m, 2H, C*H*=C*H* (*trans*-configuration). Representative ^{1}H NMR spectra of PPF oligomer can be found in Appendix.

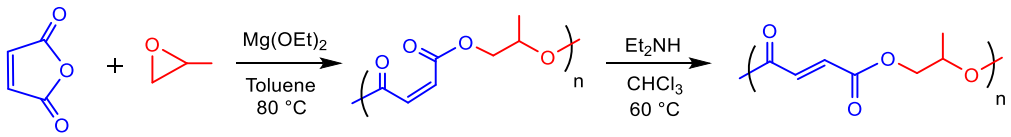

Scheme 4.1. Preparation of poly(propylene maleate) oligomers by ring-opening copolymerization of maleic anhydride and propylene oxide and a subsequent isomerization into poly(propylene fumarate).

4.4 Results and Discussion

The investigation of how viscosity influences the cDLP 3D printing process and the mechanical properties of the resulting scaffolds will aid in the future development of novel resins. Recent improvements in the synthesis of PPF afford better control of molecular mass and molecular mass distribution over traditional step growth polymerization methods. Three PPF oligomers (*i.e.*, 1.1 kDa, 1.7 kDa, and 2.0 kDa) were synthesized by ring-opening copolymerization (ROCOP) of maleic anhydride (MAn) and propylene oxide (PO) and subsequent isomerization reactions.

Table 4.1. Synthetic conditions and characterization of poly(propylene fumarate) oligomers

PPF	**MAn (mol)**	**PO (mol)**	**Monomer Conc. (mol·L^{-1})**	**Molar ratio of MAn/Mg(OEt)$_2$**	**Time (h)**	$\overline{M_n}$ **[a] (kDa)**	$Đ_m$ **[a]**	T_g **[b] (°C)**
1	1.8	1.8	7.14	24	16	1.1	1.28	-5.9
2	1.8	1.8	7.14	48	36	1.7	1.29	-3.5
3	1.8	1.8	9.00	48	50	2.0	1.61	11.8

[a]Determined by SEC in THF at 45 °C with RI detector using PS standards, [b]Determined by DSC

The synthetic conditions and the corresponding molecular characteristics are summarized in Table 4.1. The structures were confirmed by ^{1}H NMR spectroscopy, and the number-average molecular mass values ($\overline{M_n}$) and the molecular mass distribution values ($Đ_m$) were assessed by size exclusion chromatography (SEC) (Figures S5 and S6). The three mass values obtained correspond to the peak mass values from MALDI-ToF spectra (Figure S7). Moreover, the T_g values determined by differential scanning

calorimetry (DSC) are below the ambient temperature for the three PPF oligomers, indicating a viscous state.

Preparation of low viscosity polymer resins that are able to flow like simple liquids is an important challenge in Stereolithography (SLA) and continuous Digital Light Processing (cDLP) photo-crosslink-based 3D printing of PPF and other oligomers. The viscosity of resins for cDLP printing are generally below 10 Pa·s to avoid the structure being destroyed as it is extracted with the basement plate from the vat due to capillary forces as the construct is drawn out of from the cDLP vat once each layer is printed.[187, 188] Moreover, low viscosities are necessary to allow a new layer of liquid resin to flow into the small gap between the bottom surface of the resin tray and the previous photo-crosslinked solid layer after it is raised from the basement plate, to maintain print speed and afford fine structures within the printed product.[158, 193]

Three PPF oligomers were used for the preparation of six resin formulations of PPF:DEF to investigate their complex viscosity (η^*) as functions of number-average molecular mass ($\overline{M_n}$) of PPF, PPF to diethyl fumarate (DEF) weight ratios (*i.e.*, 1:1 and 3:1), and temperature. The complex viscosity (η^*) of each PPF:DEF resin formulation was measured at four different temperatures (25 °C, 35 °C, 45 °C, and 55 °C) and the zero-shear viscosity (η_0) calculated by extrapolation of the complex viscosity to zero angular frequency from a plot of complex viscosity *versus* angular frequency (Figure 4.1A). The zero-shear viscosity data as a function of number-average molecular mass ($\overline{M_n}$) of PPF are presented in Figure 4.1B.

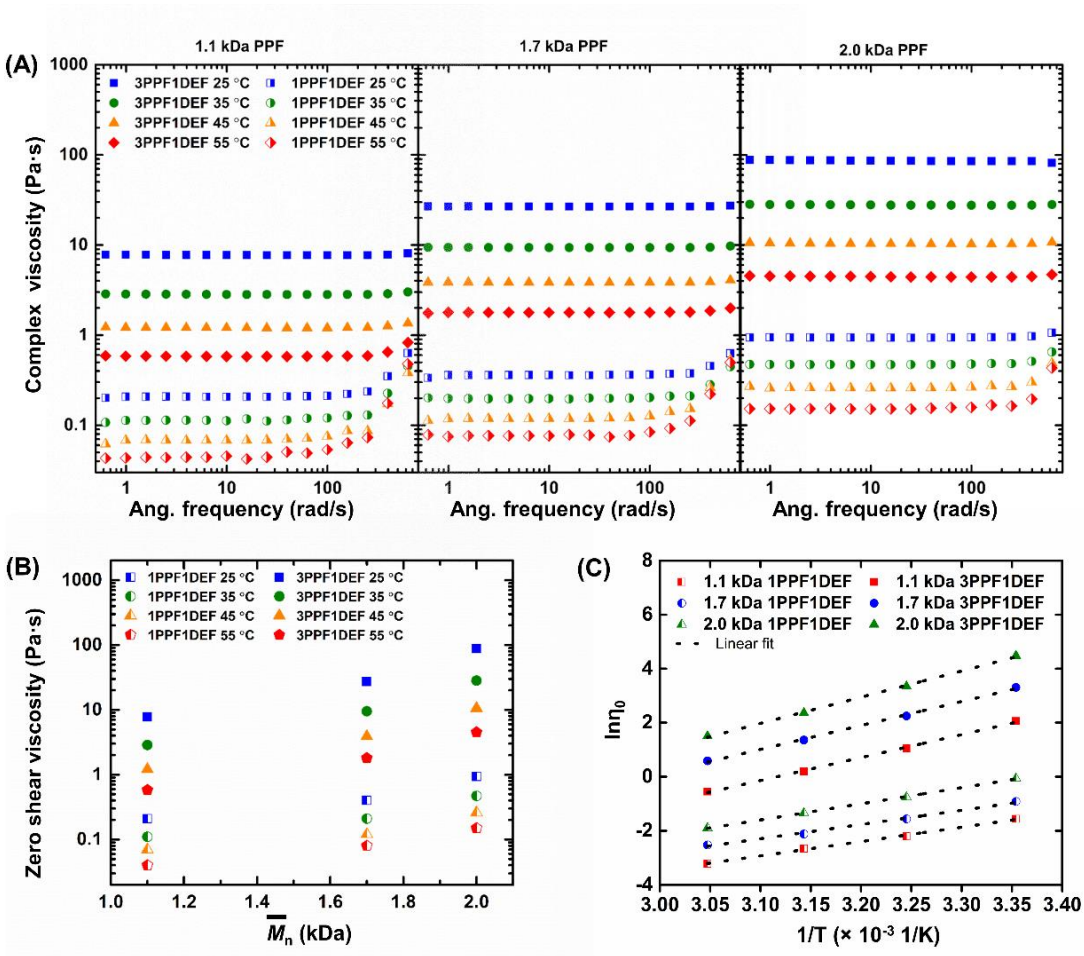

Figure 4.1. (A) Complex viscosity (η^*) of PPF/DEF solutions (without photoinitiators and radical scavenger) as a function of temperature and number-average molecular mass ($\overline{M_n}$) of PPF oligomers (1.1 kDa PPF, 1.7 kDa PPF and 2.0 kDa PPF). (B) Zero-shear viscosity (η_0) of PPF:DEF solutions as a function of temperature, PPF to DEF weight ratio and number-average molecular mass ($\overline{M_n}$) of PPF oligomers. (C) Temperature dependence of zero-shear viscosity (η_0) of PPF:DEF solutions (without photoinitiators or radical scavenger) as a function of PPF to DEF weight ratio for three number-average molecular masses ($\overline{M_n}$) of PPF oligomers, following an Arrhenius model.

Influences of various physical parameters were evaluated separately. The zero-shear viscosity values (η_0) obtained for the PPF:DEF weight ratio 3:1 (solid symbols in Figure 4.1B, at each temperature and for each molecular mass, were found to be systematically higher, about one order of magnitude higher, than values corresponding to the PPF:DEF weight ratio 1:1 (half solid symbols in Figure 4.1B). This suggests that a

higher wt.% of PPF led to an increase in complex viscosity when DEF is used as a diluent. Similarly, an increase in the $\overline{M_n}$ of PPF results in an increase in the zero-shear viscosity (η_0) of the PPF:DEF resin. For example, at 25 °C, for the 1:1 PPF:DEF weight ratio, an increase in the $\overline{M_n}$ of PPF from 1.1 kDa to 2.0 kDa resulted in an increase in the η_0 from 0.21 to 0.94 Pa·s. This indicates that increasing the PPF chain length will increase the zero-shear viscosity (η_0). The increases in η_0 are within one order of magnitude for the PPF:DEF weight ratio 1:1. Temperature also showed a significant influence on the solution viscosity. For example, in the PPF:DEF weight ratio 3:1, with PPF of $\overline{M_n}$ of 2.0 kDa, increasing the temperature from 25 °C to 55 °C leads to a decrease in η_0 from 88.2 Pa·s to 4.5 Pa·s.

Numerous expressions have been suggested for representing the variation of liquid viscosity upon temperature through available experimental data, to predict viscosity values.[195, 196] For this purpose, ln η_0 plotted versus 1/*T* (Figure 4.1C) has revealed a linear behavior, indeed, the temperature dependence of zero-shear viscosity could be linearly fitted using an Arrhenius model:

$$\ln \eta_0 = \frac{E_a}{R}\left(\frac{1}{T}\right) + \mathrm{A}' \tag{4.2}$$

where *T* is the absolute temperature in degree Kelvin, E_a is the activation energy for flow, *R* is the Universal Gas Constant (= 8.3144598(48) $J \cdot K^{-1} \cdot mol^{-1}$) and A' is a constant. The activation energy of each resin composition can be obtained from the slope of corresponding linear fit in Figure 4.1C. The activation energies of PPF:DEF 1:1 resin group were in a 44-50 $kJ \cdot mol^{-1}$ range, which was lower than the values obtained for the PPF:DEF 3:1 resin group, 71-81 $kJ \cdot mol^{-1}$. Moreover, in each group, the 1.1 kDa PPF led to a lower activation energy, than 1.7 kDa and 2.0 kDa PPF, even if the gaps are narrow. From the

kinetic theory of fluids, it is known that the activation energy of viscous fluid flow is equal to the work to be done to transfer components of the fluid, here PPF and DEF, depend on their intermolecular-interaction energy.[197] The differences in activation energy can be explained by differences in the mobility of the polymer chains within DEF. A linear fit of zero-shear viscosities of PPF:DEF solutions makes it possible to predict the solution viscosity at a designated temperature when 3D printing by μSLA or DLP. In short, to decrease PPF viscosity to the suitable range for 3D printing, three main strategies available are: decreasing the molecular mass $\overline{M_n}$ of PPF, decreasing wt.% of PPF in PPF:DEF resin formulation, and/or increasing the temperature of the resin during the 3D printing process.

For cure tests and 3D printing of PPF:DEF resins at ambient temperature, a PPF:DEF weight ratio 1:1 was chosen for an initial study as this ratio yields an intermediate viscosity (0.21-0.94 Pa·s) and has been reported previously for 3D printing.[41] Cure tests were performed to study the relationship between exposure duration, the UV light intensity during that exposure, and the resulting layer thickness from the three PPF oligomer resins at ambient temperature (24 ± 2 °C) to determine the most appropriate layer thickness for the 3D printing of tensile bars. As shown in Figure 4.2, increasing the curing time from 45 s to 180 s led to a significant increase in the measured thickness of cured PPF:DEF films from about 0.1 mm to about 0.3 mm, indicating the lowest curing time necessary for curing of a layer of predetermined thickness. For example, the layer thickness choice of the 45 s per layer UV exposure time should be less than 0.1 mm to maintain effective binding between cured layers. As expected layer thickness can be controlled by adjusting the exposure time of each layer.[198] However, the high molecular mass distribution of PPF synthesized by the traditional step growth method, it has previously been difficult to

impossible to determine a relationship between molecular mass and layer thickness when all other resin additives are held constant.

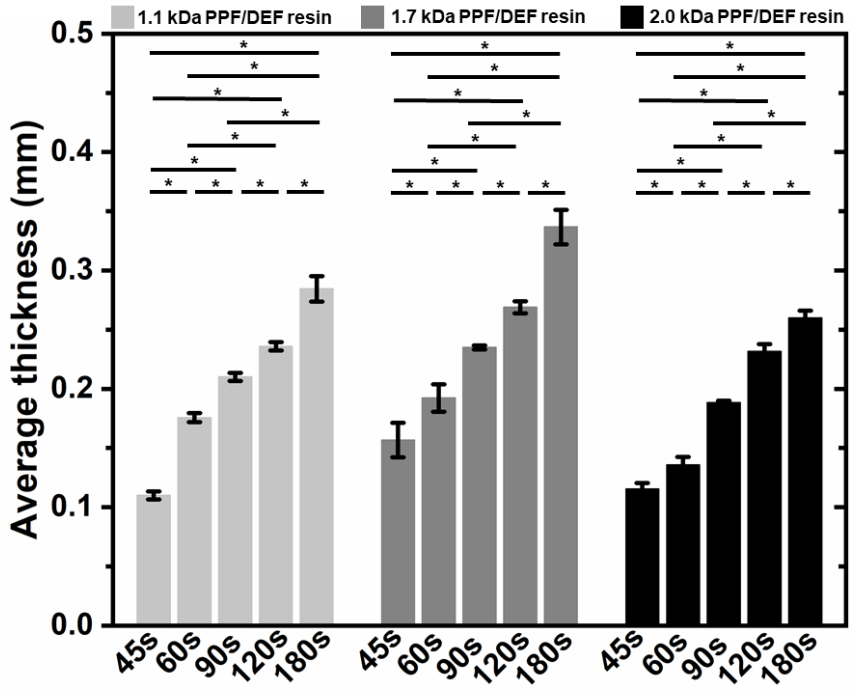

Figure 4.2. Film thickness of cured PPF:DEF resins as a function of cure time and number-average molecular mass ($\overline{M_n}$) of PPF oligomers, UV intensity at 225 mW/dm^2. *$p < 0.05$, one-way ANOVA test with Tukey method.

Given the photoinitiator concentrations used, the films obtained after a UV irradiation time below 90 s have a gel consistency, so for an efficient photo-crosslinking within and between the layers, we used a 120 s UV exposure time for each layer for 3D printing of tensile bars with a 50 μm/layer thickness. Figure 4.3A shows a schematic representation of the Computer Aided Design (CAD) model used for the tensile bars. From Figure 4.3B, the tensile bars at 40 % scale of ASTM D638 type V model have length overall (LO) close to the diameter of a United States quarter. After 3D printing of tensile bars in each of the three $\overline{M_n}$ groups, the dimensions of each tensile bar were measured with a digital caliper before tensile testing to compare the difference in dimension between the

final tensile bars and the CAD design. As shown in Figure 4.3C, the LO values (■) of the three groups are larger only by 0.8 %, 0.6 % and 0.2 % of the LO value of design.

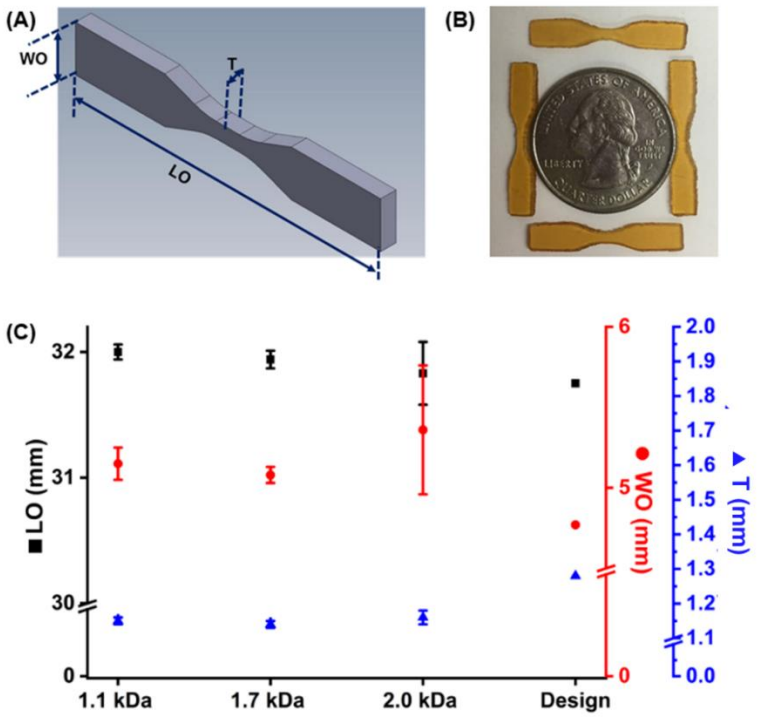

Figure 4.3. A) Dimensional parameters in CAD. B) 3D printed tensile bars, layer thickness 50 μm, 40 % scale of ASTM D638 type V. C) External dimension information of 3D printed tensile bars for tensile test, with 50 % scale of ASTM D638 type V in CAD. (LO, length overall; WO, width overall; and T, thickness).

A similar trend can be found for the width overall (WO) values (●), and LO (■) values, both of which show small variances for all three resins (*i.e.*, none are significantly different from Levene's test [squared deviations], indicating high accuracy of the 3D printing). Moreover, the minor existing errors between the CAD design and the materials obtained can be predicted and compensated. The thickness values (▲) of three resin groups are smaller than that in CAD design, which suggests that shrinkage occurred during 3D printing. This is expected because of the phase change of this material during photo-crosslinking and can be fixed by adjusting the printing parameters during printer set-up.[199,

[200] Overall, the 2.0 kDa PPF group showed the the least precise 3D printing. A possible reason for this decrease in printing stability is the higher $\overline{M_n}$, which facilitates more crosslinking also facilitates more variation in shrinkage. However, overall, none of the groups showed an unexpected level of fidelity to the CAD file given the expected amount of shrinkage.

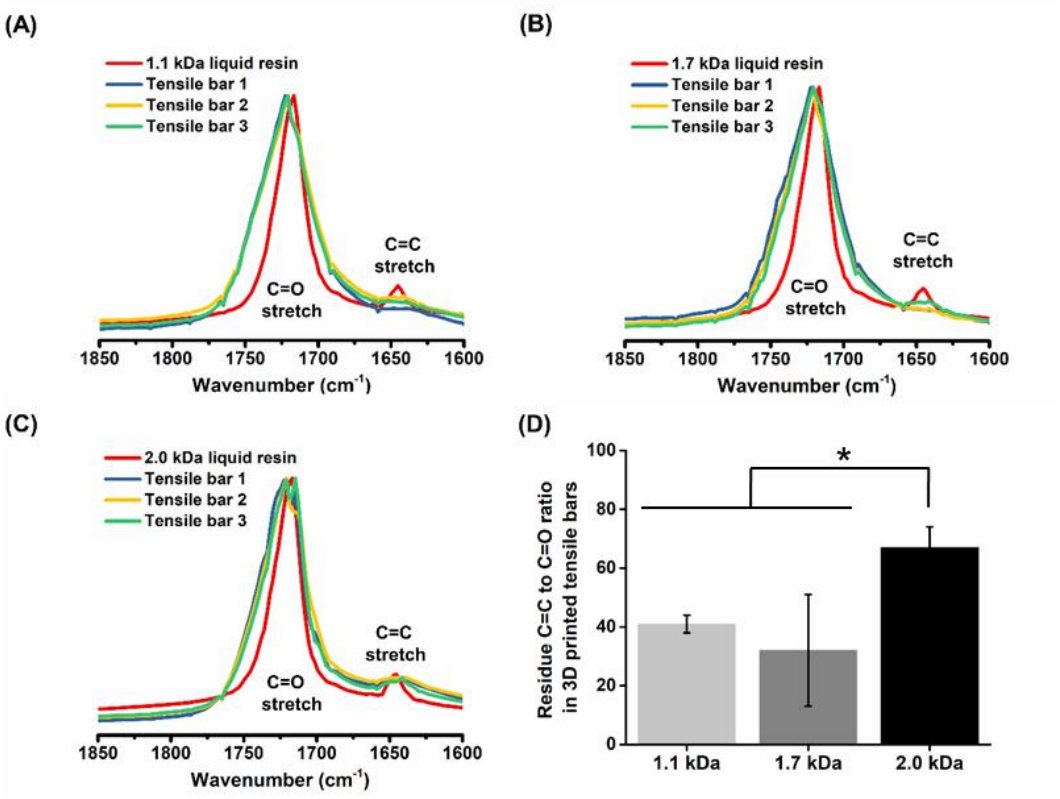

Figure 4.4. Normalized FTIR spectra showing the alkene C=C and carbonyl C=O stretches before and after 3D printing of PPF:DEF resins, using 1.1 kDa PPF (A), 1.7 kDa PPF (B), and 2.0 kDa PPF (C). Liquid resin denotes the resin before photo-crosslinking. (D) Calculated average residue of C=C to C=O groups in the 3D printed tensile bars. *$p < 0.05$, one-way ANOVA test with Tukey method.

To evaluate the double bond conversion after 3D printing, various tensile bars were characterized by Fourier Transform Infrared Spectroscopy (FTIR). Figure 4.4A, B and C shows the normalized IR stretches of ester carbonyl C=O bond (stretching at 1670-1770

cm^{-1}) and alkene C=C bond (stretching at 1625-1665 cm^{-1}) before and after 3D printing, part cleaning, and post-curing exposure (with 20 min post-printing full spectrum UV curing) by an OriginPro$^{TM\ 2017}$ software. Comparison of the red curve (before 3D printing) with blue, yellow and green curves (after UV exposure) in Figure 4.4A showed a significant decrease of the peak intensity of C=C stretching, revealing a decrease in number of C=C in this PPF:DEF mixture. The C=O stretching pattern became wider after photo-crosslinking, which corresponded to crosslinking throughout the resin at the unsaturated sites. Similar trends have been observed in the 1.7 kDa group and 2.0 kDa group as shown in Figure 4.4B and C. This demonstrated that the PPF oligomer chains and DEF solvent, acting as a co-crosslinker and as crosslinkable monomer (*i.e.,* a precursor of PPF), underwent photo-crosslinking during the 3D printing process. The ratio of area under the peak for C=C to C=O in Figure 4.4A, B and C were calculated and listed in Figure 4.4D. The 2.0 kDa group had the most C=C residue after 3D printing, while the 1.1 kDa group and 1.7 kDa group had relatively similar C=C residue. This semi-quantitative result from FTIR analyses demonstrated a lower photo-crosslinking for the higher $\overline{M_n}$that correlates with poor printing repeatability in terms of dimensions.

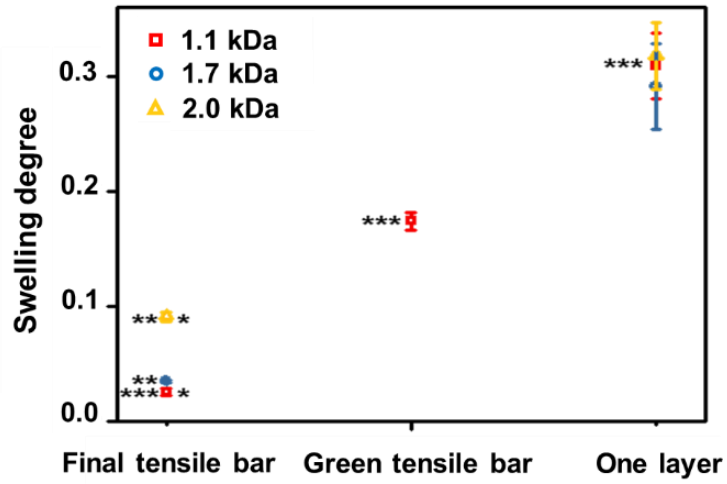

Figure 4.5. Swelling degree results of 3D printed tensile bars and one layer cured resin as a function of number-average molecular mass ($\overline{M_n}$) of PPF oligomers. Green tensile bar corresponds to swelling tests performed directly after 3D printing, final tensile bar corresponds to swelling tests performed after post-curing 20 min, and one layer means the swelling test was performed after 120 s UV curing process in the 3D printer. *p < 0.01, **p < 0.01, ***p < 0.01, one-way ANOVA test with Tukey method.

The properties of 3D printed tensile bars were then studied in terms of swelling behavior and tensile tests. The degree of swelling of one layer, green tensile bars ("green" means test was performed directly after 3D printing, without post-curing) and final tensile bars ("final" means test was performed after the completion of 20 min full spectrum UV post-curing) are listed in Figure 4.5.

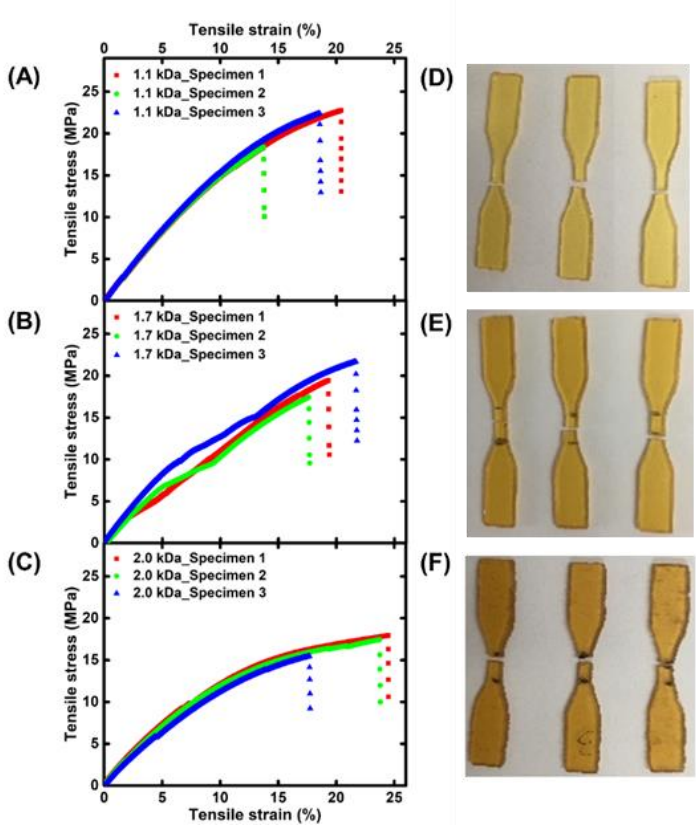

Figure 4.6. (A, B and C) Engineering stress-strain curves of 3D printed PPF:DEF tensile bars as a function of number-average molecular mass ($\overline{M_n}$) of PPF oligomers from tensile testing with a strain rate = 0.1 mm/(mm·min). (D, E and F) Pictures of tensile bars after break from tensile test as a function of number-average molecular mass ($\overline{M_n}$) of PPF oligomers, 1.1 kDa PPF, 1.7 kDa PPF and 2.0 kDa PPF, respectively.

For the 1.1 kDa PPF resin group, the data show that as the total UV exposure time increased, from green tensile bar to final, post-cured, tensile bar, the extent of swelling decreased. Thus, the final tensile bar groups had less swelling, for all the three $\overline{M_n}$ studied. The longer UV exposure time led to an increased degree of crosslinking and a tighter network in the tensile bar preventing solvent uptake. The post-cured tensile bars each swelled less than 10 %, however, the 2.0 kDa final tensile bars had a significant larger swelling ratio (0.091±0.004) than the 1.1 kDa and 1.7 kDa final tensile bars, driven by a lower crosslink density, as demonstrated above. Moreover, because the one-layer part had

a higher surface area to volume ratio than the two types of tensile bars, this has allowed it to swell more readily. Consequently, the degree of swelling of 3D printed PPF-based biomaterials can be attributed to both part thickness, UV exposure time and network structure.

Mechanical properties of the various PEF:DEF tensile bars were assessed by tensile mechanical testing. The engineering tensile stress-strain curves of three resin groups are shown in Figure 4.6. All specimens had ultimate strength above 15 MPa and strain in the 15%-25% range. No significant yield behavior was observed in each specimen.

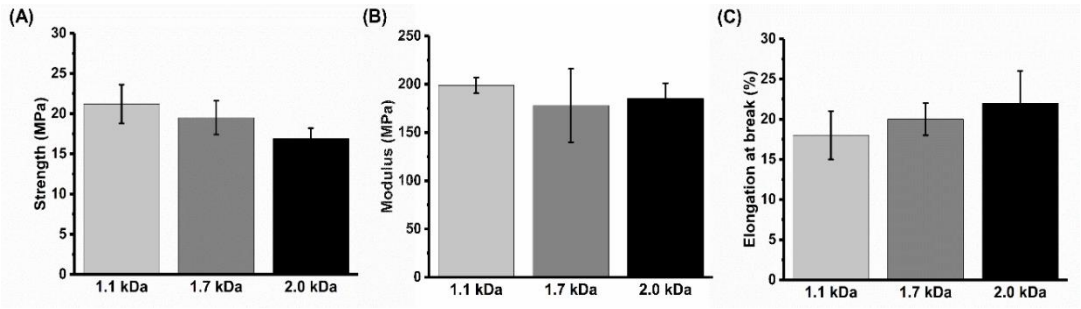

Figure 4.7. Mechanical properties from tensile tests of 3D printed PPF:DEF materials as a function of number-average molecular mass ($\overline{M_n}$) of PPF oligomers. (A) tensile strength (stress at failure carried by the specimen during tensile tests), (B) elastic modulus from slope of linear fitting of the engineering stress-strain data in strain range from 0 % to 0.1 % and (C) elongation at break of tensile bars.

The strength, elastic moduli, and elongations at break are shown in Figure 4.7A, B and C respectively. Even if a trend seemed to show a decrease of strength and an increase of elongation break as $\overline{M_n}$ increased, statistical analysis from one-way ANOVA test with Tukey method, at p<0.05 level, showed the means of tensile mechanical properties (strength, and elongation at break) of 3 resin groups are not significantly different. Moreover, from Figure 4.7B, the average elastic modulus in 1.1 kDa, 1.7 kDa and 2.0 kDa groups were 199 ± 8 MPa, 178 ± 38 MPa and 185 ± 16 MPa, respectively.

This indicates that under the same printing conditions, $\overline{M_n}$ of PPF oligomers in the range of 1.1 kDa to 2 kDa did not significantly influence tensile mechanical properties of tensile bars printed from a DLP 3D printer. In addition, mechanical properties of our materials are close to those human trabecular bone (*i.e.*, strength ranged between 2 and 45 MPa)[120, 201-203] which suggests that they have a good ability to promote the formation of osteoblasts. Indeed, numerous studies have reported that mechanical properties are among the parameters influencing cell proliferation, migration, and differentiation.[204, 205] Typically, a functional material should mimic the mechanical properties of the target tissue. Moreover, because previous studies demonstrated that PPF shows various degradation rates depending on its molecular mass,[35] our results highlight a real advantage: the retention of mechanical properties adapted to trabecular bone reconstruction while tuning biodegradability *via* molecular mass modification.

4.5 Conclusions

In summary, we studied several parameters influencing the cDLP 3D printing of low molecular mass distribution ($Đ_m$<1.6) poly(propylene fumarate) (PPF) oligomers and the tensile properties of the materials obtained. For three PPF with number-average molecular mass ($\overline{M_n}$) ranged from 1.1 kDa to 2.0 kDa, the complex viscosity of PPF based resin was found following an Arrhenius model, and this benchmark model makes it possible to precisely and proficiently predict the resin viscosity at a designated temperature (between 25-55 °C) using Arrhenius equation. Complex viscosity increased significantly with increase in either PPF molecular mass or the amount of PPF with respect to solvent.

Resin viscosity can be maintained in the 3D printable range by decreasing $\overline{M_n}$ of PPF, and/or increasing temperature and/or increasing loading of diethyl fumarate (DEF) used both as solvent and co-crosslinker. These observations confirm the importance of low viscosity, both to promote flow during 3D printing (*i.e.*, between printing of each layer), but also to ensure full mixing of resin additives (*i.e.*, photoinitiators, radical scavenger, and co-crosslinking species). 3D printed tensile bars with three $\overline{M_n}$ of PPF oligomers demonstrated good printing accuracy, despite expected shrinkage, as no significant difference was found dimensionally. Moreover, the chain length did not significantly influence the tensile properties of the final 3D printed tensile bars in the $\overline{M_n}$ range studied, and tensile properties of these 3D printed tensile bars showed that elastic moduli (from 178±38 MPa to 199±8 MPa) of these specimens were within range of human trabecular bone. These results further confirm how PPF constitutes a polymer of interest for designing scaffolds for bone regeneration by DLP 3D printing since providing suitable mechanical properties in a $\overline{M_n}$ range leading to various degradation rates. *In vivo* degradation and tissue regeneration studies of PPF oligomers synthesized from ROCOP method are ongoing to evaluate the translational potential of this material.

4.6 Acknowledgements

The Ohio Department of Development's Open Innovation Platform "Akron Functional Materials Center" and 21st Century Medical Technologies are acknowledged for financial support. M.L.B is grateful for support from the W. Gerald Austen Endowed Chair in Polymer Science and Polymer Engineering from the John S. and James L. Knight

Foundation. D.D. acknowledges partial support from the Army, Navy, NIH, Air Force, VA, and Health Affairs to support the AFIRM II effort under award No. W81XWH-14–2-0004. The US Army Medical Research Acquisition Activity is the awarding and administering acquisition office for award No. W81XWH-14–2-0004. Opinions, interpretations, conclusions, and recommendations are those of the authors and are not necessarily endorsed by the US Department of Defense.

CHAPTER V

STAR-SHAPED POLY(PROPYLENE FUMARATE), TOWARD A DRASTIC VISCOSITY DECREASE OF PRINTABLE RESIN AND FAST 3D PRINTING OF SHAPE-MEMORY GYROID SCAFFOLDS

Some of this work has been previously published as

Gaëlle Le Fer, Yuanyuan Luo and Matthew L. Becker

Polymer Chemistry, 2019, doi: 10.1039/C9PY00738E

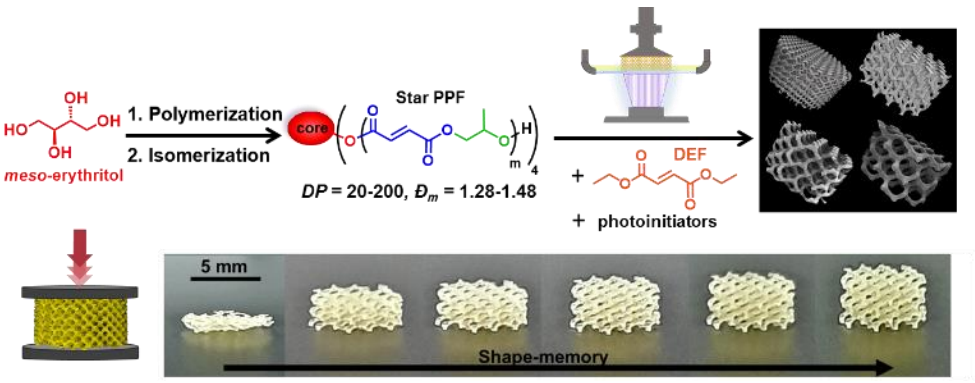

5.1 Abstract

Nowadays, additive manufacturing is changing tissue engineering by offering pathways to otherwise unattainable highly complex scaffold morphologies. Linear oligomer poly(propylene fumarate) (PPF) has already shown remarkable properties for 3D printing of porous gyroid scaffolds using continuous digital light processing (cDLP). Nevertheless, the narrow molar mass ($\overline{M_n}$) range with suitable viscosity properties for printing severely limits the printing speed, the breadth of mechanical properties, and the resorption window of the scaffolds. To overcome this constraint, we report the divergent synthesis of four-arm PPF using sugar-based alcohol *meso*-erythritol as initiator. Using a combination of ^{1}H NMR spectroscopy, size exclusion chromatography (SEC), and viscosity measurements, the well-defined star-shape was confirmed. Subsequently, printable resins based on star PPF were prepared and showed complex viscosity decreasing as the total $\overline{M_n}$ increases, allowing rapid printing of PPF with $\overline{M_n}$ nearly eight times larger than the largest PPF oligomer previously printed. High porosity gyroid scaffolds were manufactured with two different star-PPF molar masses and one linear oligomer of 1.6 kDa for comparison, and four architecture styles opening previously unexplored shape memory properties of PPF-based scaffolds.

5.2 Introduction

Progress in additive manufacturing, also known as three-dimensional (3D) printing, has the potential to revolutionize the way surgeons address complicated reconstructive efforts in many surgical specialties. Digital light processing (DLP), also referred to

dynamic mask photolithography, is a 3D printing technique based on the selective crosslinking of a photo-sensitive resin in a layer-by-layer process using a UV and/or visible light projector. This method affords high resolution control over cell scaffold features such as porosity, strut size and pore size and overall scaffold shape, offering significant advantages to regenerative medicine, including reproducibility or fabrication of patient specific templates.[170, 206] The architecture of the scaffold is of paramount importance since will directly impact its mechanical strength, degradation characteristics, and capacity to guide new tissues into the defect.

Tissue engineering, especially for the treatment of large bone defects could really be improved by the development of new resorbable 3D printed materials able to supply attractive alternatives to the autografts, allografts, ceramics, and metals that are currently used in clinical settings. Polymers are attractive materials for tissue engineering scaffolds because they may be chosen and tailored to satisfy specific requirements such as biodegradability, biocompatibility, functionality or mechanical properties.[26, 207, 208] Polyester has been extensively used in regenerative medicine partly because they exhibit various biodegradability rate.[209-211] Consequently, their use in tissue engineering has grown steadily over the past decade.[118, 212, 213] Saturated polyesters such as poly(ε-caprolactone) (PCL), poly(lactic acid) (PLA), poly(glycolic acid) (PGA), poly(lactic-*co*-glycolic acid) (PLGA) or vinyl polyester[214, 215] have been utilized in applications including suture,[216, 217] drug delivery systems,[218-221] imaging systems combining biomaterials and contrast agents,[222-224] and scaffolds for tissue engineering.[225, 226] Nevertheless, the lack of reactive groups along the backbone limits their post-polymerization and post-printing functionalization and their applicability for stereolithography (SLA).

Poly(propylene fumarate) (PPF), an unsaturated polyester, used in a number of medical applications, such as controlled drug release,[180, 181] and tissue engineering [83, 85, 87, 88, 96, 113, 183-186] has already shown remarkable properties in the fabrication of medical devices and 3D tissue scaffolds using SLA methods, such as cDLP.[20, 41, 107, 179, 227] The chains can be photo-crosslinked through the alkenes to produce reliable, high-fidelity solid-cured polymer scaffolds with complex geometric designs.[35, 228] PPF presents numerous benefits including its resorption timescale, within a window identified to more closely match new tissue growth than PLA or PCL. PPF degrades *via* hydrolysis of the ester bonds into a Krebs-cycle constituent (fumaric acid) and propylene glycol, two non-toxic products that are cleared by normal metabolic processes.[147, 177, 229] PPF was synthesized for the first time in 1994 by Mikos and co-workers[178] *via* step-growth polycondensation of diethyl fumarate (DEF) and propylene glycol. However, this synthetic method is difficult to control at low molar mass ($\overline{M_n}$), and results in broad molar mass distribution ($Đ_m$), poor end-group fidelity, all of which influence the properties of the final material. The ring-opening copolymerization (ROCOP) of maleic anhydride (MA) and propylene oxide (PO) in the presence of a cobalt catalyst was then introduced by Coates and co-workers[90] to yield well-defined poly(propylene maleate) (PPM) that could be converted to PPF upon isomerization. More recently, our group avoided the toxicity of cobalt by using magnesium ethoxide catalyst[41] and then developed PPF with high end-group fidelity thanks to magnesium 2,6-di-tert-butyl phenoxide ($Mg(BHT)_2(THF)_2$) catalyst and functionalized primary alcohol initiator.[36] This result provided a route to expand the diversity of PPF-based copolymers such as poly(lactone)-*block*-polypropylene fumarate)[230] or

poly(ethylene glycol)-*block*-poly(propylene fumarate) (PEG-*b*-PPM)[182] *via* sequential ROP/ROCOP method and PEG macroinitiator, respectively.

However, opposing forces govern the polymer resin properties required for cDLP 3D printing and ensuring the resulting scaffolds possess the optimal biological and mechanical properties. Low viscosities, typically between 0.25 Pa·s and 10 Pa·s[231-233] are required for rapid printing to accommodate a new layer of liquid resin to flow into the small gap between the bottom surface of the resin tray and the previous cured solid layer supported by the platform and to maintain dispersion of resin additives.[167, 175, 188, 189] The viscosity of pure linear PPF (*e.g.*,for a $\overline{M_n}$ = 1.5 kDa, $Đ_m$ = 1.7 PPF oligomer, the zero-shear viscosity at 40 °C is 2370 Pa·s)[137] has required a fifty wt.% dilution in the light reactive diluent diethyl fumarate (DEF) to avoid print failures and long curing time and allow layer thickness control.[145, 158] Because the viscosity of linear PPF is closely related to its degree of polymerization,[96, 234] the use of short PPF oligomers in a 0.7-3.5 kDa molar mass range is usually required, which limits the exploration of mechanical properties of the materials obtained.

Branched polymers such as star polymers, cyclic polymer, dendrimers, and hyperbranched polymers process distinctive rheological and mechanical properties. In comparison with conventional linear polymers, they generally provide smaller hydrodynamic volume and consequently lower solution viscosity and less entanglement in bulk.[235] For these reasons, we synthesized four-arm poly(propylene fumarate) through a core-first approach using *meso*-erythritol, a sugar-based alcohol, as an initiator with total DPs in a 20-200 range corresponding to molar masses between 3.2 and 31.2 kDa and narrow, monomodal molar mass distributions ($Đ_m$ = 1.28-1.48). These star-shape PPF were

used to prepare PPF:DEF resins with different weight ratios (50:50 wt%, 60:40 wt% and 70:30 wt%) to assess the influence of the $\overline{M_n}$ of PPF on solution viscosity properties. Furthermore, we sought to determine the structure-property relationship between the resin formulation, the gyroid scaffold pore architecture and characteristics such as mechanical integrity by printing materials with constant porosity and four different struts sizes. Finally, we found that gyroid scaffolds printed with four-arm PPF with a DP of 200 exhibited tunable shape-memory properties.

5.3 Experimental Section

5.3.1 Materials and methods

5.3.1.1 Chemicals

All reagents were purchased from Sigma-Aldrich (St. Louis, MO, USA). All solvents were purchased from Fisher Scientific (Hampton, NH, USA) and dried using an Innovative Technology Inc. (Newburyport, MA, USA) Pure Solv MD-3 solvent purification system. $Mg(BHT)_2(THF)_2$ was synthesized as reported previously.[236] *Meso*-erythritol was dried by azeotropic distillation before use. Maleic anhydride was dried under vacuum over P_2O_5 for one week. Propylene oxide was dried over calcium hydride overnight prior to vacuum distillation. All other reagents were used as received.

5.3.1.2 Characterization techniques

Proton (^{1}H) NMR experiments were performed in DMSO-d_6 or $CDCl_3$ at 25 °C using a Varian (Palo Alto, CA, USA) Mercury NMRS 500 spectrometer. All chemical shifts were recorded in parts per million (ppm) relative to the reference peak solvent: DMSO at δ = 2.50 ppm and chloroform at δ = 7.26 ppm. The relative number-average molar masses ($\overline{M_n}$) and the molar mass ditributions ($Đ_m$) of copolymers were determined by size exclusion chromatography (SEC) on a Tosoh (Grove City, OH, USA) EcoSEC HLC-8320GPC with TSKgel GMHHR-M columns in series. The detector used in this determination was a refractive index detector (RI). Tetrahydrofuran (THF) was used as eluent flowing at 1.0 mL·min^{-1}. The sample concentration was 10 mg·mL^{-1}. Relative $\overline{M_n}$ were calculated using a calibration curve determined from NIST-traceable polystyrene standards.

To confirm the arm number of star PPM, the intrinsic viscosities of star-shaped PPM with a degree of polymerization (DP) of 40 were measured in THF using an Ubbelohde viscometer at 35 °C. Each sample solution was prepared in THF and then diluted directly by adding a known volume in the viscometer. The flow time was recorded at each concentration (n=3). The ratios (g′) of intrinsic viscosities of the star-shaped PPF to that of linear PPF bearing similar number-average molar mass were experimentally estimated in accordance with Equation 5.1:

$$g' = [\eta]_{star}/[\eta]_{linear} \qquad \text{Equation 5.1}$$

where $[\eta]_{star}$ and $[\eta]_{linear}$ are the intrinsic viscosities of star PPF and linear PPF respectively. For a star-shaped polymer with perfect arm structures, there is a strong relationship of $g^{1/2}$

= g′ or $g^{1/2}/g' = 1.0$ as proposed by Zimm and Kilb.[237] The parameter (g) was defined as the ratio of mean-square radius of gyration (R_g) of a star-shaped polymer to that of a linear counterpart with similar $\overline{M_n}$, and could be calculated according to Equation 5.2,[238] where the parameter *f* is the number of arms of the star-shaped polymer.

$$g = 6f / [(f+1)\cdot(f+2)] \qquad \text{Equation 5.2}$$

Complex viscosity (η*) of PPF:DEF resins was obtained by using an ARES-G2 rheometer from TA instrument (New Castle, DE, USA) using 50 mm diameter parallel plates with a geometry gap of 0.4 mm. Measurements were performed at 25 °C, at 8 % strain and at frequencies ranging from 0.1 Hz to 100 Hz (0.6 to 628.3 $rad\cdot s^{-1}$). Oscillatory shear measurements were done in the linear response regime.

The scaffolds were imaged using an Olympus Stereoscope (Center Valley, PA, USA) to depict the gyroid architecture features in greater detail. The structure properties of these gyroid scaffolds were also thoroughly characterized nondestructively using X-ray micro-computed tomography (μ-CT) Skyscan 1172 (Bruker; Billerica, MA, USA). 3D scanning of scaffolds was carried out using the following parameters: 40 kV voltage, medium camera (pixel size = 8.73 μm), no filter, 238 ms camera exposure preset time and 7.0 μm resolution.

The mechanical properties of the gyroid scaffolds were studied by compression tests using an Instron 5566 Universal Testing Machine (Norwood, MA, USA). Force and displacement were zeroed prior to compression, with the top plate slightly above the surface of the sample. Samples were compressed at a constant crosshead velocity of 0.5 $mm\cdot min^{-1}$ at room temperature while stress and strain were monitored throughout the experiment. The compressive moduli were calculated using the slope of linear fitting in the

linear regime. The reported results are average values from five individual measurements and the associated errors are the standard deviations.

The recovery of the scaffolds after compression was evaluated by measuring their thickness over time with a digital caliper at room temperature and at 40 °C. The actual height/initial height ratio *versus* recovery time was then plotted. Each point is a duplicate and the associated errors are the standard deviations.

5.3.2 Procedures

5.3.2.1 Synthesis of star-shaped poly(propylene maleate) (PPM)

Four-arm star-shaped poly(propylene maleate) (PPM) copolymers were synthesized by ring-opening copolymerization (ROCOP) of maleic anhydride (MAn) and propylene oxide (PO) using *meso*-erythritol as an initiator. Various [monomers]/[initiator] molar ratios were used to obtain copolymers with different PPM arm lengths and consequently various total degrees of polymerization (DPs). For instance, four-arm star PPM with a target total degree of polymerization (DP) 40, was prepared as follows: in a glovebox, *meso*-erythritol (112.12 $g \cdot mol^{-1}$, 124.5 mg, 1.02 mmol), $Mg(BHT)_2(THF)_2$ (604.95 $g \cdot mol^{-1}$, 123.4 mg, 2.04×10^{-1} mmol), anhydrous toluene (10.2 mL), MAn (98.06 $g \cdot mol^{-1}$, 4.0 g, 40.8 mmol) and PO (58.08 $g \cdot mol^{-1}$, 2.85 mL, 40.8 mmol) were introduced, in this order, in a flame-dried Schlenk tube. The Schlenk tube was sealed with PTFE plug and removed from the glovebox. The solution was stirred at 80 °C for 48 h (typically until the PPM precipitated in the bottom of the Schlenk and the supernatant looked clear). The resultant copolymer was recovered by precipitation in diethyl ether and then dried under

vacuum to afford a highly viscous oil. Yield: 78 %. Influence of the total monomer concentration (1 M, 2 M, 4 M, 8 M and 14 M) on the monomer conversion was investigated by performing syntheses of star PPM with *meso*-erythritol as an initiator and total target DPs of 20, 40, 80, 120 and 200. Moreover, influence of the total monomer concentration on the copolymerization process was investigated by performing kinetic studies at 2 M, 4 M and 8 M, with *meso*-erythritol as an initiator and total target DP at 40. The initial mixture was split in several vials, immersed in a preheated bath at 80 °C (corresponding to the time zero of the reaction), copolymerizations were conducted under stirring and stopped by quenching to ambient temperature and adding an excess of chloroform. The monomer conversions were determined by ^{1}H NMR in $CDCl_3$ of crude samples from reactional volumes. For comparison, kinetics of linear PPM was performed using propargyl alcohol as a monofunctional initiator with a monomer concentration of 8 M and target total DPs at 10 and 40.

5.3.2.2 Isomerization of PPM.

The copolymer was dissolved in chloroform at a concentration of 0.5 mol·L^{-1} of MAn residues and diethylamine (DEA) was added to reach 0.15 eq/MAn residue. As an example, four-arm star PPM with target total DP at 40 were isomerized in the corresponding four-arm star PPF as follows: star-shaped PPM (4.8 g, 7.62×10^{-1} mmol, 30.5 mmol of olefin) was dissolved into chloroform (61 mL, 0.5 mol·L^{-1} of olefin), DEA (0.47 mL, 0.15 mol. eq. olefin) was added and the solution was heated under reflux for 24 h under a nitrogen atmosphere. After cooling to room temperature, the organic solution

was washed with 1 M sodium phosphate solution (250 mL, pH = 6) and the copolymer was recovered after evaporation of the chloroform. Yield: 95 %.

5.3.2.3 Resin preparation.

Polymeric resins were prepared by mixing star-shaped PPF with diethyl fumarate (DEF), which acts as both solvent and crosslinking agent. Various PPF:DEF weigh ratios were investigated, *i.e.*, 70:30, 60:40 and 50:50 wt%. PPF and DEF were carefully introduced in the flask and mixtures were maintained at 45 °C overnight under stirring to insure adequate mixing. In order to print 3D scaffolds, two photoinitiators, phenylbis(2,4,6-trimethylbenzoyl)phosphine oxide (BAPO) and Irgacure 784, and a radical scavenger oxybenzone (HMB) were added to the PPF:DEF solutions at 3 %, 0.4 % and 0.7 % by weight, respectively and mixed evenly throughout the resin, following a previously reported protocol.[41, 96]

5.3.2.4 Gyroid scaffold design.

Each scaffold was cylindrical with a prescribed diameter of 6 mm and height of 4 mm. Schoen's gyroid triply periodic minimal surface[36, 239] was used as the geometric foundation for the pore architecture allowing full control over the porosity and strut sizes. In this work, four different architectures were investigated with constant pore geometry and porosity (88.2 %) but varying the strut size from 140 to 280 μm and consequently the pore size from 489 to 979 μm. The gyroid parameters and the dimensions are given in Table 5.1.

Table 5.1. Pore design parameters of gyroid scaffolds.

Architecture	Porosity (%)	Strut size (μm)	Pore size (μm)
CAD model 1	88.2	140	489
CAD model 2	88.2	200	699
CAD model 3	88.2	240	838
CAD model 4	88.2	280	978

Although cylindrical structures were used in this work, additive manufacture, especially digital light processing (DLP), allows this same design methodology to be applied to arbitrarily shaped objects. Thus, anatomically matched implants designed directly from patient computed tomography-data can be fabricated.

5.3.2.5 3D printing of gyroid scaffolds.

Gyroid scaffolds were printed from liquid resins with an EnvisionTEC (Dearborn, MI, USA) Micro HR 279 printer using a 405 nm LED UV light projector with an irradiance of 225 $mW \cdot dm^{-2}$ and the CAD models were sliced digitally into layers using the Perfactory software suite prior to manufacturing. The Perfactory P3 is an inverted system that projects upward through a transparent glass plate into a reservoir containing the resin. After each projection, the build platform moves vertically upward to allow resin inflow for the next layer. Prior to scaffold printing, cure tests of PPF-based resins were performed to determine the optimal printed layer thickness and UV exposure time depending on the resin formulation. About 20 mg of resin were placed in the middle of the resin tray and after irradiation with UV for varying time durations (*i.e.*, 60, 120, 180 and 240 s), the uncured liquid resin was gently removed by tissue paper. The resulting film was peeled off the resin

tray with a razor blade and the thickness of the cured film was measured by a digital caliper (Marathon, Ontario, CA) with 10 μm precision. Following these cure tests and printing tests, the layer thickness was fixed to 25 μm and projection time ranged from 60 s to 225 s depending on the PPF molar mass. After printing, scaffolds were immediately rinsed with acetone, 70 % ethanol (v/v), and distilled water for 15 s each. Finally, the "green" scaffolds were post-cured in a full spectrum UV irradiation chamber for 45 min or 90 min. The scaffold diameters and heights were measured with a digital caliper to quantify the shrinkage.

5.4 Results and discussion

The synthesis of four-arm star polypropylene maleate (PPM) was performed through a core-first approach using *meso*-erythritol as multifunctional initiator possessing four hydroxyl initiating functionalities and $Mg(BHT)_2(THF)_2$ as catalyst for the ring-opening copolymerization (ROCOP) of maleic anhydride (MAn) with propylene oxide (PO) (as represented in Scheme 5.1). Various total monomer concentrations were investigated for their influence on the copolymerization and with the aim of obtaining defined star-shaped copolymer with low viscosity adapted for 3D printing application.

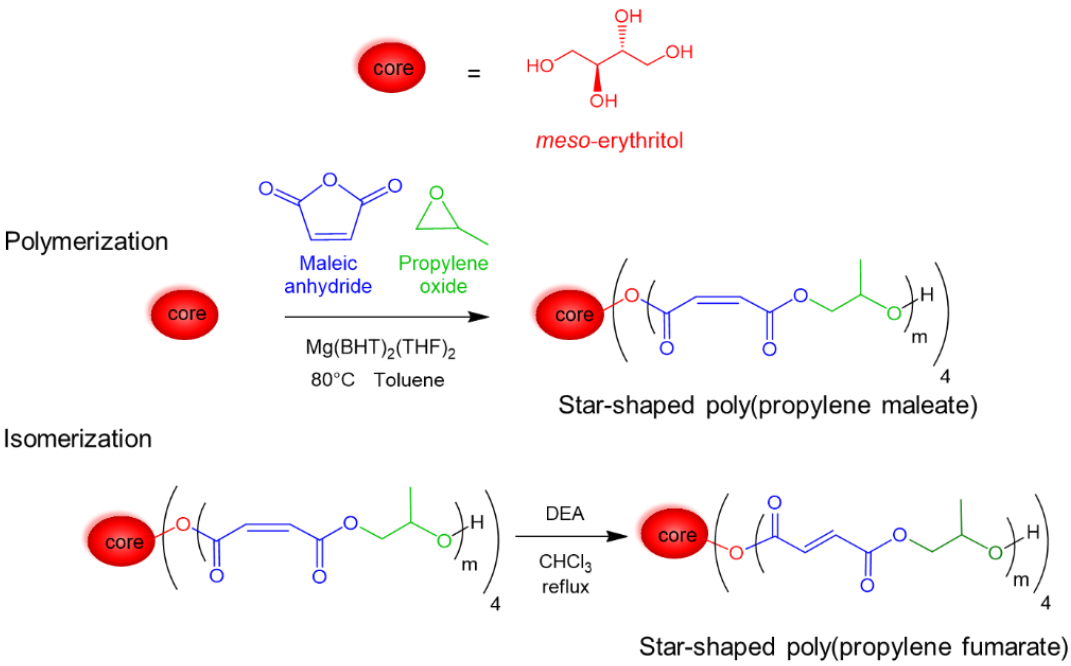

Scheme 5.1. Synthesis of star-shaped poly(propylene maleate) (PPM) polymers and subsequent isomerization into star-shaped poly(propylene fumarate) (PPF).

Initial copolymerization conditions employed a 1:1 molar ratio of MAn:PO, total monomer concentrations of 1, 2, 4, 8 and 14 M, and amounts of *meso*-erythritol targeting degrees of polymerization (DPs) of 5, 10, 20, 30 and 50 units for each arm corresponding to total target DPs 20, 40, 80, 120 and 200 respectively. The chemical structures of *meso*-erythritol used as initiator (Figure 5.1A) and of poly(propylene maleate) (PPM) copolymers obtained were investigated by ^{1}H NMR spectroscopic analyses (Figure 5.1B). The star structure of copolymers was attested by the downfield shift of the signals 1, and 2' from the initiator (from 3.35 to 5.44 ppm and from 3.35 and 3.50 ppm to about 4.50 ppm respectively). The ratio of MAn and PO incorporated into the polymer backbone remained roughly equimolar, moreover, the absence of signal corresponding to the methylene protons observed from the homopolymerization of PO (δ = 3.3-3.5 ppm) confirmed the alternating copolymerization process. The DP values and the corresponding molar masses

were calculated using ratio of the proton integration from the core 1 and integration of 2 ^{1}H and the signal integration of 3 attributed to the olefin protons of MAn repetitive units.

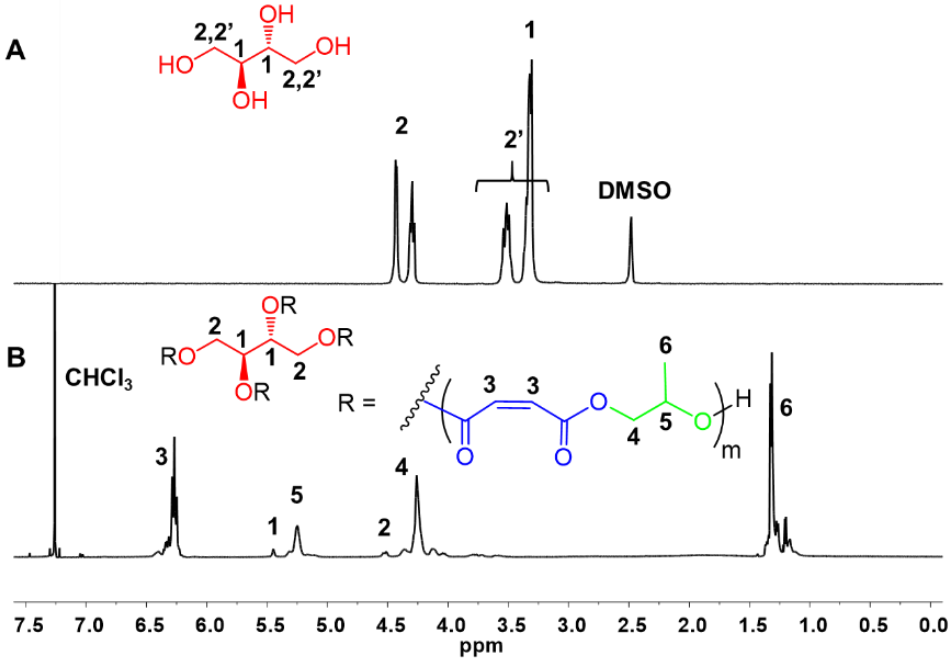

Figure 5.1. (A) ^{1}H NMR spectrum of *meso*-erythritol (500 MHz, 303 K, DMSO-d_6) and (B) ^{1}H NMR spectrum of four-arm star-shaped PPM DP 40 with a *meso*-erythritol core (500 MHz, 303 K, $CDCl_3$).

The obtained DPs were plotted *versus* the monomer concentration for each of the target DP (Figure 5.2A). The resulting plot revealed a strong concentration dependence of the DP obtained. Higher target DP generally required higher monomer concentration. As an example, while the total target DP of 20 was reached from a 2 M concentration, a 14 M concentration was necessary to obtain full monomer conversation leading to a total DP of 200 (4×50).

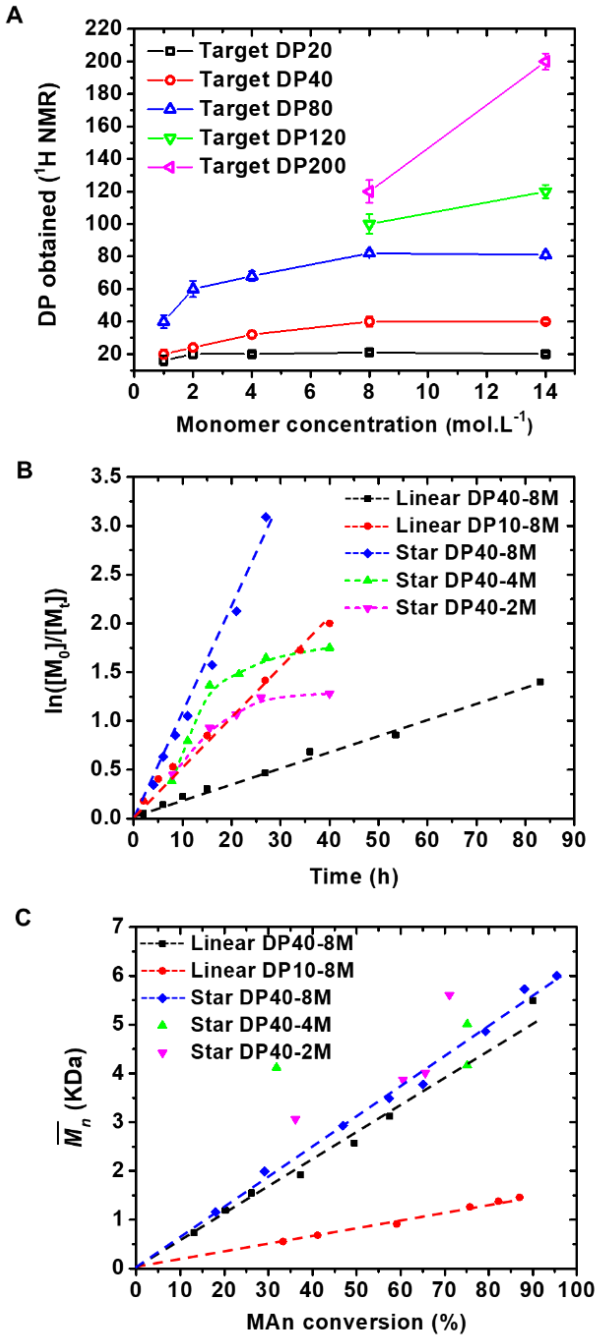

Figure 5.2. (A) Evolution of total DP of four-arm shaped PPM as a function of monomer concentration. (B) Kinetic plot for the copolymerization of maleic anhydride and propylene oxide for star-shaped PPM target DP40 (total monomer concentration 2 M, 4 M and 8 M), and linear PPM target DPs 10 and 40 (total initial monomer concentration = 8 M), conducted at 80 °C in toluene with $[OH]_0$:$[Cat.]_0$ = 1:0.05. (C) Changes in number-average molar mass ($\overline{M_n}$) over increasing MAn conversion determined by ^{1}H NMR (500 MHz, 303 K, $CDCl_3$).

For a better understanding of the influence of the concentration during the copolymerization process, kinetic studies were performed at various concentrations (2 M, 4 M, 8 M) at target DP 40 using *meso*-erythritol as an initiator. For comparison, kinetic studies at 8 M were also conducted during the synthesis of linear PPM oligomers DP10 and DP40, corresponding to the DP of one arm or the total DP within the star structure. For this purpose, the $\ln([M_0]/[M_t])$ values and the MAn conversion were monitored *via* ^{1}H NMR of the crude reaction mixture by comparing the monomer proton resonance (δ = 7.01 ppm) to the corresponding polymer proton resonance (δ = 6.27 ppm). The monomer conversion of PO was not characterized because of the low vapor pressure and boiling point of the PO leading to unreliable integrations assessed by ^{1}H NMR spectroscopy. Figure 5.2B and Figure 5.2C show respectively the evolution of the $\ln([M_0]/[M_t])$ values with time and the evolution of number-average molar mass ($\overline{M_n}$) with the MAn conversion. For the star PPM synthesis, at 8 M (blue diamonds), the kinetic plot of $\ln([M]_0/[M]_t)$ against time revealed a linear relationship, which demonstrated a pseudo-first-order kinetics and thus suggested a living polymerization mechanism with a maintained number of active chains overtime and no termination side reactions. However, for copolymerizations performed at 2 M and 4 M (pink and green triangles respectively), the slowdown of the polymerization rate followed by a plateau, characteristic of an early termination of the polymerization, was observed, demonstrating a loss of the living characteristics. The ROCOP of MAn with PO at 8 M to afford linear PPM followed pseudo-first-order-kinetics[240], as well for DP10 (red circles) and DP40 (black squares). From the slopes of these linear kinetic plots, the propagation rate constants k_p' for the star PPM, and the linear PPM DP40 and DP10 respectively were calculated and found to be 2.30×10^{-2} L·mol^{-1}·s^{-1},

3.84×10^{-3} L·mol^{-1}·s^{-1} and 2.88×10^{-3} L·mol^{-1}·s^{-1}. The synthesis of the star shape PPM DP40 is therefore eight times faster than the linear PPM DP40 and six times faster than the linear DP10. The $\overline{M_n}$ value obtained by ^{1}H NMR was plotted against MAn conversion. The plot obtained showed that $\overline{M_n}$ increased linearly with conversion and no transfer reactions occurred during the copolymerization except at 2 M and 4 M.

Table 5.2. Synthetic conditions and characterization of star-shaped poly(propylene maleate) (PPM).

Target DP	[MAn]:[I]:[Cat][a]	[Monomer] (M)	MAn conversion[b]	DP NMR[b]	$\overline{M_n}$ NMR[b] (kDa)	$\overline{M_n}$ SEC[c] (kDa)	$Đ_m$ SEC[c]
20 (4 × 5)	20:1:0.2	4	99	21	3.4	1.8	1.45
40 (4 × 10)	40:1:0.2	8	95	40	6.3	3.2	1.40
80 (4 × 20)	80:1:0.2	8	99	82	12.9	3.2	1.48
120 (4 × 30)	120:1:0.2	12	92	120	18.8	1.9	1.35
200 (4 × 50)	200:1:0.2	14	96	198	31.0	3.5	1.29

[a] [I] = 4[OH] for *meso*-erythritol, [MAn]=[PO]
[b] ^{1}H NMR in $CDCl_3$
[c] SEC in THF, RI detector, PS standard

These studies determined the optimal concentration conditions for the synthesis of four-arm star PPM with various DPs, from 20 to 200. The synthesis conditions and the molecular characteristics obtained by ^{1}H NMR and size exclusion chromatography (SEC) in tetrahydrofuran (THF) are summarized in the Table 5.2. A strong correlation between

expected DPs and DPs determined from ^{1}H NMR was observed. As reported previously for star polymers, the SEC profiles of four-arm PPM (Figure S8-S12) showed monomodal peaks shifted to earlier elution times compared with the corresponding linear polymer, due to their smaller hydrodynamic volume, inherent to the star architectures. Consequently, the apparent $\overline{M_n}$ values are lower than the actual values. The molar mass distributions ($Đ_m$) were between 1.28-1.48, corresponding to the $Đ_m$ range reported for the PPM synthesis by ROCOP of MAn with PO.[107]

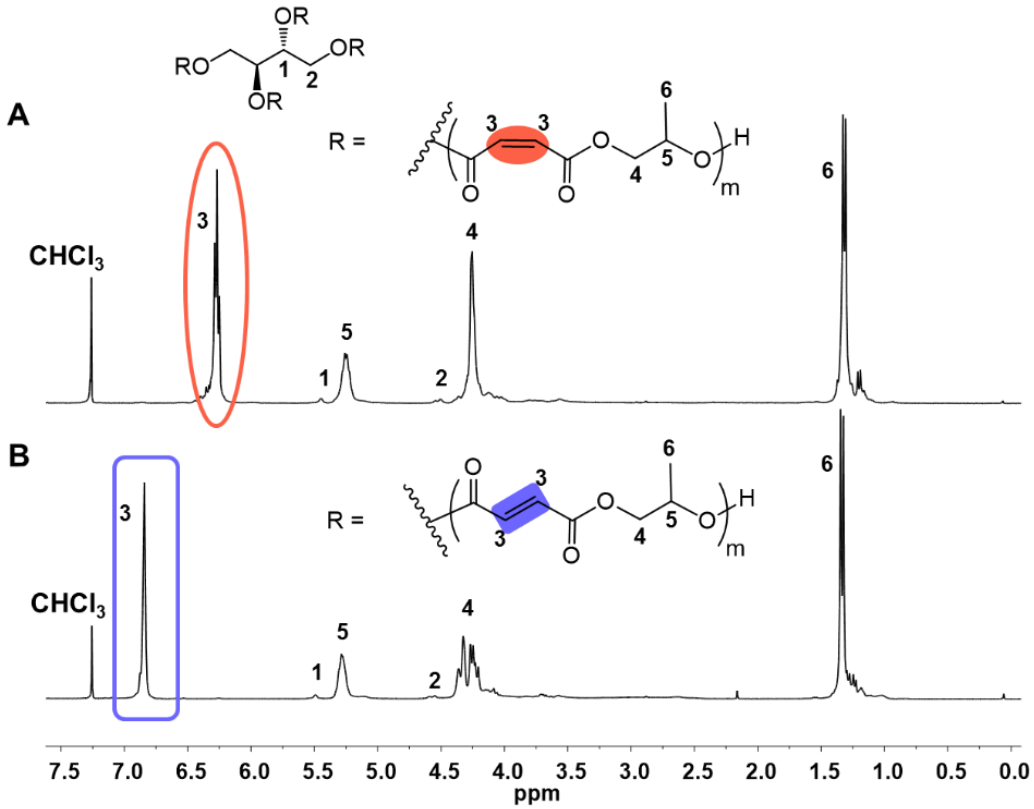

Figure 5.3. (A) ^{1}H NMR spectrum of four-arm star-shaped PPM DP 40 and (B) ^{1}H NMR spectrum of four-arm star-shaped PPF DP 40 with a *meso*-erythritol core (500 MHz, 303 K, $CDCl_3$).

To confirm the arm number of star PPM, the intrinsic viscosities of star PPM DP40 and linear PPM DP40 were measured in THF. The values were obtained by plotting the reduced viscosity ($\eta_{red} = \eta_{sp}/C$) and the inherent viscosity ($\eta_{inh} = \ln(\eta_r/C)$ with the

concentration and found to be $[\eta]_{star} = 6.4\times10^{-3}$ L·g^{-1} and $[\eta]_{linear} = 7.4\times10^{-3}$ L·g^{-1} (Figure S13). The ratios $g' = [\eta]_{star}/[\eta]_{linear}$ was equal to 0.86, the value $g = 6f / [(f+1)(f+2)]$ for f = 4 (arms) was 0.8, and consequently $g^{1/2} = 0.89$. The relationship $g^{1/2}/g' = 1.03 \approx 1.0$ confirmed the number of arms is four. Hence, the copolymerization of MAn and PO using $Mg(BHT)_2(THF)_2$ as a catalyst initiates both from primary alcohol and secondary alcohol sources.

^{1}H NMR spectra obtained before and after isomerization reaction attested that star PPM (Figure 5.3A) was successfully isomerized to star PPF (Figure 5.3B) by showing the disappearance of the proton resonance signal corresponding to *cis*-alkene protons (δ = 6.3 ppm) and the appearance of the new proton resonance signal corresponding to *trans*-alkene protons (δ = 6.7 ppm). All the other ^{1}H NMR spectra are shown in supporting information (Figure S8-S12).

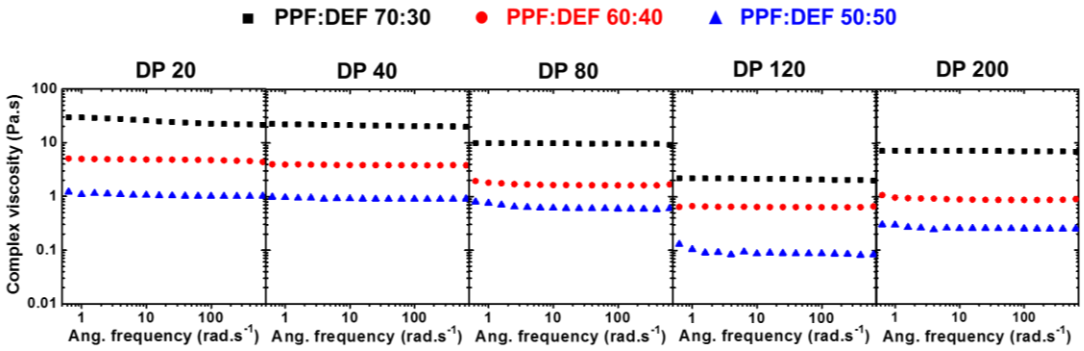

Figure 5.4. Complex viscosity (η*) of PPF:DEF solutions (without photoinitiators and radical scavenger) as a function of DP of star PPF (20, 40, 80, 120 and 200).

The complex viscosities (η*) of star PPF resin formulations in diethyl fumarate (DEF) were then investigated as function of DP and PPF:DEF weight ratio (*i.e.*, 50:50, 60:40 and 70:30). The zero-shear viscosity (η_0) calculated by extrapolation of the complex viscosity to zero angular frequency from a plot of complex viscosity *versus* angular

frequency (Figure 5.4).The zero-shear viscosity (η_0) as a function of number-average molar mass ($\overline{M_n}$) of star PPF are presented in Figure 5.5.

The zero-shear viscosity values (η_0) for the PPF:DEF weight ratio 70:30 (black squares in Figure 5.6), for each DP, were found, as expected, to be systematically higher than the values obtained for the PPF:DEF weight ratio 60:40 (red circles) which are higher than that of the PPF:DEF weight ratio 50:50 (blue triangle). Interestingly, the star shape caused an important and linear decrease of the zero-shear viscosity as the DP increased from 20 to 120, followed by a slight increase for DP200. On the contrary, for the linear PPF oligomers, we previously showed that increasing DP leads to a drastic increase of the zero-shear viscosity,[234] which makes it impossible to 3D print resin based on PPF with DP higher than about 20 and limits the exploration of mechanical properties of the materials obtained.

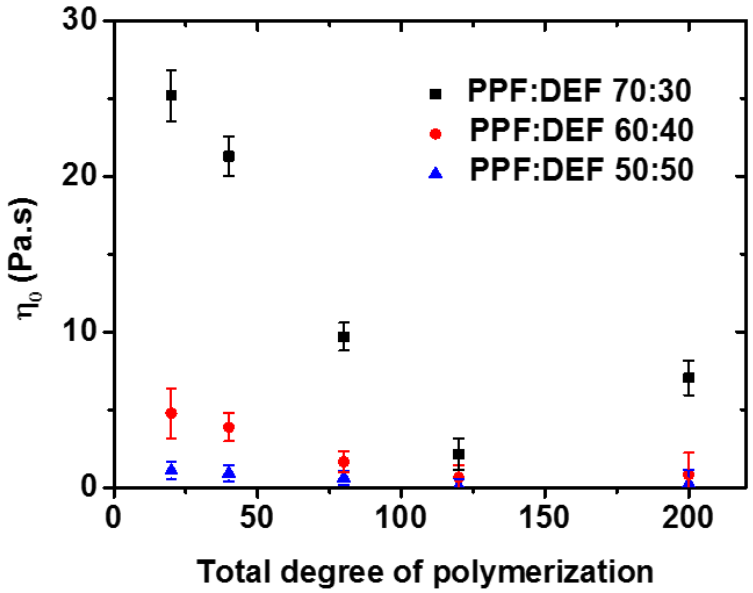

Figure 5.5. Zero-shear viscosity (η_0) of PPF:DEF solutions as a function of DP of star PPF for three various PPF:DEF ratios (50:50, 60:40 and 70:30).

Because of their low viscosity, PPF:DEF (50:50) resins based on the four-arm star PPF DP40 and DP200 were used for digital light processing (DLP) type 3D printing of gyroid scaffolds, after addition of photo-initiators and radical scavenger. Linear DP10 PPF oligomer resin (50:50) was also used for comparison. Cure tests and printing tests were performed to determine the most appropriate UV exposure time/layer for each formulation. A 25 μm layer thickness allowed for a better attachment of the gyroid structures on the basement plate while an increase in DP of PPF used in the formulation led to a significant decrease of the curing time/layer. For instance, for the linear PPF DP10, a curing time/layer of 225 s was necessary, whereas such process only took 95 s and 60 s for resins formulated with star PPF at DP40 and DP200 respectively. Consequently, the total printing duration of scaffolds with a 4 mm height has been reduced from more than 13 h for the linear DP10 to less than 5.5 h for the star DP200.

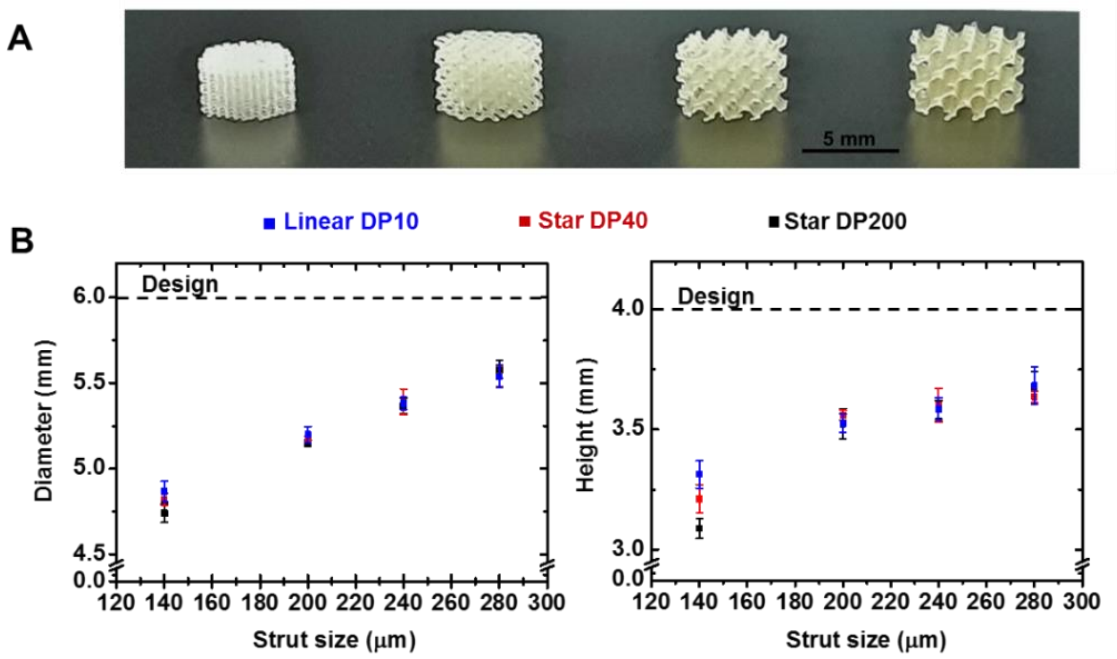

Figure 5.6. (A) Pictures of scaffolds based on star PPF DP200 with different strut sizes, from left to right: 140, 200, 240 and 280 μm. (B) Diameter (left) and height (right) of the scaffolds depending on their strut size and the PPF used.

Porous, cylindrical scaffold were printed using CAD files describing gyroid structures with four different architectures with constant pore geometry and porosity (88.2 %) but varying the strut size (140, 200, 240 and 280 μm) and consequently the pore size (respectively 489; 699, 838 and 978 μm) (Figure 5.6A). After printing, uncrosslinked PPF:DEF solution was removed from the scaffolds and the scaffold were post-cured under UV irradiation for 45 min or 90 min. This step is necessary to ensure a higher crosslinking ratio and consequently improve the mechanical properties, but the effects of its duration were not previously investigated. Dimensions (*i.e.*, diameter and height) of these printed scaffolds were measured with a digital caliper to quantify the shrinkage (Figure 5.6B).

For the three different PPF, the shrinkage phenomenon, induced smaller values than expected both in diameter and in height. Moreover, the smaller the strut size was, the higher this discrepancy was observed. A possible reason is that small strut sizes facilitate the photo-crosslinking and consequently the shrinkage by reducing the chain-to-chain distance. However, no significant differences were triggered by the PPF nature used except for scaffolds with a strut size of 140 μm for which star PPF DP200 showed a more shrinkage in height. In addition, dimensional values obtained after 45 min or 90 min of post-curing were similar, which suggests that shrinkage occurred during 3D printing. Since the reproducibility of the shrinkage was observed, highlighted by the reasonable error bars, the minor disparities between the CAD model and the scaffolds obtained can be predicted and compensated for.

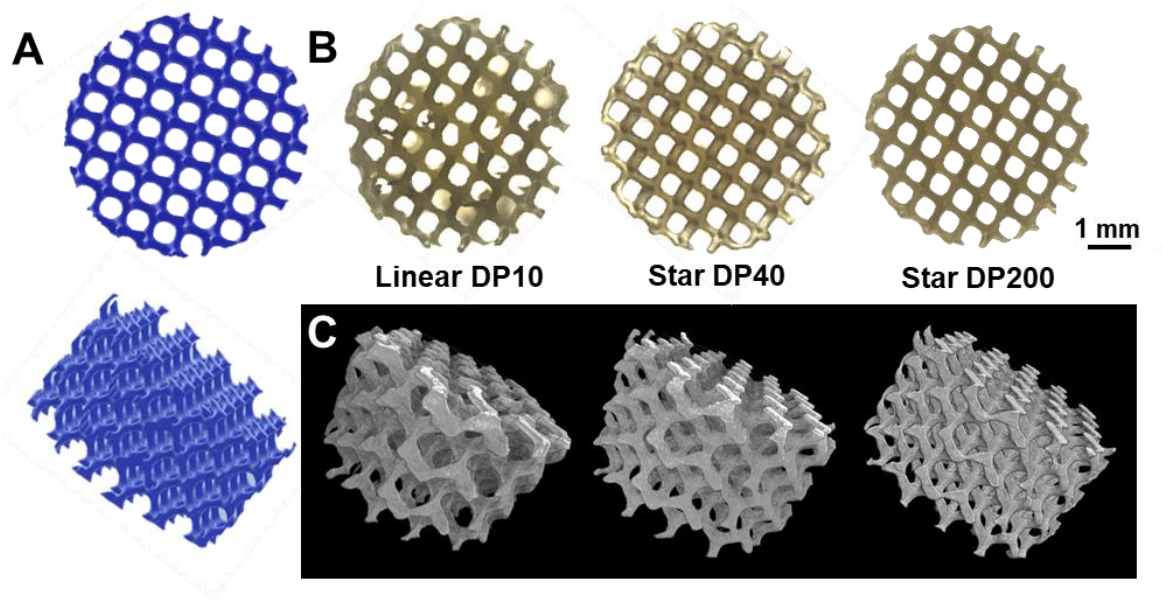

Figure 5.7. (A) CAD file was created in Matlab using the Schoen gyroid triply periodic minimal surface with 200 μm strut size, 699 μm pore size, and 88.2% porosity. (B) Optical micrographs of the top of the scaffolds obtained from different PPF samples (from left to right: linear PPF DP10, star PPF DP40, star PPF DP200). (C) μ-CT images of the scaffolds obtained from different PPF samples (from left to right: linear PPF DP10, star PPF DP40, star PPF DP200).

As the internal pore geometry can directly influence the capacity of a scaffold to guide neo-tissues, the infusion of vasculature into the defect, cell seeding and/or nutrient flow for *ex vivo* culturing, it is also important to characterize the relationship between resin formulations, printing parameters and scaffold architectures. For this purpose, the scaffolds were imaged by optical microscope to depict the gyroid architecture features in greater detail and to determine their actual strut size. The structure of the gyroid scaffolds was also characterized by X-ray micro-computed tomography (μ-CT) to determine their total porosity. The corresponding pore sizes were calculated. Figure 5.7 shows the resulting images for the scaffolds with a strut size of 200 μm with the CAD model used.

Table 5.3. Characterization summary of the scaffolds obtained by DLP 3D printing.

	Strut size (μm)[a]	Porosity (%)[b]	Pore size (μm)[c]
CAD model 1	140	88.2	489
Linear PPF DP10	131 (± 11)	85.2	389
Star PPF DP40	142 (± 10)	90.5	575
Star PPF DP200	141 (± 9)	90.8	583
CAD model 2	200	88.2	699
Linear PPF DP10	246 (± 54)	81.2	613
Star PPF DP40	194 (± 13)	88.1	674
Star PPF DP200	196 (± 12)	86.3	616
CAD model 3	240	88.2	838
Linear PPF DP10	242 (± 26)	77.9	532
Star PPF DP40	238 (± 17)	87.3	790
Star PPF DP200	237 (± 11)	88.3	833
CAD model 4	280	88.2	978
Linear PPF DP10	393 (± 37)	80.5	952
Star PPF DP40	286 (± 24)	87.8	976
Star PPF DP200	275 (± 11)	87.6	928

[a]obtained by optical microscopy; [b]obtained by μ-CT; [c] calculated.

Optical micrographs and μ-CT images of scaffolds based on the linear PPF DP10 revealed a less defined structure and photocrosslinked PPF:DEF resin within the pores, while scaffolds obtained from the star PPF were better homogeneous with highly reproducible spatial arrangement of pores. Similar trend was found in scaffolds with other CAD model designs as shown in supporting information (Figure S14, S15 and S16, with

140 μm, 240 μm and 280 μm as strut size respectively). Porosity values, actual strut sizes and pore sizes are summarized in Table 5.3.

These values highlighted a significant discrepancy between the CAD models and the actual scaffolds for the linear DP10 and on the contrary, a good fidelity between the desired characteristic dimensions and those obtained for the star PPF. This phenomenon can be explained by that a larger UV irradiation time/layer was needed to print resins formulated with linear PPF at DP10 level. Previous studies showed that increasing the irradiation time/layer can cause undesirable "dark" curing, photo-crosslinking of the resin in areas where no light is exposed, induced by diffusion of radical species..[179] Consequently, the use of star PPF with higher molar mass allowed a shorter irradiation time/layer and improved the 3D printing fidelity, resulting in well-defined scaffolds with high porosity and thin strut sizes.

Mechanical properties of these scaffolds were measured *via* uniaxial compression tests with a constant crosshead velocity of 0.5 mm·min^{-1} at room temperature. Scaffolds with post-curing time of 45 min or 90 min were characterized by monitoring stress and strain throughout the experiment (Figure 5.8A-J). The compressive moduli were calculated using the slope of linear fitting in the linear regime. The reported results are average values from five individual measurements and the associated errors are the standard deviations (Figure 5.9).

Based on types of PPF used, designs of scaffold architecture and durations of post-curing, the stress *versus* strain curves highlighted completely different behaviors (Figure 5.8A-L). Scaffolds with the lowest strut size, *i.e.,* 140 μm, exhibited brittle fracture, irrespective of the PPF used or the post-curing time (Figure 5.8A, 5.8E and 5.8I).

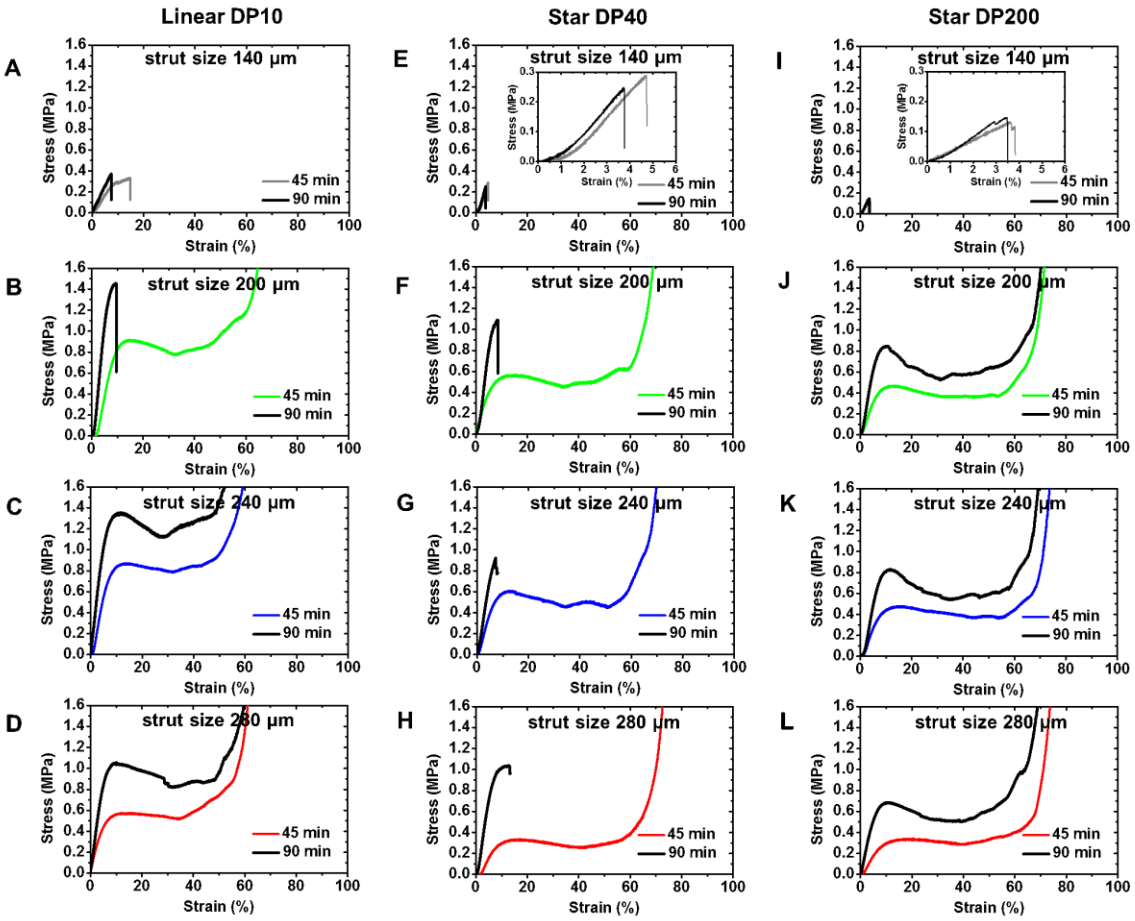

Figure 5.8. Stress *versus* strain curves of scaffolds after 45 min or 90 min of post-curing.

All the other scaffolds that underwent a short post-curing time of 45 min, supported the applied load with no apparent sudden failure. Most of the scaffolds showed a trend of successive collapse of in-plane pores (perpendicular to the force loading direction), the plateau region on the stress-strain curve, which is a characteristic property of low-strain failure. For the scaffolds based on star PPF DP40 and PPF DP200 and strut size of 280 μm (respectively Figure 5.8H and 5.8L), the curves showed an initial linear elastic deformation after which stress nonlinearly increased with the applied strain to reach a plateau regime, highlighting lack of failure and stretching of struts.

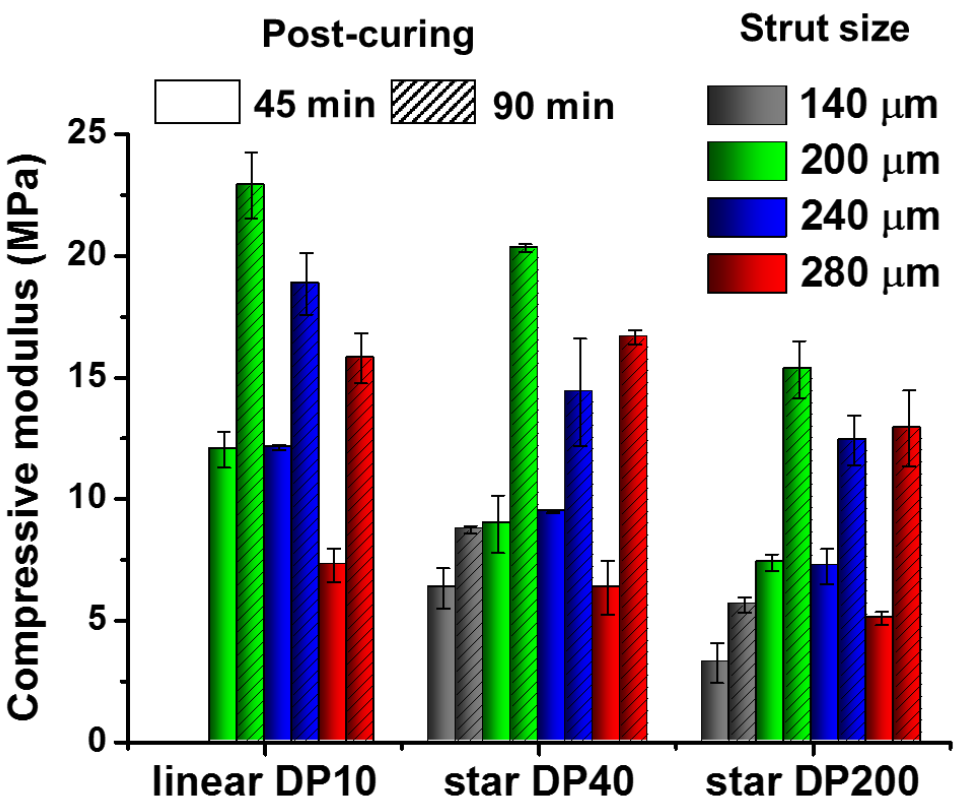

Figure 5.9. The 3D printed scaffolds after 90 min of post-curing exhibited a higher compressive modulus compared to those obtained after 45 min of post-curing.

Upon further compression, the structure grew stronger after the densification as the slope of the curve increased. This densification step appeared earlier for the linear DP10, in a 25-40 % strain range, than that of the star PPF, in a 45-63 % strain range, indicating higher elasticity of star PPF DP40 and 200 polymers themselves than linear PPF DP10. After a post-curing of 90 min, the scaffolds of linear DP10 and strut sizes 140 and 200 μm and all the scaffolds of star PPF DP40 exhibited brittle fracture while the other scaffolds of linear DP10 and star DP200 displayed only a low-strain failure with successive pore collapse. For these scaffolds obtained after a longer post-curing, the densification occurred earlier than those after only 45 min, due to higher crosslinking ratios. Compressive modulus varied between 3.26 ± 0.83 MPa and 12.3 ± 0.74 MPa for scaffolds that underwent

45 min post-curing time, and between 5.65 ± 0.30 MPa and 22.9 ± 1.35 MPa for scaffolds after 90 min post-curing time, so compressive modulus was generally found to be larger after a longer post-cure treatment. Consequently, a longer post-curing time can increase the compression modulus while make the scaffolds more brittle.

The compression tests led to another inquiry: how is the shape-recovery property of those scaffolds that did not show failure, that are those of star DP40 and DP200 after 45 min post-curing? To answer this question, the height of the scaffolds was measured over time just after compression and the actual height/initial height ratio was plotted with time (Figure 5.10).

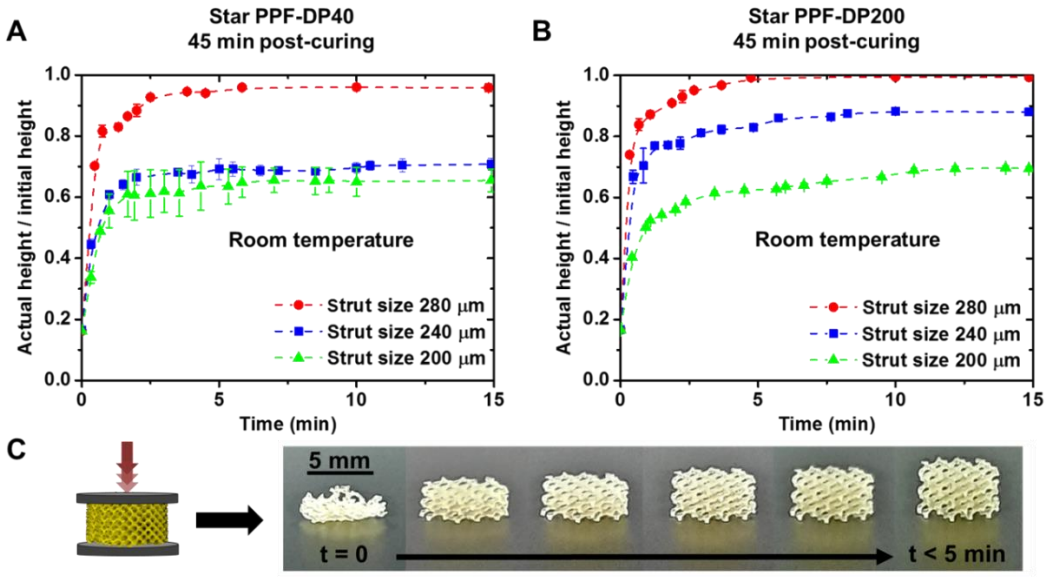

Figure 5.10. Evaluation of shape recovery behavior at room temperature after compression of scaffolds with 45 min post-curing time. (A) Actual height/initial height ratio *versus* time for scaffolds based on star PPF DP40. (B) Actual height/initial height ratio *versus* time for scaffolds based on star PPF DP200. (C) Pictures of a scaffold (four-arm PPF DP200, strut size 280 μm, 45 min post-curing) during the recovery.

At room temperature, scaffolds of star PPF DP40 with strut sizes of 200 and 240 μm showed partial recovery, about 60 % and 70% height recovery and the strut size 280

μm scaffolds with start PPF DP40 showed almost complete recovery, about 95 % in 5 min (Figure 5.10A). In a different way, star PPF DP200 showed a better recovery as the strut size increased, the scaffold with a 200 μm strut size reached 70 % of recovery, while scaffolds with strut sizes of 240 and 280 μm led to 90 % and 100 % of recovery in 15 min respectively (Figure 5.10B). These shape-recovery behaviors can be explained according to the scaffold status after compression. For instance, scaffolds that showed an elastic deformation and consequently no failure during compression test were able to recover their shape once the compressive force was removed.

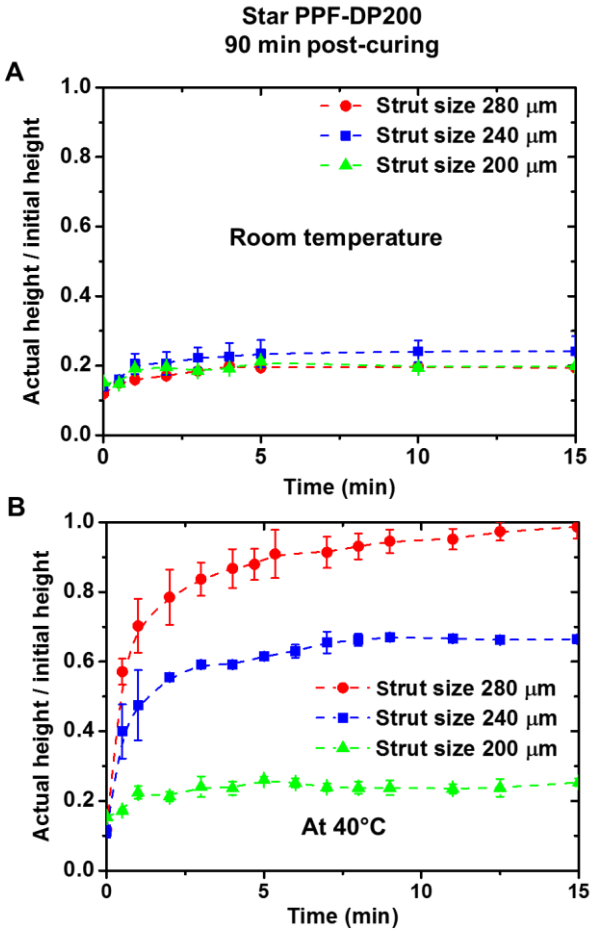

Figure 5.11. Evaluation of the shape recovery property after compression for scaffolds after 90 min of post-curing. (A) Actual height/initial height ratio *versus* time for scaffolds based on star PPF DP200 recovered at room temperature. (B) Actual height/initial height ratio *versus* time for scaffolds based on star PPF DP200 recovered at 40 °C.

Then, we investigated the recovery properties at room temperature and at 40 °C using scaffolds printed with star PPF DP200 with 90 min post-curing time (Figure 5.11). At room temperature, these scaffolds were not able to recover more than 30% of their height as showed in Figure 5.11A. However, at 40 °C, scaffolds with larger strut sizes displayed better recovery behaviors (65% recovery for strut size 240 µm and 100% recovery for strut size 280 µm), and scaffolds with the smallest strut size, 200 μm, presented a poorer recovery, which was similar to that obtained at room temperature.

Scaffolds of star PPF DP200 were characterized by optical microscopy and μ-CT before compression and after compression and total recovery (Figure 5.12). Pictures showed very similar structures and no change in the porosity value was observed.

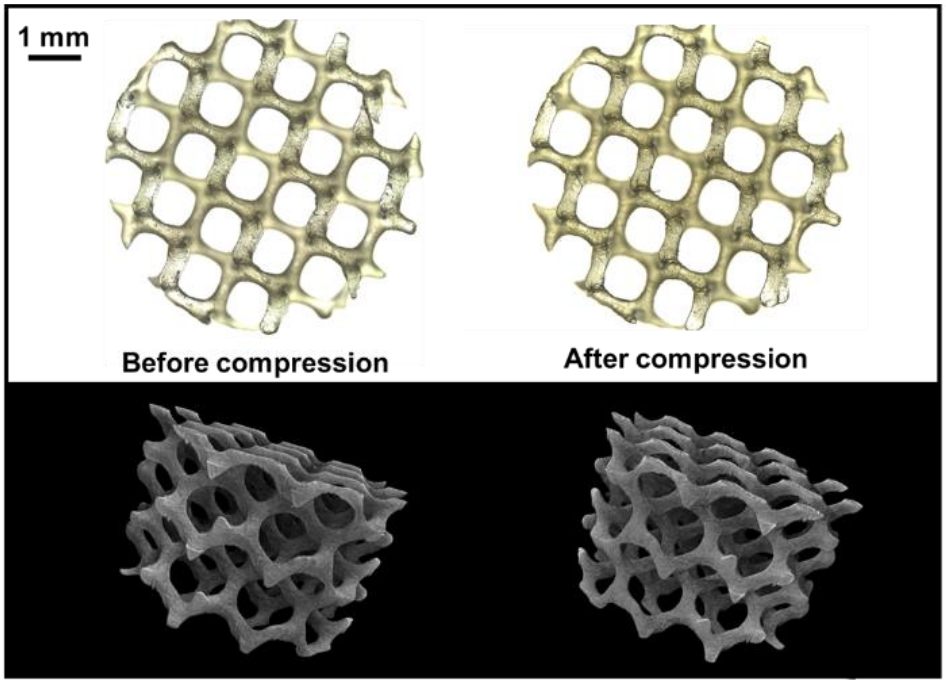

Figure 5.12. Optical micrographs of the top of the scaffolds of star PPF DP200 and μ-CT images before and after compression and complete recovery.

Consequently, these highly porous scaffolds, based on star PPF DP200 and with strut size of 280 μm showed good shape-memory behavior after compression. This

recovery process can happen at room temperature or higher temperature (e.g., 40 °C), depending on the duration of the post-curing.

Therefore, the mechanical characteristics of PPF scaffolds in this study are influenced by combined factors: types of PPF used in resin formulation, the crosslinking degrees (e.g., tuned by post-curing duration), strut size of the scaffolds.

5.5 Conclusion

The synthesis of four-arm PPF *via* a core-first approach was reported in this study using sugar-based alcohol *meso*-erythritol as an initiator with total DPs in a 20-200 range. Their star-shape was confirmed by combination of ^{1}H NMR spectroscopy, size exclusion chromatography (SEC), and viscosity measurements. These star PPF allowed for the preparation of PPF:DEF resins with complex viscosities compatible with DLP 3D printing with high DP values, resulting in the ability to print PPF with $\overline{M_n}$ nearly 8 times larger than that of the largest linear PPF previously printed. Highly porous gyroid scaffolds were manufactured with two different four-arm PPF, *i.e.*, DP40 and DP200, and one linear oligomer DP10 for comparison. The use of larger DPs lead to a faster printing speed, resulting in better-defined gyroid structures. Their compression moduli were found to increase with the post-curing time. Scaffolds based on star PPF200 were able to recover their shape after compression, opening previously unexplored shape memory properties of PPF-based scaffolds. Future investigations concern their degradability and ability to self-fit into a complex shape of a bone defect.

5.6 Acknowledgments

The Ohio Department of Development (AFMC) and 21st Century Medical Technologies are acknowledged for financial support. M.L.B. is grateful for support from the W. Gerald Austen Endowed Chair in Polymer Science and Polymer Engineering from the Knight Foundation.

CHAPTER VI

SUMMARY

To tackle the unmet material supply issues in high-resolution 3D printing manufacturing process (*e.g.*, digital light processing, DLP) for patient-specific regenerative medical applications, a series of bioresorbable poly(propylene fumarate) (PPF) oligomers with well-defined properties were synthesized *via* ring-opening copolymerization (ROCOP) methods using biologically tolerant magnesium-based catalysts. To meet the viscosity requirement for DLP 3D printing, PPF-based resins with printable viscosity were prepared followed by evaluations of their 3D printing characteristics and mechanical behaviors of the 3D printed tensile bars and porous scaffolds.

Chemical structures of ROCOP synthesized linear PPF oligomers were thoroughly characterized by ^{1}H NMR, ^{13}C NMR, matrix-assisted laser desorption/ionization (MALDI), Fourier transform infrared spectroscopy (FTIR) and UV-Visible spectroscopy (UV-vis). Molecular mass information was obtained by size exclusion chromatography (SEC) and MALDI. Physical properties of PPF were evaluated by differential scanning calorimetry (DSC) and intrinsic viscosity measurements. Contrary to traditional step-growth synthetic method, the ROCOP is a more reproducible synthetic route to generate PPF of desired molecular mass with higher yields (*e.g.*, 50-65% compared to 20-35%) and enables large batch synthesis

(200g/batch). These ROCOP synthesized PPF oligomers also exhibited narrow molecular mass distribution (1.3-1.6). These properties allow to predict the viscosity of PPF, which is an important parameter in DLP 3D printing of PPF-based resins. Narrow molecular mass distribution ($Đ_m$) can also contribute to control mechanical performances and resorption profiles for the 3D printed products, which are of primary importance for regenerative medicine applications such as bone tissue regeneration substitutes. Precisely controlled number-average molecular mass ($\overline{M_n}$), molecular mass distribution and viscosity properties will facilitate a predictable pathway for good manufacturing practice certification.

Subsequently, well-defined linear PPF ($Đ_m$ < 1.6) were synthesized at three number-average molecular mass levels ($\overline{M_n}$) from 1.1 kDa to 2.0 kDa using this ROCOP method. They were further used in DLP 3D printing to evaluate their 3D printing and mechanical properties. PPF-based resin viscosity can be adjusted into the DLP printable range (< 2 Pa·s) by decreasing chain length of PPF used in resin formulation, increasing reactive diluent (*i*.e., diethyl fumarate (DEF)) weight ratio in resin formulation and/or elevating 3D printing temperature. The complex viscosity of linear PPF:DEF solutions was found increasing with the chain length and following an Arrhenius model, providing a predictable resin complex viscosity at a designated temperature (between 25-55 °C). These PPF with narrow $Đ_m$ showed excellent 3D printing consistency regarding the dimensions of 3D printed tensile bars. FTIR and swelling tests denoted the crosslinking density of these 3D printed PPF products can be tuned with UV exposure duration. The longer the UV exposure time, the higher the crosslinking density, opening a window to tune the mechanical and degradation behavior of these 3D printed objects for future works. Mechanical evaluations of these tensile bars demonstrated the ability of using

such 3D printed PPF-based materials for bone tissue applications as their elastic moduli (from 178 ± 38 MPa to 199 ± 8 MPa) fell into the range of human trabecular bone.

As linear PPF oligomers have shown a drastic increase in complex viscosity of their corresponding PPF:DEF resins when increasing the $\overline{M_n}$ of PPF used, it is challenging to 3D print PPF of larger $\overline{M_n}$. Another strategy was investigated with the aim to produce less viscous resins while increasing the $\overline{M_n}$ of PPF used in the resin formulation and to evaluate properties of these 3D printed products.

A series of five four-arm PPF with total degree of polymerization (DP) from 20 to 200 were synthesized *via* a core-first approach using sugar-based alcohol *meso*-erythritol as an initiator. Their star-shape was confirmed by combination of ^{1}H NMR, SEC, and intrinsic viscosity measurements. The copolymerization process revealed a strong concentration-dependence of the DP obtained; higher total monomer concentration was required to reach larger DP PPF (*e.g.*, 2 M for DP20 *vs*. 14 M for DP200). Kinetic studies demonstrated star-shaped PPF can reach a designated DP in shorter time than their linear analogues. Further complex viscosity measurements of resins made from star-shaped PPF and DEF showed a decrease in complex viscosity as the DP of PPF increased, allowing 3D printing of PPF with $\overline{M_n}$ eight times larger than that of the largest linear PPF previously printed using the same DLP 3D printing technique.

The scale-up synthesis of linear DP10, star-shaped DP40 and DP200 PPF were performed to obtain enough polymers for DLP 3D printing of cylindrical gyroid scaffolds with a prescribed diameter of 6 mm, height of 4 mm, a target porosity of 88.2%, and four strut sizes (140, 200, 240 and 280 μm). 3D printing was faster for resins containing PPF at

larger DP. These scaffolds were then post-cured in a UV chamber for 45 min and 90 min to improve their mechanical property. Porosity and strut size of each printing group were thoroughly evaluated by optical microscopy and μ-CT. A significant discrepancy appeared between the computer-aided design (CAD) models and the actual scaffolds for linear DP10 PPF, and on the contrary, a good fidelity was found between the designed dimensions and those from printed scaffolds using star PPF. The longer printing time necessary for curing resins of linear PPF oligomer showed an undesirable lateral curing.

For each DP group, compressive mechanical properties were significantly influenced by the post-curing duration, and compressive moduli were found larger for scaffolds with longer post-curing time. Interestingly, depending on the DP of PPF, strut size, and/or post-curing duration, these scaffolds displayed brittle fracture, low-strain failure or linear elastic deformation under compression. Scaffolds based on star PPF with DP200 were able to recover their shape after compression, at room temperature for those with 45 min post-curing and at 40 °C for those with 90 min post-curing. The largest strut size (280 μm) was found to allow for a faster and better shape recovery. These observations revealed a previously unexplored field, shape recovery properties of 3D printed PPF-based scaffolds. Future investigations regarding their degradability and their potential to self-fit into a complex shape of bone defect.

Accomplishments displayed in this dissertation provided a scale-up synthesis method to reproducibly generate a bioresorbable material, which can be used in high-resolution 3D printing techniques, allowing manufacturing of scaffolds that has the potential to fill the resorption time gap between the degradation of polylactides (typically within weeks), and poly(ε-caprolactone) (over the course of years). This is a critical

window for the presence and absence of a scaffold. Initially the presence of a scaffold facilitates either seeded and/or host cells and vasculature to infuse the tissue into the defect space. Thereafter, in tissues that require remodeling to take on their adult function, the absence of scaffolding material is essential. Designing the formulation of PPF-based resins using chemical and physical strategies, combining the feasibility from computer-aided design, allowed for 3D printing of PPF at higher molecular mass level, and resulted in diverse mechanical properties. Such reproducible synthetic methods and resin viscosity tuning techniques not only paved the road to further identify the potential of using 3D printed PPF scaffolds in regenerative medicine field, but also can be adapted for the developing other related biomaterials.

REFERENCES

1. ISO/ASTM Standard 52900, 2015, "Additive Manufacturing-General Principles-Terminology". ISO: 2015.

2. Chua, C. K.; Leong, K. F., *3D Printing and Additive Manufacturing: Principles and Applications (with Companion Media Pack) of Rapid Prototyping Fourth Edition*. World Scientific Publishing Company: 2014.

3. Bose, S.; Vahabzadeh, S.; Bandyopadhyay, A., Bone tissue engineering using 3D printing. *Materials today* **2013,** *16* (12), 496-504.

4. Rengier, F.; Mehndiratta, A.; Von Tengg-Kobligk, H.; Zechmann, C. M.; Unterhinninghofen, R.; Kauczor, H.-U.; Giesel, F. L., 3D printing based on imaging data: review of medical applications. *International journal of computer assisted radiology and surgery* **2010,** *5* (4), 335-341.

5. Trenfield, S. J.; Awad, A.; Goyanes, A.; Gaisford, S.; Basit, A. W., 3D printing pharmaceuticals: drug development to frontline care. *Trends in pharmacological sciences* **2018**.

6. Bill, J. S.; Reuther, J. F.; Dittmann, W.; Kübler, N.; Meier, J. L.; Pistner, H.; Wittenberg, G., Stereolithography in oral and maxillofacial operation planning. *International journal of oral and maxillofacial surgery* **1995,** *24* (1), 98-103.

7. Hull, C. W., Apparatus for production of three-dimensional objects by stereolithography. Google Patents: 1986.

8. Mukhopadhyay, S.; Poojary, R. In *A review on 3D printing: Advancement in healthcare technology*, 2018 Advances in Science and Engineering Technology International Conferences (ASET), IEEE: 2018; pp 1-5.

9. Dodziuk, H., Applications of 3D printing in healthcare. *Kardiochirurgia i torakochirurgia polska= Polish journal of cardio-thoracic surgery* **2016,** *13* (3), 283.

10. Truby, R. L.; Lewis, J. A., Printing soft matter in three dimensions. *Nature* **2016,** *540* (7633), 371.

11. Park, C.; Kim, K.-H.; Lee, Y.-M.; Seol, Y.-J., Advanced engineering strategies for periodontal complex regeneration. *Materials* **2016,** *9* (1), 57

12. Ko, D.-H.; Gyak, K.-W.; Kim, D.-P., Emerging microreaction systems based on 3D printing techniques and separation technologies. *Journal of Flow Chemistry* **2017,** *7* (3-4), 72-81.

13. van Bodegom, L.; van der Meulen, B., Additive bio-manifacturing: 3D printing for medical recovery and human enhancement: study STOA. **2018**.

14. Awad, A.; Trenfield, S. J.; Gaisford, S.; Basit, A. W., 3D printed medicines: A new branch of digital healthcare. *International journal of pharmaceutics* **2018**.

15. Kaye, R.; Goldstein, T.; Zeltsman, D.; Grande, D. A.; Smith, L. P., Three dimensional printing: A review on the utility within medicine and otolaryngology. *International Journal of Pediatric Otorhinolaryngology* **2016,** *89*, 145-148.

16. Liang, K.; Carmone, S.; Brambilla, D.; Leroux, J.-C., 3D printing of a wearable personalized oral delivery device: A first-in-human study. *Science advances* **2018,** *4* (5), eaat2544.

17. Bosc, R.; Hersant, B.; Carloni, R.; Niddam, J.; Bouhassira, J.; De Kermadec, H.; Bequignon, E.; Wojcik, T.; Julieron, M.; Meningaud, J.-P., Mandibular reconstruction after cancer: an in-house approach to manufacturing cutting guides. *International journal of oral and maxillofacial surgery* **2017,** *46* (1), 24-31.

18. Haidar, Z., 3D printed titanium implants: colossal FDA-approved leap towards "personalized" maxillo-facial surgery. *Journal of Oral Research* **2017,** *6* (11), 282-284.

19. Schantz, J.-T.; Lim, T.-C.; Ning, C.; Teoh, S. H.; Tan, K. C.; Wang, S. C.; Hutmacher, D. W., Cranioplasty after trephination using a novel biodegradable burr hole cover: technical case report. *Operative Neurosurgery* **2006,** *58* (suppl_1), ONS-E176-ONS-E176.

20. Childers, E. P.; Wang, M. O.; Becker, M. L.; Fisher, J. P.; Dean, D., 3D printing of resorbable poly (propylene fumarate) tissue engineering scaffolds. *Mrs Bulletin* **2015,** *40* (2), 119-126.

21. Zopf, D. A.; Hollister, S. J.; Nelson, M. E.; Ohye, R. G.; Green, G. E., Bioresorbable airway splint created with a three-dimensional printer. *New England Journal of Medicine* **2013,** *368* (21), 2043-2045.

22. Choi, J.; Kim, K.; Kim, T.; Liu, G.; Bar-Shir, A.; Hyeon, T.; McMahon, M. T.; Bulte, J. W.; Fisher, J. P.; Gilad, A. A., Multimodal imaging of sustained drug release from 3-D poly (propylene fumarate)(PPF) scaffolds. *Journal of controlled release* **2011,** *156* (2), 239-245.

23. Rezaie, H. R.; Esnaashary, M.; Öchsner, A., 3D Printing Technologies for Drug Delivery. In *A Review of Biomaterials and Their Applications in Drug Delivery*, Springer: 2018; pp 53-60.

24. Rahmani Del Bakhshayesh, A.; Annabi, N.; Khalilov, R.; Akbarzadeh, A.; Samiei, M.; Alizadeh, E.; Alizadeh-Ghodsi, M.; Davaran, S.; Montaseri, A., Recent advances on biomedical applications of scaffolds in wound healing and dermal tissue engineering. *Artificial cells, nanomedicine, and biotechnology* **2018,** *46* (4), 691-705.

25. Gu, B. K.; Choi, D. J.; Park, S. J.; Kim, M. S.; Kang, C. M.; Kim, C.-H., 3-dimensional bioprinting for tissue engineering applications. *Biomaterials research* **2016,** *20* (1), 12.

26. Do, A. V.; Khorsand, B.; Geary, S. M.; Salem, A. K., 3D printing of scaffolds for tissue regeneration applications. *Advanced healthcare materials* **2015,** *4* (12), 1742-1762.

27. Vinatier, C.; Guicheux, J., Cartilage tissue engineering: From biomaterials and stem cells to osteoarthritis treatments. *Annals of physical and rehabilitation medicine* **2016,** *59* (3), 139-144.

28. Hollinger, J. O.; Winn, S.; Bonadio, J., Options for tissue engineering to address challenges of the aging skeleton. *Tissue Engineering* **2000,** *6* (4), 341-350.

29. Hatton, G. B.; Madla, C. M.; Gaisford, S.; Basit, A. W., Medical applications of 3D Printing. In *3D Printing of Pharmaceuticals*, Springer: 2018; pp 163-182.

30. Wang, S.; Lee, J. M.; Yeong, W. Y., Smart hydrogels for 3D bioprinting. *International Journal of Bioprinting* **2015,** *1* (1).

31. Black, C. R.; Goriainov, V.; Gibbs, D.; Kanczler, J.; Tare, R. S.; Oreffo, R. O., Bone tissue engineering. *Current molecular biology reports* **2015,** *1* (3), 132-140.

32. Jin, K.; Simpkins, J. W.; Ji, X.; Leis, M.; Stambler, I., The critical need to promote research of aging and aging-related diseases to improve health and longevity of the elderly population. *Aging and disease* **2015,** *6* (1), 1.

33. Mahal, A.; McPake, B., Health systems for aging societies in Asia and the Pacific. *Health Systems & Reform* **2017,** *3* (3), 149-153.

34. Gross, B. C.; Erkal, J. L.; Lockwood, S. Y.; Chen, C.; Spence, D. M., Evaluation of 3D printing and its potential impact on biotechnology and the chemical sciences. ACS Publications: 2014.

35. Walker, J. M.; Bodamer, E.; Kleinfehn, A.; Luo, Y.; Becker, M.; Dean, D., Design and mechanical characterization of solid and highly porous 3D printed poly (propylene fumarate) scaffolds. *Progress in Additive Manufacturing* **2017,** *2* (1-2), 99-108.

36. Walker, J. M.; Bodamer, E.; Krebs, O.; Luo, Y.; Kleinfehn, A.; Becker, M. L.; Dean, D., Effect of chemical and physical properties on the in vitro degradation of 3D printed high resolution poly (propylene fumarate) scaffolds. *Biomacromolecules* **2017,** *18* (4), 1419-1425.

37. Goole, J.; Amighi, K., 3D printing in pharmaceutics: A new tool for designing customized drug delivery systems. *International journal of pharmaceutics* **2016,** *499* (1-2), 376-394.

38. Hung, B. P.; Naved, B. A.; Nyberg, E. L.; Dias, M.; Holmes, C. A.; Elisseeff, J. H.; Dorafshar, A. H.; Grayson, W. L., Three-dimensional printing of bone extracellular matrix for craniofacial regeneration. *ACS biomaterials science & engineering* **2016,** *2* (10), 1806-1816.

39. Yu, J.; Xu, Y.; Li, S.; Seifert, G. V.; Becker, M. L., Three-dimensional printing of nano hydroxyapatite/poly (ester urea) composite scaffolds with enhanced bioactivity. *Biomacromolecules* **2017,** *18* (12), 4171-4183.

40. Billiet, T.; Vandenhaute, M.; Schelfhout, J.; Van Vlierberghe, S.; Dubruel, P., A review of trends and limitations in hydrogel-rapid prototyping for tissue engineering. *Biomaterials* **2012,** *33* (26), 6020-6041.

41. Luo, Y.; Dolder, C. K.; Walker, J. M.; Mishra, R.; Dean, D.; Becker, M. L., Synthesis and biological evaluation of well-defined poly (propylene fumarate) oligomers and their use in 3D printed scaffolds. *Biomacromolecules* **2016,** *17* (2), 690-697.

42. Sandström, C. G., The non-disruptive emergence of an ecosystem for 3D Printing—Insights from the hearing aid industry's transition 1989–2008. *Technological Forecasting and Social Change* **2016,** *102*, 160-168.

43. Lu, Y.; Mantha, S. N.; Crowder, D. C.; Chinchilla, S.; Shah, K. N.; Yun, Y. H.; Wicker, R. B.; Choi, J.-W., Microstereolithography and characterization of poly (propylene fumarate)-based drug-loaded microneedle arrays. *Biofabrication* **2015,** *7* (4), 045001.

44. Matsuda, T.; Mizutani, M., Liquid acrylate-endcapped biodegradable poly (ϵ-caprolactone-co-trimethylene carbonate). II. Computer-aided stereolithographic microarchitectural surface photoconstructs. *Journal of Biomedical Materials Research: An Official Journal of The Society for Biomaterials, The Japanese Society for Biomaterials, and The Australian Society for Biomaterials and the Korean Society for Biomaterials* **2002,** *62* (3), 395-403.

45. Smith, K. E.; Dupont, K. M.; Safranski, D. L.; Blair, J.; Buratti, D.; Zeetser, V.; Callahan, R.; Lin, J.; Gall, K., Use of 3D printed bone plate in novel technique to surgically correct hallux valgus deformities. *Techniques in orthopaedics (Rockville, Md.)* **2016,** *31* (3), 181.

46. Morrison, R. J.; Kashlan, K. N.; Flanangan, C. L.; Wright, J. K.; Green, G. E.; Hollister, S. J.; Weatherwax, K. J., Regulatory considerations in the design and manufacturing of implantable 3D-printed medical devices. *Clinical and translational science* **2015,** *8* (5), 594-600.

47. Ngo, T. D.; Kashani, A.; Imbalzano, G.; Nguyen, K. T.; Hui, D., Additive manufacturing (3D printing): A review of materials, methods, applications and challenges. *Composites Part B: Engineering* **2018,** *143*, 172-196.

48. Zadpoor, A. A.; Malda, J., Additive manufacturing of biomaterials, tissues, and organs. Springer: 2017.

49. Rust, B.; Tsaponina, O.; Maniruzzaman, M., Recent Innovations in Additive Manufacturing Across Industries: 3D Printed Products and FDA's Perspectives. *3D and 4D Printing in Biomedical Applications: Process Engineering and Additive Manufacturing* **2019**, 443-462.

50. Domb, A. J.; Khan, W., *Focal controlled drug delivery*. Springer: 2014.

51. Bazaka, K.; Jacob, M., Implantable devices: issues and challenges. *Electronics* **2013,** *2* (1), 1-34.

52. Shegarfi, H.; Reikeras, O., Bone transplantation and immune response. *Journal of Orthopaedic Surgery* **2009,** *17* (2), 206-211.

53. Francois, E. L.; Yaszemski, M. J., Preclinical Bone Repair Models in Regenerative Medicine. In *Principles of Regenerative Medicine*, Elsevier: 2019; pp 761-767.

54. Sheikh, Z.; Hamdan, N.; Ikeda, Y.; Grynpas, M.; Ganss, B.; Glogauer, M., Natural graft tissues and synthetic biomaterials for periodontal and alveolar bone reconstructive applications: a review. *Biomaterials research* **2017,** *21* (1), 9.

55. Poser, J. W., Commercial Non-Allograft Bone Graft Products. In *Translating Biomaterials for Bone Graft*, CRC Press: 2017; pp 75-88.

56. Finkemeier, C. G., Bone-grafting and bone-graft substitutes. *JBJS* **2002,** *84* (3), 454-464.

57. Wang, W.; Yeung, K. W., Bone grafts and biomaterials substitutes for bone defect repair: A review. *Bioactive Materials* **2017,** *2* (4), 224-247.

58. Ong, J.; Guda, T.; Actis, L.; Gaviria, L., Bone Grafting Evolution. In *Translating Biomaterials for Bone Graft*, CRC Press: 2017; pp 15-30.

59. Wang, W.; Caetano, G. F.; Chiang, W.-H.; Braz, A. L.; Blaker, J. J.; Frade, M. A. C.; Bartolo, P. J., Morphological, mechanical and biological assessment of PCL/pristine graphene scaffolds for bone regeneration. *Int. J. Bioprint* **2016,** *2*, 95-104.

60. Tan, L.; Yu, X.; Wan, P.; Yang, K., Biodegradable materials for bone repairs: a review. *Journal of Materials Science & Technology* **2013,** *29* (6), 503-513.

61. Gunatillake, P. A.; Adhikari, R., Biodegradable synthetic polymers for tissue engineering. *Eur Cell Mater* **2003,** *5* (1), 1-16.

62. Domb, A. J. K., J.; Wiseman, D. M., *Handbook of biodegradable polymers*. Harwood Academic Publishers: 1997.

63. Sheikh, Z.; Najeeb, S.; Khurshid, Z.; Verma, V.; Rashid, H.; Glogauer, M., Biodegradable materials for bone repair and tissue engineering applications. *Materials* **2015,** *8* (9), 5744-5794.

64. Velasco, M. A.; Narváez-Tovar, C. A.; Garzón-Alvarado, D. A., Design, materials, and mechanobiology of biodegradable scaffolds for bone tissue engineering. *BioMed research international* **2015,** *2015*.

65. Jammalamadaka, U.; Tappa, K., Recent advances in biomaterials for 3D printing and tissue engineering. *Journal of functional biomaterials* **2018,** *9* (1), 22.

66. Sabir, M. I.; Xu, X.; Li, L., A review on biodegradable polymeric materials for bone tissue engineering applications. *Journal of materials science* **2009,** *44* (21), 5713-5724.

67. Becker, M.; Dean, H.; Yuanyuan, L., Well-defined degradable poly (propylene fumarate) polymers and scalable methods for the synthesis thereof. Google Patents: 2017.

68. Middleton, J. C.; Tipton, A. J., Synthetic biodegradable polymers as orthopedic devices. *Biomaterials* **2000,** *21* (23), 2335-2346.

69. Stevens, M. M., Biomaterials for bone tissue engineering. *Materials today* **2008,** *11* (5), 18-25.

70. Farah, S.; Anderson, D. G.; Langer, R., Physical and mechanical properties of PLA, and their functions in widespread applications—A comprehensive review. *Advanced drug delivery reviews* **2016,** *107*, 367-392.

71. Maitz, M. F., Applications of synthetic polymers in clinical medicine. *Biosurface and Biotribology* **2015,** *1* (3), 161-176.

72. Lee, B. K.; Yun, Y.; Park, K., PLA micro-and nano-particles. *Advanced drug delivery reviews* **2016,** *107*, 176-191.

73. Martin, I.; Wendt, D.; Heberer, M., The role of bioreactors in tissue engineering. *Trends in biotechnology* **2004,** *22* (2), 80-86.

74. Sinha, V.; Sharma, S.; Kaur, M.; Sarwal, A., Current polyesteric systems for advanced drug delivery. In *Nanoarchitectonics for Smart Delivery and Drug Targeting*, Matthew Deans The Boulevard, Langford Lane, Kidlington, Oxford, OX5 1GB …: 2016; pp 143-168.

75. Couet, F.; Rajan, N.; Mantovani, D., Macromolecular biomaterials for scaffold-based vascular tissue engineering. *Macromolecular bioscience* **2007,** *7* (5), 701-718.

76. Maurus, P. B.; Kaeding, C. C., Bioabsorbable implant material review. *Operative Techniques in Sports Medicine* **2004,** *12* (3), 158-160.

77. Cameron, R.; Kamvari-Moghaddam, A., Synthetic bioresorbable polymers. In *Degradation rate of bioresorbable materials*, Elsevier: 2008; pp 43-66.

78. Giannoudis, P. V.; Dinopoulos, H. T., Autologous bone graft: when shall we add growth factors? *Orthopedic Clinics* **2010,** *41* (1), 85-94.

79. Li, R. H.; Wozney, J. M., Delivering on the promise of bone morphogenetic proteins. *Trends in biotechnology* **2001,** *19* (7), 255-265.

80. Bergsma, J. E.; De Bruijn, W.; Rozema, F.; Bos, R.; Boering, G., Late degradation tissue response to poly (L-lactide) bone plates and screws. *Biomaterials* **1995,** *16* (1), 25-31.

81. Wu, Y.; Wong, Y. S.; Fuh, J. Y. H., Degradation behaviors of geometric cues and mechanical properties in a 3D scaffold for tendon repair. *Journal of Biomedical Materials Research Part A* **2017,** *105* (4), 1138-1149.

82. Sanderson, J. E., Bone replacement and repair putty material from unsaturated polyester resin and vinyl pyrrolidone. Google Patents: 1988.

83. Wang, S.; Kempen, D. H.; Simha, N. K.; Lewis, J. L.; Windebank, A. J.; Yaszemski, M. J.; Lu, L., Photo-cross-linked hybrid polymer networks consisting of poly (propylene fumarate) and poly (caprolactone fumarate): controlled physical properties and regulated bone and nerve cell responses. *Biomacromolecules* **2008,** *9* (4), 1229-1241.

84. Yaszemski, M. J.; Mikos, A. G.; Payne, R. G.; Hayes, W. C., Biodegradable polymer composites for temporary replacement of trabecular bone: The effect of polymer molecular weight on composite strength and modulus. *MRS Online Proceedings Library Archive* **1994**

331.

85. Bracaglia, L. G.; Yu, L.; Hibino, N.; Fisher, J. P., Reinforced pericardium as a hybrid material for cardiovascular applications. *Tissue Engineering Part A* **2014,** *20* (21-22), 2807-2816.

86. Chifiriuc, M. C.; Ficai, A.; Grumezescu, A. M.; Ditu, L.-M.; Popa, M.; Iordache, C.; Holban, A. M.; Beresteanu, Ş. V. G.; Grigore, R.; Lazar, V., Soft tissue engineering and microbial infections: Challenges and perspectives. In *Nanobiomaterials in Soft Tissue Engineering*, Elsevier: 2016; pp 1-29.

87. Liao, E.; Yaszemski, M.; Krebsbach, P.; Hollister, S., Tissue-engineered cartilage constructs using composite hyaluronic acid/collagen I hydrogels and designed poly (propylene fumarate) scaffolds. *Tissue engineering* **2007,** *13* (3), 537-550.

88. Barenghi, R.; Beke, S.; Romano, I.; Gavazzo, P.; Farkas, B.; Vassalli, M.; Brandi, F.; Scaglione, S., Elastin-coated biodegradable photopolymer scaffolds for tissue engineering applications. *BioMed research international* **2014,** *2014*.

89. Gerhart, T. N.; Hayes, W. C., Bioerodable implant composition. Google Patents: 1989.

90. DiCiccio, A. M.; Coates, G. W., Ring-opening copolymerization of maleic anhydride with epoxides: a chain-growth approach to unsaturated polyesters. *Journal of the American Chemical Society* **2011,** *133* (28), 10724-10727.

91. Gerhart, T.; Roux, R.; Horowitz, G.; Miller, R.; Hanff, P.; Hayes, W., Antibiotic release from an experimental biodegradable bone cement. *Journal of orthopaedic research* **1988,** *6* (4), 585-592.

92. Díez-Pascual, A. M.; Díez-Vicente, A. L., Magnetic Fe3O4@ poly (propylene fumarate-co-ethylene glycol) core–shell biomaterials. *RSC Advances* **2017,** *7* (17), 10221-10234.

93. Kasper, F. K.; Tanahashi, K.; Fisher, J. P.; Mikos, A. G., Synthesis of poly (propylene fumarate). *Nature protocols* **2009,** *4* (4), 518.

94. Fisher, J. P.; Vehof, J. W.; Dean, D.; van der Waerden, J. P. C.; Holland, T. A.; Mikos, A. G.; Jansen, J. A., Soft and hard tissue response to photocrosslinked poly (propylene fumarate) scaffolds in a rabbit model. *Journal of Biomedical Materials Research: An Official Journal of The Society for Biomaterials, The Japanese Society for Biomaterials, and The Australian Society for Biomaterials and the Korean Society for Biomaterials* **2002,** *59* (3), 547-556.

95. Wilson, J. A.; Luong, D.; Kleinfehn, A. P.; Sallam, S.; Wesdemiotis, C.; Becker, M. L., Magnesium catalyzed polymerization of end functionalized poly (propylene maleate) and poly (propylene fumarate) for 3D printing of bioactive scaffolds. *Journal of the American Chemical Society* **2018,** *140* (1), 277-284.

96. Fisher, J. P.; Dean, D.; Mikos, A. G., Photocrosslinking characteristics and mechanical properties of diethyl fumarate/poly (propylene fumarate) biomaterials. *Biomaterials* **2002,** *23* (22), 4333-4343.

97. Yaszemski, M. J.; Payne, R. G.; Hayes, W. C.; Langer, R.; Mikos, A. G., In vitro degradation of a poly (propylene fumarate)-based composite material. *Biomaterials* **1996,** *17* (22), 2127-2130.

98. Goldstein, S. A.; Wilson, D. L.; Sonstegard, D. A.; Matthews, L. S., The mechanical properties of human tibial trabecular bone as a function of metaphyseal location. *Journal of biomechanics* **1983,** *16* (12), 965-969.

99. Allo, B. A.; Costa, D. O.; Dixon, S. J.; Mequanint, K.; Rizkalla, A. S., Bioactive and biodegradable nanocomposites and hybrid biomaterials for bone regeneration. *Journal of functional biomaterials* **2012,** *3* (2), 432-463.

100. Bose, S.; Roy, M.; Bandyopadhyay, A., Recent advances in bone tissue engineering scaffolds. *Trends in biotechnology* **2012,** *30* (10), 546-554.

101. Crane, G. M.; Ishaug, S. L.; Mikos, A. G., Bone tissue engineering. Nature Publishing Group: 1995.

102. Kim, S.-S.; Park, M. S.; Jeon, O.; Choi, C. Y.; Kim, B.-S., Poly (lactide-co-glycolide)/hydroxyapatite composite scaffolds for bone tissue engineering. *Biomaterials* **2006,** *27* (8), 1399-1409.

103. Kempen, D. H.; Lu, L.; Hefferan, T. E.; Creemers, L. B.; Maran, A.; Classic, K. L.; Dhert, W. J.; Yaszemski, M. J., Retention of in vitro and in vivo BMP-2 bioactivities in sustained delivery vehicles for bone tissue engineering. *Biomaterials* **2008,** *29* (22), 3245-3252.

104. Shin, J. H.; Lee, J. W.; Jung, J. H.; Cho, D.-W.; Lim, G., Evaluation of cell proliferation and differentiation on a poly (propylene fumarate) 3D scaffold treated with functional peptides. *Journal of Materials Science* **2011,** *46* (15), 5282-5287.

105. Lee, J. W.; Jung, J. H.; Kim, D. S.; Lim, G.; Cho, D.-W., Estimation of cell proliferation by various peptide coating at the PPF/DEF 3D scaffold. *Microelectronic Engineering* **2009,** *86* (4-6), 1451-1454.

106. Lan, P. X.; Lee, J. W.; Seol, Y.-J.; Cho, D.-W., Development of 3D PPF/DEF scaffolds using micro-stereolithography and surface modification. *Journal of Materials Science: Materials in Medicine* **2009,** *20* (1), 271-279.

107. Wilson, J. A.; Luong, D.; Kleinfehn, A. P.; Sallam, S.; Wesdemiotis, C.; Becker, M. L., Magnesium catalyzed polymerization of end functionalized poly (propylene maleate) and poly (propylene fumarate) for 3d printing of bioactive scaffolds. *Journal of the American Chemical Society* **2017,** *140* (1), 277-284.

108. Chu, T.; Sargent, P.; Warden, S. J.; Turner, C. H.; Stewart, R. L., Preliminary evaluation of a load-bearing BMP-2 carrier for segmental defect regeneration. *Biomedical sciences instrumentation* **2006,** *42*, 42-47.

109. Seol, Y.-J.; Kang, T.-Y.; Cho, D.-W., Solid freeform fabrication technology applied to tissue engineering with various biomaterials. *Soft Matter* **2012,** *8* (6), 1730-1735.

110. Ueda, H.; Hacker, M.; Haesslein, A.; Jo, S.; Ammon, D.; Borazjani, R.; Kunzler, J.; Salamone, J.; Mikos, A., Injectable, in situ forming poly (propylene fumarate)-based ocular drug delivery systems. *Journal of Biomedical Materials Research Part A: An Official Journal of The Society for Biomaterials, The Japanese Society for Biomaterials,*

and The Australian Society for Biomaterials and the Korean Society for Biomaterials **2007,** *83* (3), 656-666.

111. Kempen, D. H.; Lu, L.; Zhu, X.; Kim, C.; Jabbari, E.; Dhert, W. J.; Currier, B. L.; Yaszemski, M. J., Development of biodegradable poly (propylene fumarate)/poly (lactic-co-glycolic acid) blend microspheres. II. Controlled drug release and microsphere degradation. *Journal of Biomedical Materials Research Part A: An Official Journal of The Society for Biomaterials, The Japanese Society for Biomaterials, and The Australian Society for Biomaterials and the Korean Society for Biomaterials* **2004,** *70* (2), 293-302.

112. Haesslein, A.; Hacker, M.; Mikos, A., Effect of macromer molecular weight on in vitro ophthalmic drug release from photo-crosslinked matrices. *Acta biomaterialia* **2008,** *4* (1), 1-10.

113. Trachtenberg, J. E.; Placone, J. K.; Smith, B. T.; Fisher, J. P.; Mikos, A. G., Extrusion-based 3D printing of poly (propylene fumarate) scaffolds with hydroxyapatite gradients. *Journal of Biomaterials science, Polymer edition* **2017,** *28* (6), 532-554.

114. Trachtenberg, J. E.; Placone, J. K.; Smith, B. T.; Piard, C. M.; Santoro, M.; Scott, D. W.; Fisher, J. P.; Mikos, A. G., Extrusion-based 3D printing of poly (propylene fumarate) in a full-factorial design. *ACS Biomaterials Science & Engineering* **2016,** *2* (10), 1771-1780.

115. Wang, M. O.; Vorwald, C. E.; Dreher, M. L.; Mott, E. J.; Cheng, M. H.; Cinar, A.; Mehdizadeh, H.; Somo, S.; Dean, D.; Brey, E. M.; Fisher, J. P., Evaluating 3D-Printed Biomaterials as Scaffolds for Vascularized Bone Tissue Engineering. *Adv Mater* **2015,** *27* (1), 138-144.

116. Peltola, S. M.; Melchels, F. P.; Grijpma, D. W.; Kellomäki, M., A review of rapid prototyping techniques for tissue engineering purposes. *Annals of medicine* **2008,** *40* (4), 268-280.

117. Lee, J. W.; Kim, J. Y.; Cho, D.-W., Solid free-form fabrication technology and its application to bone tissue engineering. *International journal of stem cells* **2010,** *3* (2), 85.

118. Melchels, F. P.; Feijen, J.; Grijpma, D. W., A review on stereolithography and its applications in biomedical engineering. *Biomaterials* **2010,** *31* (24), 6121-6130.

119. Shi, X.; Henslee, A.; Yoon, D.; Kasper, F. K.; Mikos, A. G., 18 Poly (Propylene Fumarate). *An Introduction to Biomaterials* **2011**, 317.

120. Nguyen, L. H.; Annabi, N.; Nikkhah, M.; Bae, H.; Binan, L.; Park, S.; Kang, Y.; Yang, Y.; Khademhosseini, A., Vascularized bone tissue engineering: approaches for potential improvement. *Tissue Engineering Part B: Reviews* **2012,** *18* (5), 363-382.

121. Martinez, P. R.; Goyanes, A.; Basit, A. W.; Gaisford, S., Fabrication of drug-loaded hydrogels with stereolithographic 3D printing. *International journal of pharmaceutics* **2017,** *532* (1), 313-317.

122. Cooke, M. N.; Fisher, J. P.; Dean, D.; Rimnac, C.; Mikos, A. G., Use of stereolithography to manufacture critical-sized 3D biodegradable scaffolds for bone ingrowth. *Journal of Biomedical Materials Research Part B: Applied Biomaterials: An Official Journal of The Society for Biomaterials, The Japanese Society for Biomaterials, and The Australian Society for Biomaterials and the Korean Society for Biomaterials* **2003,** *64* (2), 65-69.

123. Edwards, J.; Rogers, T., The accuracy and applicability of 3D modeling and printing blunt force cranial injuries. *Journal of forensic sciences* **2018,** *63* (3), 683-691.

124. Kost, J.; Wiseman, D.; Domb, A. J., *Handbook of biodegradable polymers*. CRC press: 1998.

125. Takenouchi, S.; Takasu, A.; Inai, Y.; Hirabayashi, T., Effects of Geometrical Difference of Unsaturated Aliphatic Polyesters on Their Biodegradability II. Isomerization of Poly (maleic anhydride-co-propylene oxide) inthe Presence of Morpholine. *Polymer journal* **2002,** *34* (1), 36.

126. Lee, J. W.; Lan, P. X.; Kim, B.; Lim, G.; Cho, D.-W., 3D scaffold fabrication with PPF/DEF using micro-stereolithography. *Microelectronic Engineering* **2007,** *84* (5-8), 1702-1705.

127. Domb, A. J.; Laurencin, C. T.; Israeli, O.; Gerhart, T. N.; Langer, R., The formation of propylene fumarate oligomers for use in bioerodible bone cement composites. *Journal of Polymer Science Part A: Polymer Chemistry* **1990,** *28* (5), 973-985.

128. Kharas, G. B.; Kamenetsky, M.; Simantirakis, J.; Beinlich, K. C.; Rizzo, A. M. T.; Caywood, G. A.; Watson, K., Synthesis and characterization of fumarate-based polyesters for use in bioresorbable bone cement composites. *Journal of applied polymer science* **1997,** *66* (6), 1123-1137.

129. Ordelt, Z.; Novak, V.; Krátký, B., Über die Umkehrbarkeit der Diolenaddition an die olefinische Doppelbindung der Äthylen-1, 2-dicarbonsäuren bei der Polykondensation in der Schmelze. *Collection of Czechoslovak Chemical Communications* **1968,** *33* (2), 405-415.

130. Shung, A. K.; Timmer, M. D.; Jo, S.; Engel, P. S.; Mikos, A. G., Kinetics of poly (propylene fumarate) synthesis by step polymerization of diethyl fumarate and propylene glycol using zinc chloride as a catalyst. *Journal of Biomaterials Science, Polymer Edition* **2002,** *13* (1), 95-108.

131. Hua, Z.; Qi, G.; Chen, S., Ring-opening copolymerization of maleic anhydride with propylene oxide by double-metal cyanide. *Journal of applied polymer science* **2004,** *93* (4), 1788-1792.

132. Longo, J. M.; Sanford, M. J.; Coates, G. W., Ring-opening copolymerization of epoxides and cyclic anhydrides with discrete metal complexes: structure–property relationships. *Chemical reviews* **2016,** *116* (24), 15167-15197.

133. Ji, H.-Y.; Wang, B.; Pan, L.; Li, Y.-S., Lewis pairs for ring-opening alternating copolymerization of cyclic anhydrides and epoxides. *Green Chemistry* **2018,** *20* (3), 641-648.

134. Odian, G., *Principles of polymerization*. John Wiley & Sons: 2004.

135. Toyoda, N.; Yoshida, M.; Otsu, T., Polymers from 1, 2-Disubstituted Ethylenic Monomers VI. Monomer-isomerization Radical Polymerization of Diethyl Maleate. *Polymer Journal* **1983,** *15* (4), 255.

136. Gresser, J. D.; Hsu, S. H.; Nagaoka, H.; Lyons, C. M.; Nieratko, D. P.; Wise, D. L.; Barabino, G. A.; Trantolo, D. J., Analysis of a vinyl pyrrolidone/poly (propylene fumarate) resorbable bone cement. *Journal of biomedical materials research* **1995,** *29* (10), 1241-1247.

137. Wang, S.; Lu, L.; Yaszemski, M. J., Bone-tissue-engineering material poly (propylene fumarate): correlation between molecular weight, chain dimensions, and physical properties. *Biomacromolecules* **2006,** *7* (6), 1976-1982.

138. Sallam, S.; Luo, Y.; Becker, M. L.; Wesdemiotis, C., Multidimensional mass spectrometry characterization of isomeric biodegradable polyesters. *European Journal of Mass Spectrometry* **2017,** *23* (6), 402-410.

139. Atala, A.; Yoo, J., *Essentials of 3D Biofabrication and Translation*. 1st ed.; Waltham, MA: Academic Press, 2015.

140. Dean, D.; Min, K.-J.; Bond, A., Computer aided design of large-format prefabricated cranial plates. *Journal of Craniofacial Surgery* **2003,** *14* (6), 819-832.

141. Wallace, J.; Wang, M. O.; Thompson, P.; Busso, M.; Belle, V.; Mammoser, N.; Kim, K.; Fisher, J. P.; Siblani, A.; Xu, Y.; Welter, J. F.; Lennon, D. P.; Sun, J.; Caplan, A. I.; Dean, D., Validating continuous digital light processing (cDLP) additive manufacturing accuracy and tissue engineering utility of a dye-initiator package. *Biofabrication* **2014,** *6* (1), 015003.

142. Childers, E. P.; Wang, M. O.; Becker, M. L.; Fisher, J. P.; Dean, D., 3D printing of resorbable poly(propylene fumarate) tissue engineering scaffolds. *MRS Bulletin* **2015,** *40* (02), 119-126.

143. Ronca, A.; Ambrosio, L.; Grijpma, D. W., Design of porous three-dimensional PDLLA/nano-hap composite scaffolds using stereolithography. *Journal of applied biomaterials & functional materials* **2011,** *10* (3), 249-258.

144. Skoog, S. A.; Goering, P. L.; Narayan, R. J., Stereolithography in tissue engineering. *Journal of Materials Science: Materials in Medicine* **2014,** *25* (3), 845-856.

145. Cooke, M. N.; Fisher, J. P.; Dean, D.; Rimnac, C.; Mikos, A. G., Use of stereolithography to manufacture critical-sized 3D biodegradable scaffolds for bone ingrowth. *Journal of Biomedical Materials Research Part B: Applied Biomaterials* **2003,** *64* (2), 65-69.

146. Muhammad Iqbal Sabir, X. X., Li Li, A review on biodegradable polymeric materials for bone tissue engineering applications. *J Mater Sci* **2009,** *44*, 5713-5724.

147. Yaszemski, M. J.; Payne, R. G.; Mikos, A. G., Poly (propylene fumarate). Google Patents: 1998.

148. Barenghi, R.; Beke, S.; Romano, I.; Gavazzo, P.; Farkas, B.; Vassalli, M.; Brandi, F.; Scaglione, S., Elastin-coated biodegradable photopolymer scaffolds for tissue engineering applications. *BioMed research international* **2014,** *2014*, 624645.

149. Lee, J. W.; Kang, K. S.; Lee, S. H.; Kim, J.-Y.; Lee, B.-K.; Cho, D.-W., Bone regeneration using a microstereolithography-produced customized poly(propylene fumarate)/diethyl fumarate photopolymer 3D scaffold incorporating BMP-2 loaded PLGA microspheres. *Biomaterials* **2011,** *32* (3), 744-752.

150. Temenoff, J. S.; Mikos, A. G., Injectable biodegradable materials for orthopedic tissue engineering. *Biomaterials* **2000,** *21* (23), 2405-2412.

151. Fisher, J. P.; Dean, D.; Mikos, A. G., Photocrosslinking characteristics and mechanical properties of diethyl fumarate/poly(propylene fumarate) biomaterials. *Biomaterials* **2002,** *23* (22), 4333-4343.

152. Kim, K.; Dean, D.; Wallace, J.; Breithaupt, R.; Mikos, A. G.; Fisher, J. P., The influence of stereolithographic scaffold architecture and composition on osteogenic signal expression with rat bone marrow stromal cells. *Biomaterials* **2011,** *32* (15), 3750-3763.

153. Payne, R. G.; McGonigle, J. S.; Yaszemski, M. J.; Yasko, A. W.; Mikos, A. G., Development of an injectable, in situ crosslinkable, degradable polymeric carrier for osteogenic cell populations. Part 2. Viability of encapsulated marrow stromal osteoblasts cultured on crosslinking poly(propylene fumarate). *Biomaterials* **2002,** *23* (22), 4373-4380.

154. Horch, R. A.; Shahid, N.; Mistry, A. S.; Timmer, M. D.; Mikos, A. G.; Barron, A. R., Nanoreinforcement of Poly(propylene fumarate)-Based Networks with Surface Modified Alumoxane Nanoparticles for Bone Tissue Engineering. *Biomacromolecules* **2004,** *5* (5), 1990-1998.

155. Hedberg, E. L.; Shih, C. K.; Lemoine, J. J.; Timmer, M. D.; K. Liebschner, M. A.; Jansen, J. A.; Mikos, A. G., In vitro degradation of porous poly(propylene fumarate)/poly(dl-lactic-co-glycolic acid) composite scaffolds. *Biomaterials* **2005,** *26* (16), 3215-3225.

156. Jo, S.; Engel, P. S.; Mikos, A. G., Synthesis of poly(ethylene glycol)-tethered poly(propylene fumarate) and its modification with GRGD peptide. *Polymer* **2000,** *41* (21), 7595-7604.

157. Domb, A. J. K., J.; Wiseman, D. M., *Handbook of Biodegradable Polymers*. Harwood Academic Publishers: 1997; p 87-97.

158. Choi, J.-W.; Wicker, R.; Lee, S.-H.; Choi, K.-H.; Ha, C.-S.; Chung, I., Fabrication of 3D biocompatible/biodegradable micro-scaffolds using dynamic mask projection microstereolithography. *Journal of Materials Processing Technology* **2009,** *209* (15–16), 5494-5503.

159. Pathiraja A. Gunatillake, R. A., Biodegradable Synthetic Polymers for Tissue Engineering. *European Cells and Materials* **2003,** *5*, 1-16.

160. Shrivastava, H. Y.; Ravikumar, T.; Shanmugasundaram, N.; Babu, M.; Nair, B. U., Cytotoxicity studies of chromium (III) complexes on human dermal fibroblasts. *Free Radical Biology and Medicine* **2005,** *38* (1), 58-69.

161. Figgitt, M.; Newson, R.; Leslie, I. J.; Fisher, J.; Ingham, E.; Case, C. P., The genotoxicity of physiological concentrations of chromium (Cr (III) and Cr (VI)) and cobalt (Co (II)): an in vitro study. *Mutation Research/Fundamental and Molecular Mechanisms of Mutagenesis* **2010,** *688* (1-2), 53-61.

162. Jérôme, C.; Lecomte, P., Recent advances in the synthesis of aliphatic polyesters by ring-opening polymerization. *Advanced drug delivery reviews* **2008,** *60* (9), 1056-1076.

163. Grillo, C. A.; Alvarez, F.; de Mele, M. A. F. L., Degradation of bioabsorbable Mg-based alloys: Assessment of the effects of insoluble corrosion products and joint effects of alloying components on mammalian cells. *Materials Science and Engineering: C* **2016,** *58*, 372-380.

164. Walker, J.; Dean, D., Modulating the gyroid surface for creating custom porous architectures in tissue engineering scaffolds. *Biofabrication* **in review**.

165. Wang, M. O.; Etheridge, J. M.; Thompson, J. A.; Vorwald, C. E.; Dean, D.; Fisher, J. P., Evaluation of the in vitro cytotoxicity of cross-linked biomaterials. *Biomacromolecules* **2013,** *14* (5), 1321-1329.

166. Fisher, J. P.; Holland, T. A.; Dean, D.; Mikos, A. G., Photoinitiated Cross-Linking of the Biodegradable Polyester Poly(propylene fumarate). Part II. In Vitro Degradation. *Biomacromolecules* **2003,** *4* (5), 1335-1342.

167. Stansbury, J. W.; Idacavage, M. J., 3D printing with polymers: Challenges among expanding options and opportunities. *Dental Materials* **2016,** *32* (1), 54-64.

168. Mandrycky, C.; Wang, Z.; Kim, K.; Kim, D.-H., 3D bioprinting for engineering complex tissues. *Biotechnology Advances* **2016,** *34* (4), 422-434.

169. Kang, H.-W.; Lee, S. J.; Ko, I. K.; Kengla, C.; Yoo, J. J.; Atala, A., A 3D bioprinting system to produce human-scale tissue constructs with structural integrity. *Nature biotechnology* **2016,** *34* (3), 312-319.

170. Chia, H. N.; Wu, B. M., Recent advances in 3D printing of biomaterials. *Journal of biological engineering* **2015,** *9* (1), 4.

171. Obregon, F.; Vaquette, C.; Ivanovski, S.; Hutmacher, D.; Bertassoni, L., Three-dimensional bioprinting for regenerative dentistry and craniofacial tissue engineering. *Journal of dental research* **2015,** *94* (9_suppl), 143S-152S.

172. Li, S.; Xu, Y.; Yu, J.; Becker, M. L., Enhanced osteogenic activity of poly (ester urea) scaffolds using facile post-3D printing peptide functionalization strategies. *Biomaterials* **2017,** *141*, 176-187.

173. Dean, D.; Wallace, J.; Siblani, A.; Wang, M. O.; Kim, K.; Mikos, A. G.; Fisher, J. P., Continuous digital light processing (cDLP): Highly accurate additive manufacturing of tissue engineered bone scaffolds. *Virtual physical prototyping* **2012,** *7* (1), 13-24.

174. Loh, Q. L.; Choong, C., Three-dimensional scaffolds for tissue engineering applications: role of porosity and pore size. *Tissue Engineering Part B: Reviews* **2013,** *19* (6), 485-502.

175. Ligon, S. C.; Liska, R.; Stampfl, J.; Gurr, M.; Mülhaupt, R., Polymers for 3D Printing and Customized Additive Manufacturing. *Chemical Reviews* **2017,** *117* (15), 10212.

176. Dean, D.; Mott, E.; Luo, X.; Busso, M.; Wang, M. O.; Vorwald, C.; Siblani, A.; Fisher, J. P., Multiple initiators and dyes for continuous Digital Light Processing (cDLP) additive manufacture of resorbable bone tissue engineering scaffolds: A new method and new material to fabricate resorbable scaffold for bone tissue engineering via continuous Digital Light Processing. *Virtual Physical Prototyping* **2014,** *9* (1), 3-9.

177. Yaszemski, M. J.; Payne, R. G.; Hayes, W. C.; Langer, R. S.; Aufdemorte, T. B.; Mikos, A. G., The ingrowth of new bone tissue and initial mechanical properties of a degrading polymeric composite scaffold. *Tissue engineering* **1995,** *1* (1), 41-52.

178. Yaszemski, M. J.; Payne, R. G.; Mikos, A. G., Poly (propylene fumarate). USA Pat. US5733951 A: Mar 31, 1998.

179. Wallace, J.; Wang, M. O.; Thompson, P.; Busso, M.; Belle, V.; Mammoser, N.; Kim, K.; Fisher, J. P.; Siblani, A.; Xu, Y., Validating continuous digital light processing (cDLP) additive manufacturing accuracy and tissue engineering utility of a dye-initiator package. *Biofabrication* **2014,** *6* (1), 015003.

180. Choi, J.; Kim, K.; Kim, T.; Liu, G.; Bar-Shir, A.; Hyeon, T.; McMahon, M. T.; Bulte, J. W.; Fisher, J. P.; Gilad, A. A., Multimodal imaging of sustained drug release

from 3-D poly(propylene fumarate)(PPF) scaffolds. *J. Controlled Release* **2011,** *156* (2), 239-245.

181. Seetharaman, G.; Kallar, A. R.; Vijayan, V. M.; Muthu, J.; Selvam, S., Design, preparation and characterization of pH-responsive prodrug micelles with hydrolyzable anhydride linkages for controlled drug delivery. *Journal of colloid interface science* **2017,** *492*, 61-72.

182. Dilla, R. A.; Motta, C. M.; Snyder, S. R.; Wilson, J. A.; Wesdemiotis, C.; Becker, M. L., Synthesis and 3D Printing of PEG–Poly (propylene fumarate) Diblock and Triblock Copolymer Hydrogels. *ACS Macro Letters* **2018,** *7* (10), 1254-1260.

183. Fisher, J. P.; Jo, S.; Mikos, A. G.; Reddi, A. H., Thermoreversible hydrogel scaffolds for articular cartilage engineering. *Journal of Biomedical Materials Research Part A* **2004,** *71* (2), 268-274.

184. Dean, D.; Wolfe, M. S.; Ahmad, Y.; Totonchi, A.; Chen, J. E.-K.; Fisher, J. P.; Cooke, M. N.; Rimnac, C. M.; Lennon, D. P.; Caplan, A. I., Effect of transforming growth factor β2 on marrow-infused foam poly (propylene fumarate) tissue-engineered constructs for the repair of critical-size cranial defects in rabbits. *Tissue engineering* **2005,** *11* (5-6), 923-939.

185. Lee, J. W.; Kang, K. S.; Lee, S. H.; Kim, J.-Y.; Lee, B.-K.; Cho, D.-W., Bone regeneration using a microstereolithography-produced customized poly (propylene fumarate)/diethyl fumarate photopolymer 3D scaffold incorporating BMP-2 loaded PLGA microspheres. *Biomaterials* **2011,** *32* (3), 744-752.

186. Olthof, M. G.; Kempen, D. H.; Herrick, J. L.; Yaszemski, M. J.; Dhert, W. J.; Lu, L., Effect of different sustained bone morphogenetic protein-2 release kinetics on bone formation in poly (propylene fumarate) scaffolds. *Journal of Biomedical Materials Research Part B: Applied Biomaterials* **2018,** *106* (2), 477-487.

187. Jansen, J.; Melchels, F. P.; Grijpma, D. W.; Feijen, J., Fumaric acid monoethyl ester-functionalized poly (D, L-lactide)/N-vinyl-2-pyrrolidone resins for the preparation of tissue engineering scaffolds by stereolithography. *Biomacromolecules* **2009,** *10* (2), 214-220.

188. Mu, Q.; Wang, L.; Dunn, C. K.; Kuang, X.; Duan, F.; Zhang, Z.; Qi, H. J.; Wang, T., Digital light processing 3D printing of conductive complex structures. *Additive Manufacturing* **2017,** *18*, 74-83.

189. Gonzalez, G.; Chiappone, A.; Roppolo, I.; Fantino, E.; Bertana, V.; Perrucci, F.; Scaltrito, L.; Pirri, F.; Sangermano, M., Development of 3D printable formulations containing CNT with enhanced electrical properties. *Polymer* **2017,** *109*, 246-253.

190. He, S.; Yaszemski, M. J.; Yasko, A. W.; Engel, P. S.; Mikos, A. G., Injectable biodegradable polymer composites based on poly (propylene fumarate) crosslinked with poly (ethylene glycol)-dimethacrylate. *Biomaterials* **2000,** *21* (23), 2389-2394.

191. He, S.; Timmer, M.; Yaszemski, M. J.; Yasko, A.; Engel, P.; Mikos, A., Synthesis of biodegradable poly (propylene fumarate) networks with poly (propylene fumarate)–diacrylate macromers as crosslinking agents and characterization of their degradation products. *Polymer* **2001,** *42* (3), 1251-1260.

192. Wang, S.; Kempen, D. H.; Simha, N. K.; Lewis, J. L.; Windebank, A. J.; Yaszemski, M. J.; Lu, L., Photo-crosslinked hybrid polymer networks consisting of poly (propylene fumarate)(PPF) and poly (caprolactone fumarate)(PCLF): controlled physical properties and regulated bone and nerve cell responses. *Biomacromolecules* **2008,** *9* (4), 1229.

193. Lee, K.-W.; Wang, S.; Yaszemski, M. J.; Lu, L., Physical properties and cellular responses to crosslinkable poly (propylene fumarate)/hydroxyapatite nanocomposites. *Biomaterials* **2008,** *29* (19), 2839-2848.

194. Suwandi, J.; Toes, R.; Nikolic, T.; Roep, B., Inducing tissue specific tolerance in autoimmune disease with tolerogenic dendritic cells. *Clin Exp Rheumatol* **2015,** *33* (4 Suppl 92), 97-103.

195. Andrade, E. N. D. C.; Dodd, C., The effect of an electric field on the viscosity of liquids. *Proc. R. Soc. Lond. A* **1946,** *187* (1010), 296-337.

196. Duhne, C., Viscosity-temperature correlations for liquids. *Chemical Engineering* **1979,** *86* (15), 83-91.

197. Andrade, E. d. C., LVIII. A theory of the viscosity of liquids.—Part II. *The London, Edinburgh, and Dublin Philosophical Magazine and Journal of Science* **1934,** *17* (113), 698-732.

198. Jacobs, P. F., *Rapid prototyping & manufacturing: fundamentals of stereolithography*. Society of Manufacturing Engineers: Dearborn, 1992.

199. Huang, Q.; Nouri, H.; Xu, K.; Chen, Y.; Sosina, S.; Dasgupta, T., Statistical predictive modeling and compensation of geometric deviations of three-dimensional printed products. *Journal of Manufacturing Science and Engineering* **2014,** *136* (6), 061008.

200. Huang, Q.; Zhang, J.; Sabbaghi, A.; Dasgupta, T., Optimal offline compensation of shape shrinkage for three-dimensional printing processes. *IIE Transactions* **2015,** *47* (5), 431-441.

201. Athanasiou, K.; Zhu, C.-F.; Lanctot, D.; Agrawal, C.; Wang, X., Fundamentals of biomechanics in tissue engineering of bone. *Tissue engineering* **2000,** *6* (4), 361-381.

202. Sikavitsas, V. I.; Temenoff, J. S.; Mikos, A. G., Biomaterials and bone mechanotransduction. *Biomaterials* **2001,** *22* (19), 2581-2593.

203. Hannink, G.; Arts, J. C., Bioresorbability, porosity and mechanical strength of bone substitutes: what is optimal for bone regeneration? *Injury* **2011,** *42*, S22-S25.

204. Curtis, A.; Clark, P., The effects of topographic and mechanical properties of materials on cell behavior. *Crit. Rev. Biocompat* **1990,** *5*, 343-362.

205. Murphy, W. L.; McDevitt, T. C.; Engler, A. J., Materials as stem cell regulators. *Nature materials* **2014,** *13* (6), 547.

206. Bajaj, P.; Schweller, R. M.; Khademhosseini, A.; West, J. L.; Bashir, R., 3D biofabrication strategies for tissue engineering and regenerative medicine. *Annual review of biomedical engineering* **2014,** *16*, 247-276.

207. Hutmacher, D. W., Scaffolds in tissue engineering bone and cartilage. In *The Biomaterials: Silver Jubilee Compendium*, Elsevier: 2006; pp 175-189.

208. Sears, N. A.; Seshadri, D. R.; Dhavalikar, P. S.; Cosgriff-Hernandez, E., A review of three-dimensional printing in tissue engineering. *Tissue Engineering Part B: Reviews* **2016,** *22* (4), 298-310.

209. Pitt, G.; Gratzl, M.; Kimmel, G.; Surles, J.; Sohindler, A., Aliphatic polyesters II. The degradation of poly (DL-lactide), poly (ε-caprolactone), and their copolymers in vivo. *Biomaterials* **1981,** *2* (4), 215-220.

210. Nair, L. S.; Laurencin, C. T., Biodegradable polymers as biomaterials. *Progress in polymer science* **2007,** *32* (8-9), 762-798.

211. Guégain, E.; Michel, J.-P.; Boissenot, T.; Nicolas, J., Tunable Degradation of Copolymers Prepared by Nitroxide-Mediated Radical Ring-Opening Polymerization and Point-by-Point Comparison with Traditional Polyesters. *Macromolecules* **2018,** *51* (3), 724-736.

212. Sirrine, J. M.; Pekkanen, A. M.; Nelson, A. M.; Chartrain, N. A.; Williams, C. B.; Long, T. E., 3D-printable biodegradable polyester tissue scaffolds for cell adhesion. *Australian Journal of Chemistry* **2015,** *68* (9), 1409-1414.

213. Gonçalves, F.; Fonseca, A.; Domingos, M.; Gloria, A.; Serra, A.; Coelho, J., The potential of unsaturated polyesters in biomedicine and tissue engineering: Synthesis, structure-properties relationships and additive manufacturing. *Progress in Polymer Science* **2017,** *68*, 1-34.

214. Delplace, V.; Nicolas, J., Degradable vinyl polymers for biomedical applications. *Nature chemistry* **2015,** *7* (10), 771.

215. Agarwal, S., Chemistry, chances and limitations of the radical ring-opening polymerization of cyclic ketene acetals for the synthesis of degradable polyesters. *Polymer Chemistry* **2010,** *1* (7), 953-964.

216. Cutright, D. E.; Beasley III, J. D.; Perez, B., Histologic comparison of polylactic and polyglycolic acid sutures. *Oral Surgery, Oral Medicine, Oral Pathology* **1971,** *32* (1), 165-173.

217. Balog, T. P.; Min, K. S.; Rumley, J. C.; Wilson, D. J.; Arrington, E. D., Arthroscopic anatomic coracoclavicular ligament repair using a 6-strand polyester suture tape and cortical button construct. *Arthroscopy techniques* **2015,** *4* (6), e757-e761.

218. Le Fer, G. l.; Le Cœur, C. m.; Guigner, J.-M.; Amiel, C.; Volet, G. l., Biocompatible Soft Nanoparticles with Multiple Morphologies Obtained from Nanoprecipitation of Amphiphilic Graft Copolymers in a Backbone-Selective Solvent. *Langmuir* **2017,** *33* (11), 2849-2860.

219. Guillaume, O.; Garric, X.; Lavigne, J.-P.; Van Den Berghe, H.; Coudane, J., Multilayer, degradable coating as a carrier for the sustained release of antibiotics: preparation and antimicrobial efficacy in vitro. *Journal of controlled release* **2012,** *162* (3), 492-501.

220. Cho, D. Y.; Cho, H.; Kwon, K.; Yu, M.; Lee, E.; Huh, K. M.; Lee, D. H.; Kang, H. C., Triphenylphosphonium-conjugated poly (ε-caprolactone)-based self-assembled nanostructures as nanosized drugs and drug delivery carriers for mitochondria-targeting synergistic anticancer drug delivery. *Advanced Functional Materials* **2015,** *25* (34), 5479-5491.

221. Guégain, E.; Tran, J.; Deguettes, Q.; Nicolas, J., Degradable polymer prodrugs with adjustable activity from drug-initiated radical ring-opening copolymerization. *Chemical science* **2018,** *9* (43), 8291-8306.

222. Nottelet, B.; Darcos, V.; Coudane, J., Aliphatic polyesters for medical imaging and theranostic applications. *European Journal of Pharmaceutics and Biopharmaceutics* **2015,** *97*, 350-370.

223. Mackiewicz, N.; Nicolas, J.; Handké, N. g.; Noiray, M.; Mougin, J.; Daveu, C.; Lakkireddy, H. R.; Bazile, D.; Couvreur, P., Precise engineering of multifunctional PEGylated polyester nanoparticles for cancer cell targeting and imaging. *Chemistry of Materials* **2014,** *26* (5), 1834-1847.

224. Samuel, R.; Girard, E.; Chagnon, G.; Dejean, S.; Favier, D.; Coudane, J.; Nottelet, B., Radiopaque poly (ε-caprolactone) as additive for X-ray imaging of temporary implantable medical devices. *Rsc Advances* **2015,** *5* (102), 84125-84133.

225. Hendrikson, W. J.; Zeng, X.; Rouwkema, J.; van Blitterswijk, C. A.; van der Heide, E.; Moroni, L., Biological and Tribological assessment of poly (ethylene oxide

terephthalate)/poly (butylene terephthalate), polycaprolactone, and poly (L\DL) lactic acid plotted scaffolds for skeletal tissue regeneration. *Advanced healthcare materials* **2016,** *5* (2), 232-243.

226. Ye, H.; Zhang, K.; Kai, D.; Li, Z.; Loh, X. J., Polyester elastomers for soft tissue engineering. *Chemical Society Reviews* **2018**.

227. Wang, M. O.; Vorwald, C. E.; Dreher, M. L.; Mott, E. J.; Cheng, M. H.; Cinar, A.; Mehdizadeh, H.; Somo, S.; Dean, D.; Brey, E. M., Evaluating 3D-Printed biomaterials as scaffolds for vascularized bone tissue engineering. *Adv Mater* **2015,** *27* (1), 138-144.

228. Lee, K.-W.; Wang, S.; Fox, B. C.; Ritman, E. L.; Yaszemski, M. J.; Lu, L., Poly (propylene fumarate) bone tissue engineering scaffold fabrication using stereolithography: effects of resin formulations and laser parameters. *Biomacromolecules* **2007,** *8* (4), 1077-1084.

229. He, S.; Timmer, M.; Yaszemski, M.; Yasko, A.; Engel, P.; Mikos, A., Synthesis of biodegradable poly (propylene fumarate) networks with poly (propylene fumarate)–diacrylate macromers as crosslinking agents and characterization of their degradation products. *Polymer* **2001,** *42* (3), 1251-1260.

230. Petersen, S. R.; Wilson, J. A.; Becker, M. L., Versatile Ring-Opening Copolymerization and Postprinting Functionalization of Lactone and Poly (propylene fumarate) Block Copolymers: Resorbable Building Blocks for Additive Manufacturing. *Macromolecules* **2018,** *51* (16), 6202-6208.

231. Melchels, F. P.; Feijen, J.; Grijpma, D. W., A poly (D, L-lactide) resin for the preparation of tissue engineering scaffolds by stereolithography. *Biomaterials* **2009,** *30* (23-24), 3801-3809.

232. Schüller-Ravoo, S.; Teixeira, S. M.; Feijen, J.; Grijpma, D. W.; Poot, A. A., Flexible and Elastic Scaffolds for Cartilage Tissue Engineering Prepared by Stereolithography Using Poly (trimethylene carbonate)-B ased Resins. *Macromolecular bioscience* **2013,** *13* (12), 1711-1719.

233. Mondschein, R. J.; Kanitkar, A.; Williams, C. B.; Verbridge, S. S.; Long, T. E., Polymer structure-property requirements for stereolithographic 3D printing of soft tissue engineering scaffolds. *Biomaterials* **2017,** *140*, 170-188.

234. Luo, Y.; Le Fer, G.; Dean, D.; Becker, M. L., 3D Printing of Poly(propylene fumarate) Oligomers: Evaluation of Resin Viscosity, Printing Characteristics and Mechanical Properties. *Biomacromolecules* **2019**.

235. Aoki, D.; Uchida, S.; Takata, T., Star/linear polymer topology transformation facilitated by mechanical linking of polymer chains. *Angewandte Chemie International Edition* **2015,** *54* (23), 6770-6774.

236. Wilson, J. A.; Hopkins, S. A.; Wright, P. M.; Dove, A. P., 'Immortal'ring-opening polymerization of ω-pentadecalactone by Mg (BHT) 2 (THF) 2. *Polymer Chemistry* **2014,** *5* (8), 2691-2694.

237. Zimm, B. H.; Kilb, R. W., Dynamics of branched polymer molecules in dilute solution. *Journal of Polymer Science* **1959,** *37* (131), 19-42.

238. Bywater, S., Preparation and properties of star-branched polymers. In *Physical Chemistry*, Springer: 1979; pp 89-116.

239. Walker, J. M.; Bodamer, E.; Kleinfehn, A.; Luo, Y.; Becker, M.; Dean, D., Design and mechanical characterization of solid and highly porous 3D printed poly(propylene fumarate) scaffolds. *Progress in Additive Manufacturing* **2017,** *2* (1-2), 99-108.

240. Le Fer, G.; Luo, Y.; Becker, M. L., Poly (propylene fumarate) stars, using architecture to reduce the viscosity of 3D printable resins. *Polymer Chemistry* **2019**.

APPENDIX

Procedures

Large Batch Synthesis ($\overline{M_n}$=1.27 kDa) Synthesis of Poly(maleic anhydride-co-propylene oxide)

Maleic anhydride (2.856 mol) and propylene oxide (2.856 mol) were dissolved in toluene (0.4 L) in a 2 L round-bottom flask at ambient temperature under nitrogen. After all monomers were dissolved in toluene with magnetic stirring, $Mg(OEt)_2$ (119 mmol; molar ratio of MAn:$Mg(OEt)_2$ = 24:1) was added to the mixture and the flask was moved into a silicone oil bath equipped with a water reflux condenser to start polymerization at 80 °C for 40 h. After the designated polymerization time, the system was cooled to room temperature under nitrogen, evaporated to remove all volatiles and then was diluted with $CHCl_3$, washed with water containing trace amount of HCl to remove the inorganic compound. The organic layer was poured into hexanes after rotary evaporation, and the precipitated polymer mixture was re-dissolved in a minimal amount of $CHCl_3$ that was then concentrated by rotary evaporation. Poly(malic anhydride-co-propylene oxide) was obtained after drying the product under vacuum overnight at room temperature to remove all volatiles, and then the molecular mass and mass distribution properties were characterized by SEC after ^{1}H NMR and ^{13}C NMR characterization (SEC: $\overline{M_n}$ 1200 Da; ^{1}H NMR please see Figure 3.1; ^{13}C NMR shown in Figure S1). ^{13}C NMR (300 MHz,

Chloroform-*d*) δ (ppm): 164.64, 164.63, 164.35; 130.42, 129.92, 129.78, 129.25; 69.15; 66.37; 16.19.

Isomerization of Poly(maleic anhydride-co-propylene oxide)

Diethylamine (0.15 equivalent) was added to poly(maleic anhydride-co-propylene oxide) after dissolving the polymer in $CHCl_3$ (1 mol/L) in a round-bottomed flask equipped with a water reflux condenser to start isomerization at 55 °C for 20 h under nitrogen. The mixture was then concentrated by rotary evaporation and washed with phosphate buffer saline solution (0.5M, pH = 6) to remove the diethylamine. The organic layer was collected after separation and sodium sulfate was added into the organic layer to remove water. The concentrated organic layer was then precipitated into hexanes several times to remove impurities. The precipitate was collected and kept in vacuum overnight at room temperature to remove all volatiles. ^{1}H NMR and ^{13}C NMR were used for characterization (^{1}H NMR please see Figure 3.1; ^{13}C NMR shown in Figure S1). ^{13}C NMR (300 MHz, Chloroform-*d*) δ (ppm): 164.36, 164.35, 164.04, 163.98; 134.01, 133.27; 69.26; 66.58; 16.34.

Figures

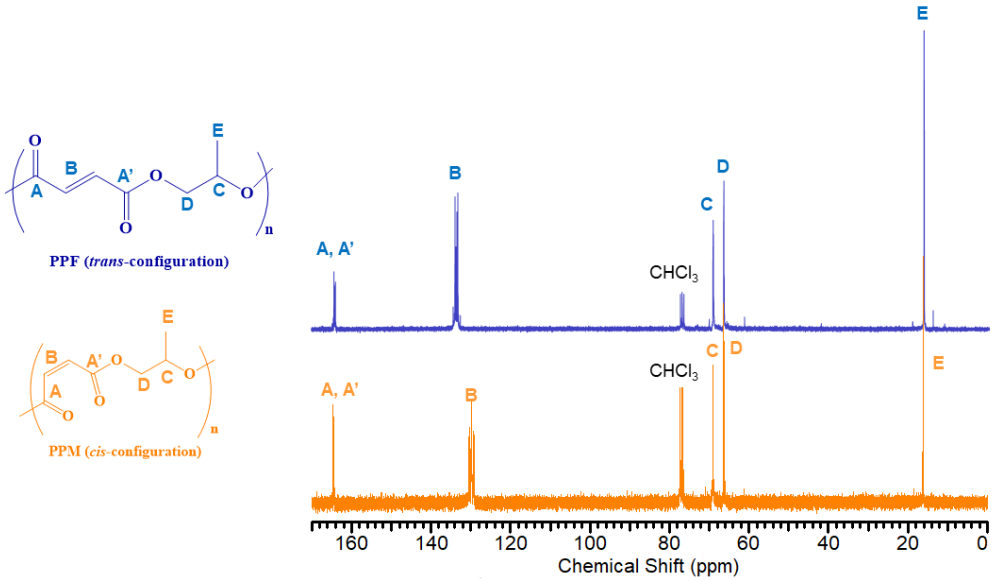

Figure S1. ^{13}C NMR for a poly(propylene malate) (PPM) intermediate and poly(propylene fumarate) (PPF) in Chapter III.

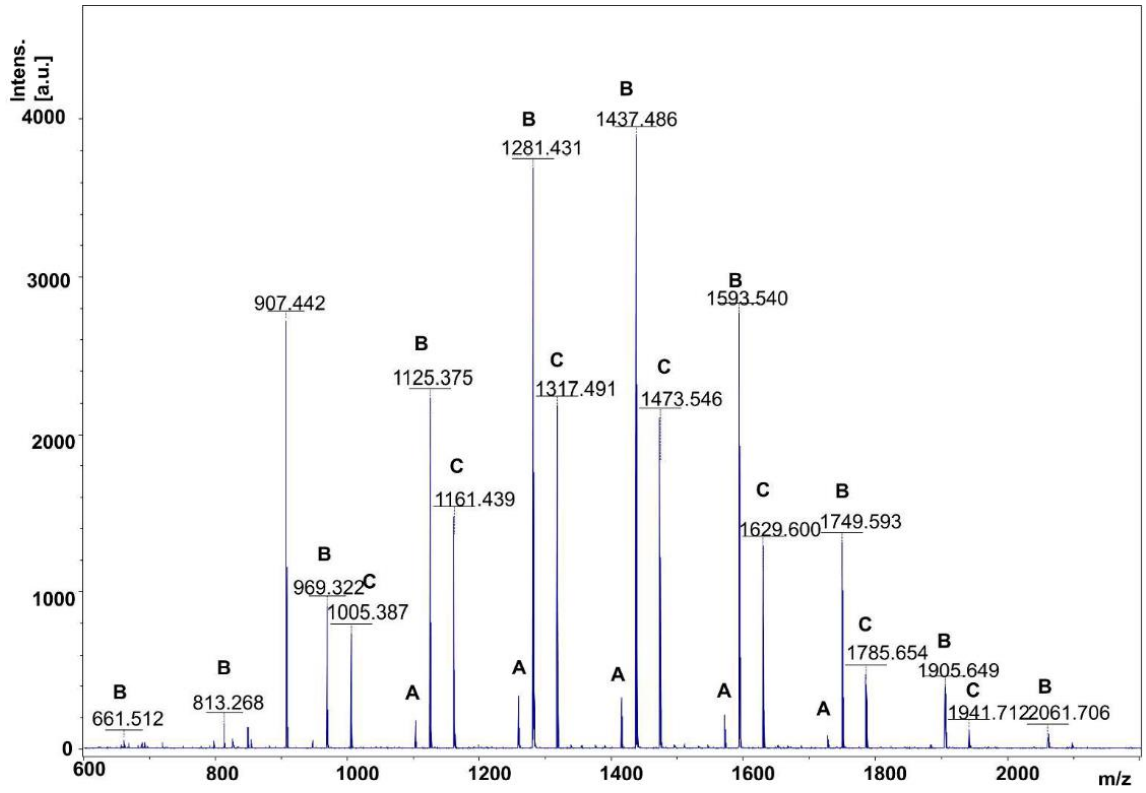

Figure S2. MALDI-TOF mass spectrograph of PPF sample number 3 in Table 3.1 showing mass distribution in this sample.

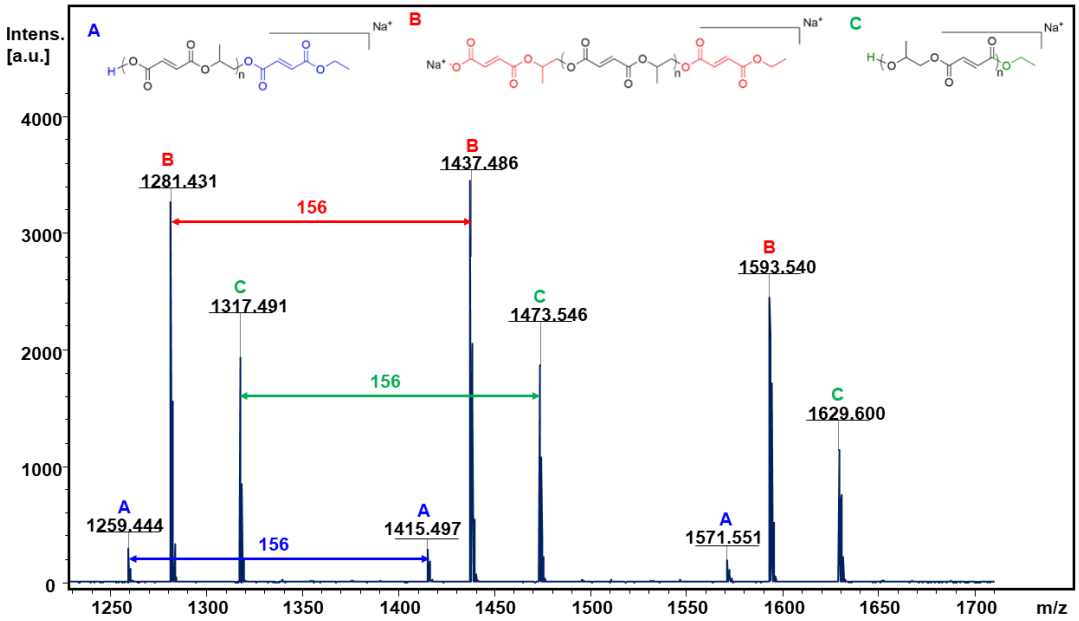

Figure S3. Enlarged portion of a MALDI-TOF mass spectrograph of PPF sample number 3 in Table 3.1 showing the repeat unit in PPF and the possible end group chemistries which correspond the individual peaks in the distribution depicted in the mass spectrometry data.

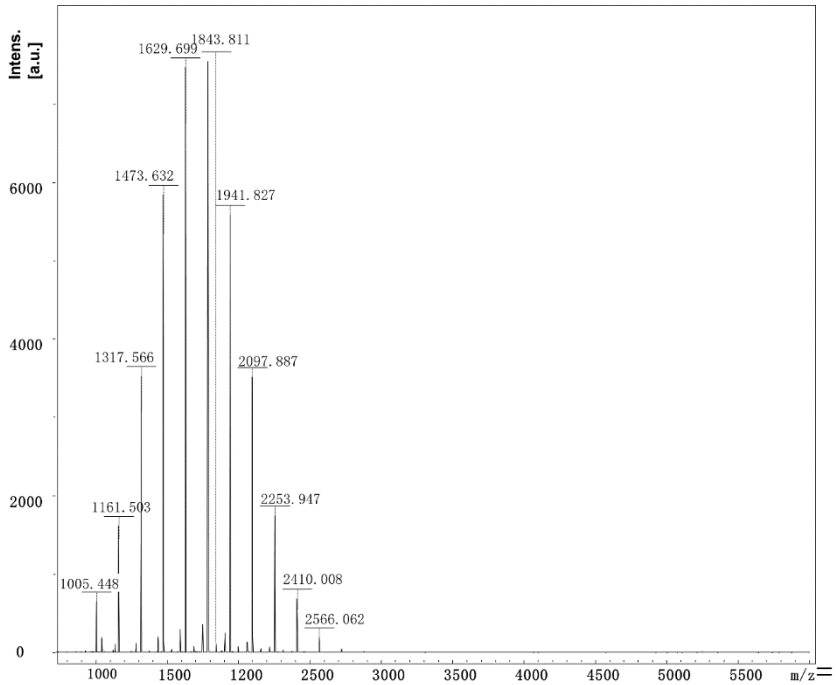

Figure S4. (C) MALDI-TOF mass spectrograph of PPF sample number 4 in Table 3.1 showing mass distribution in this sample.

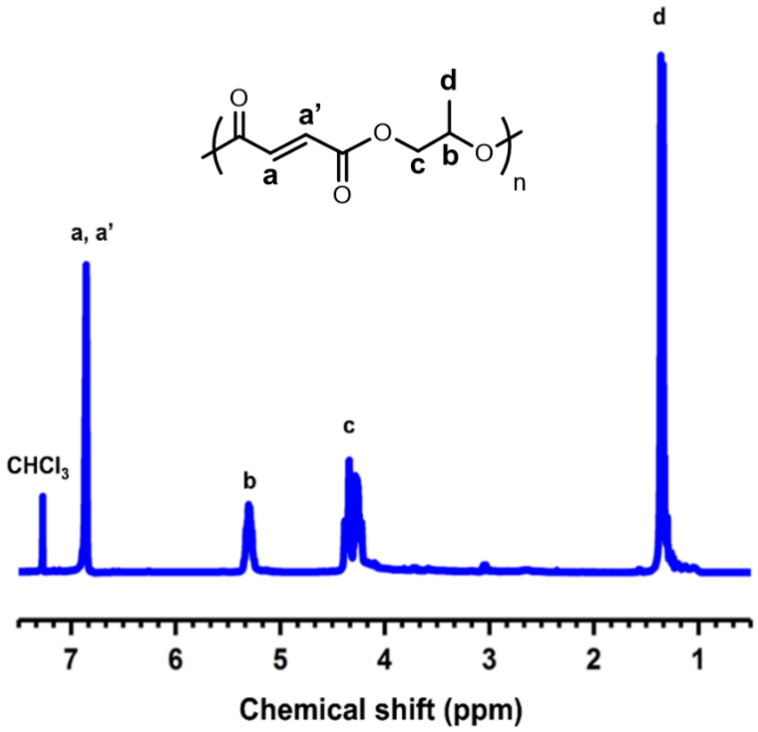

Figure S5. Representative ^{1}H NMR spectrum of poly(propylene fumarate) oligomer (number 1 in Table 4.1)

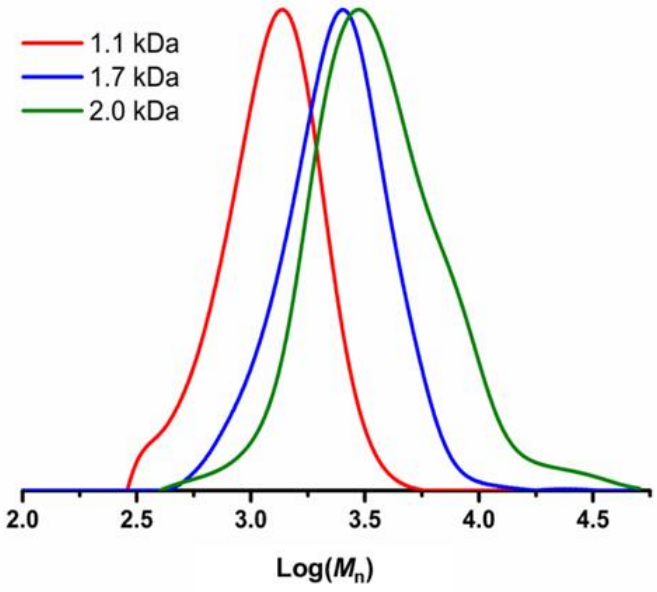

Figure S6. Size exclusion chromatography profiles of poly(propylene fumarate) oligomers (numbers 1, 2 and 3 in Table 4.1).

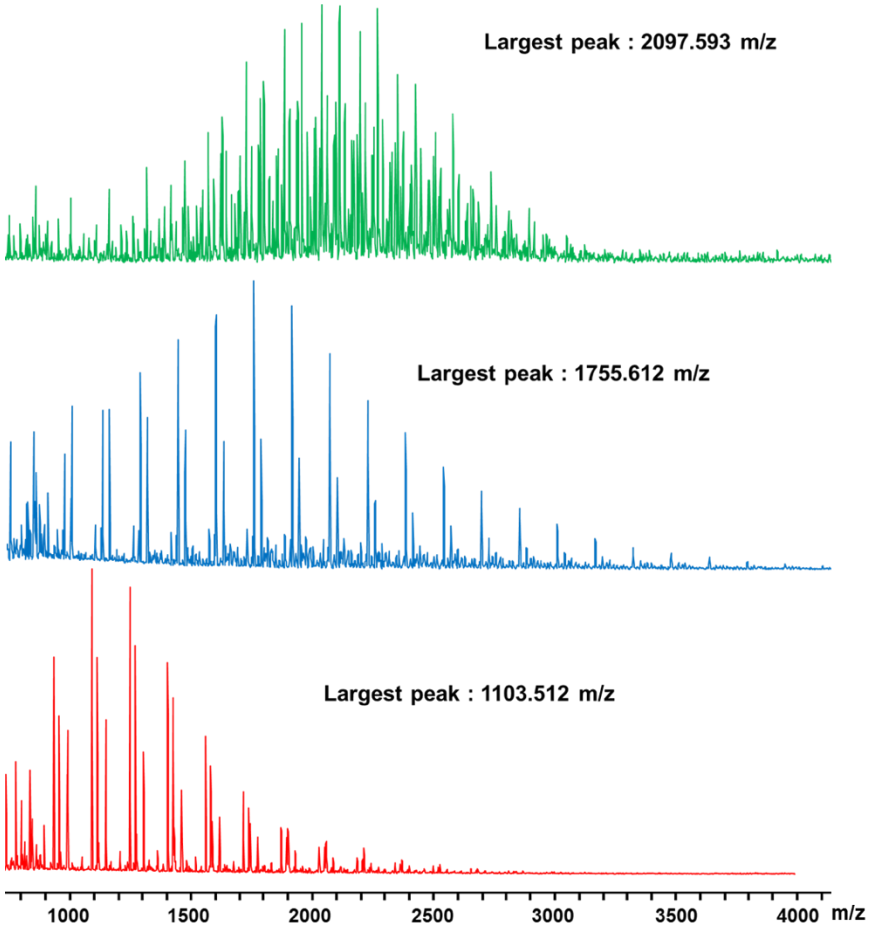

Figure S7. MALDI-ToF spectra of poly(propylene fumarate) oligomers of 1.1 kDa (red), 1.7 kDa (blue) and 2.0 kDa (green) (numbers 1, 2 and 3 in Table 4.1 respectively).

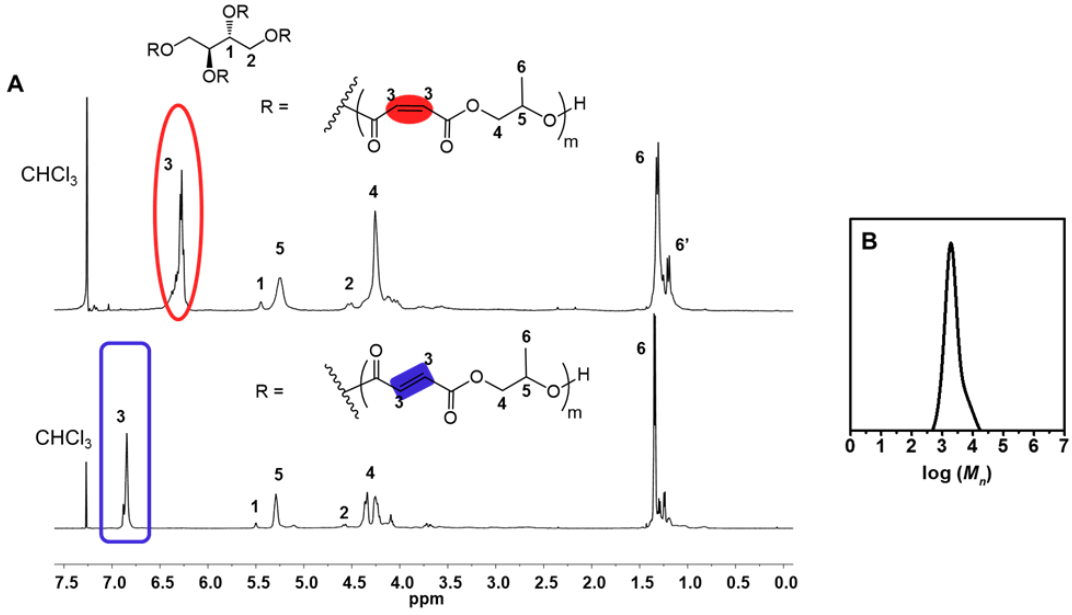

Figure S8. (A) Comparison of ^{1}H NMR spectra of four-arm star poly(propylene maleate) of a total DP20 with a *meso*-erythritol core (top) and corresponding four-arm star poly(propylene fumarate) obtained after isomerization (bottom). (B) Size exclusion chromatography profile of four-arm star poly(propylene maleate) of a total DP20 with a *meso*-erythritol core.

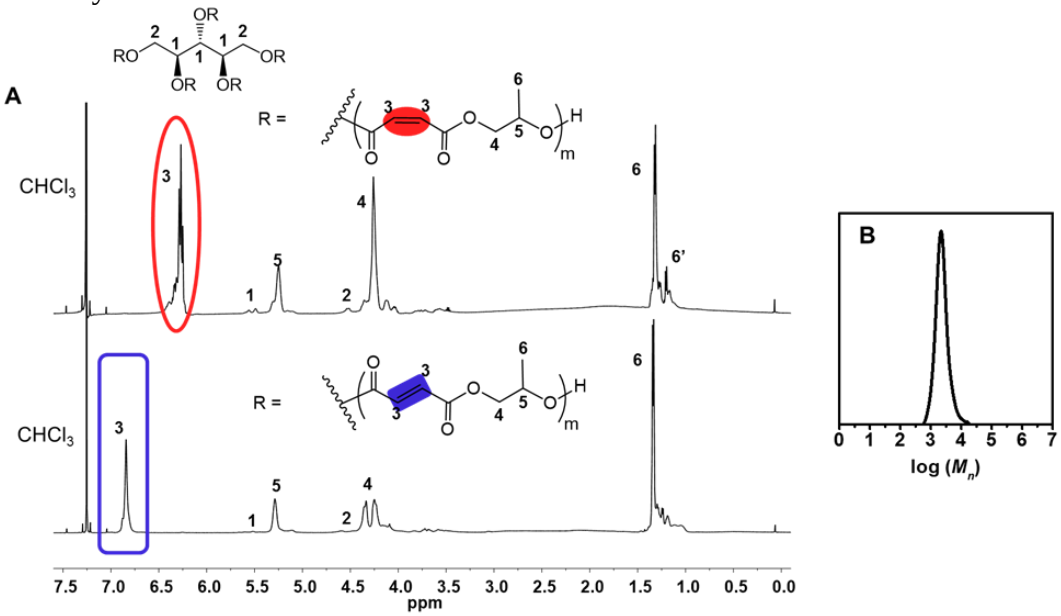

Figure S9. (A) Comparison of ^{1}H NMR spectra of four-arm star poly(propylene maleate) of a total DP40 with a *meso*-erythritol core (top) and corresponding four-arm star poly(propylene fumarate) obtained after isomerization (bottom). (B) Size exclusion chromatography profile of four-arm star poly(propylene maleate) of a total DP40 with a *meso*-erythritol core.

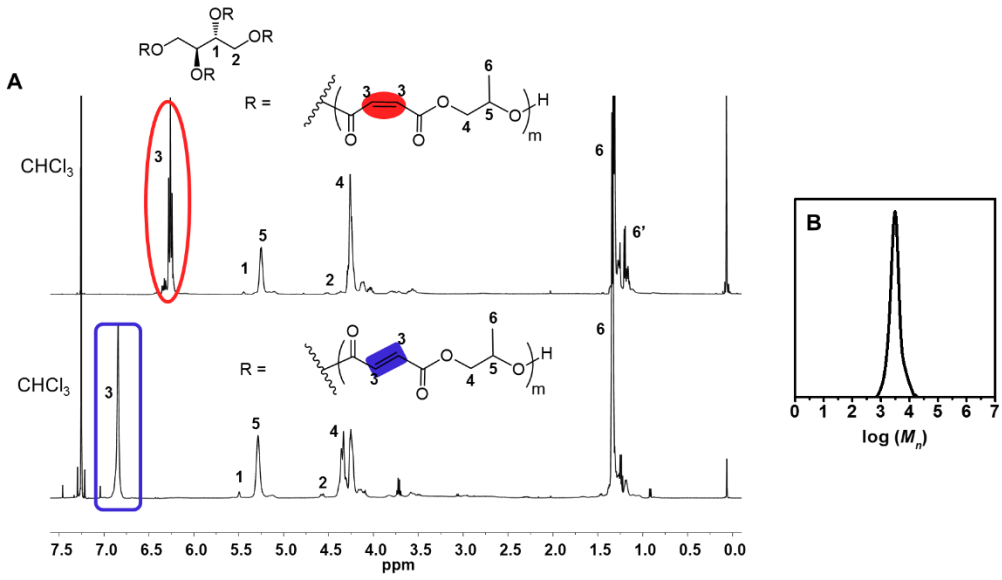

Figure S10. (A) Comparison of ^{1}H NMR spectra of four-arm star poly(propylene maleate) of a total DP80 with a *meso*-erythritol core (top) and corresponding four-arm star poly(propylene fumarate) obtained after isomerization (bottom). (B) Size exclusion chromatography profile of four-arm star poly(propylene maleate) of a total DP80 with a *meso*-erythritol core.

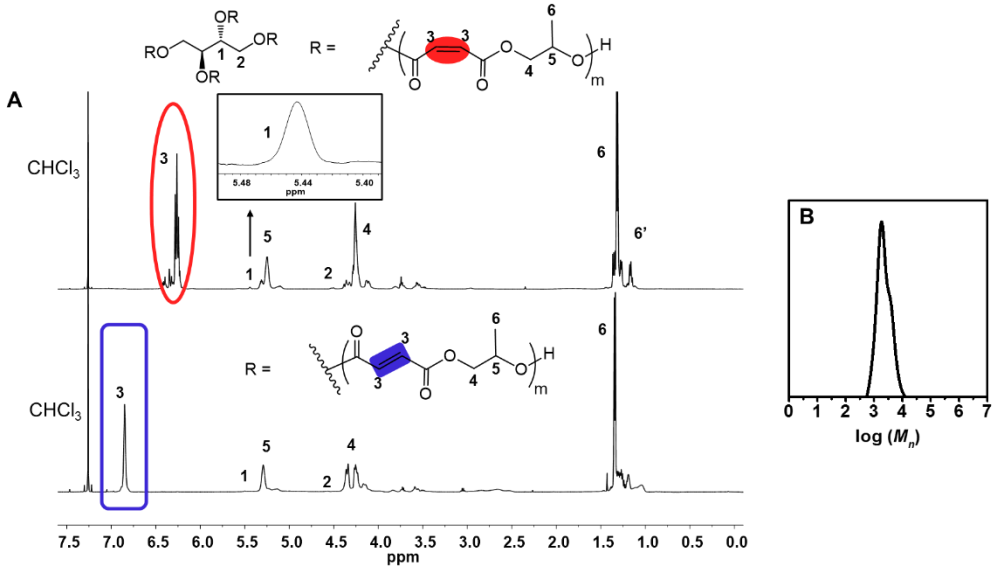

Figure S11. (A) Comparison of ^{1}H NMR spectra of four-arm star poly(propylene maleate) of a total DP120 with a *meso*-erythritol core (top) and corresponding four-arm star poly(propylene fumarate) obtained after isomerization (bottom). (B) Size exclusion chromatography profile of four-arm star poly(propylene maleate) of a total DP120 with a *meso*-erythritol core.

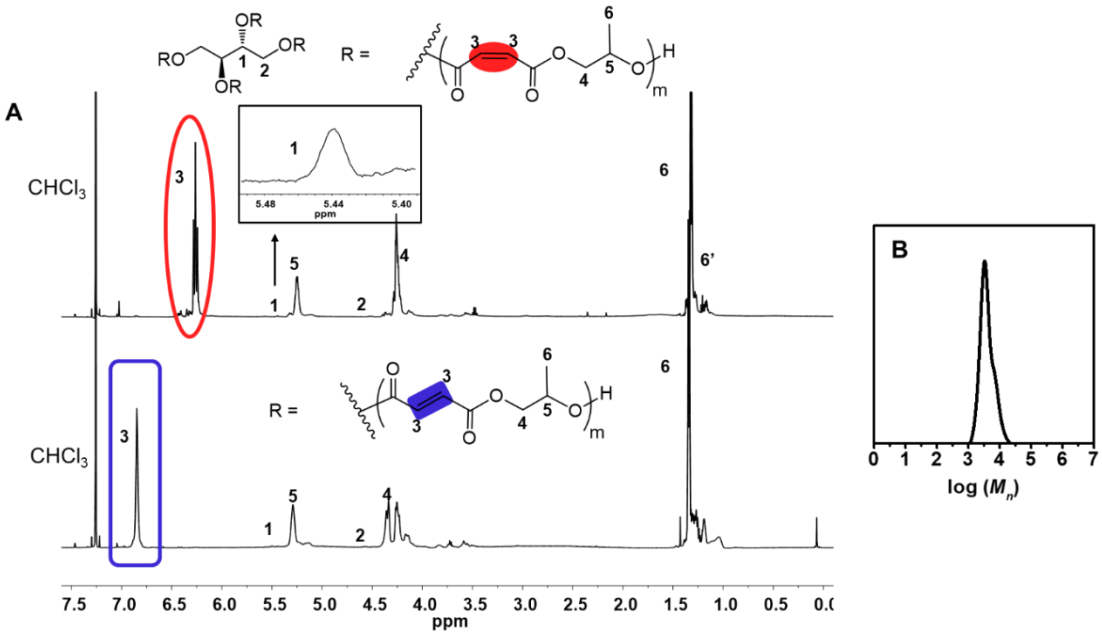

Figure S12. (A) comparison of ^{1}H NMR spectra of four-arm star poly(propylene maleate) of a total DP200 with a *meso*-erythritol core (top) and corresponding four-arm star poly(propylene fumarate) obtained after isomerization (bottom). (B) Size exclusion chromatography profile of four-arm star poly(propylene maleate) of a total DP200 with a *meso*-erythritol core.

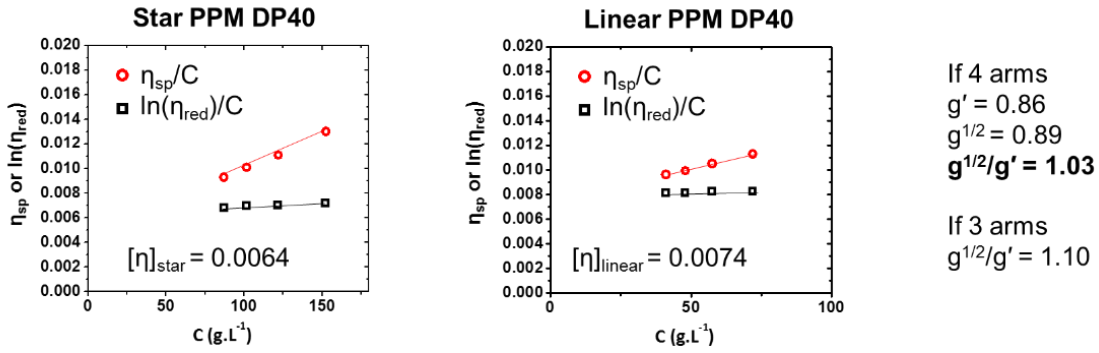

Figure S13. ηsp/c and ln(ηr)/c versus polymer concentration for star PPF DP40 and Linear PPM DP40 solution in THF. Calculation of $g^{1/2}/g'$ ratios corresponding to three or four arms demonstrating the synthesis of four-arm PPF.

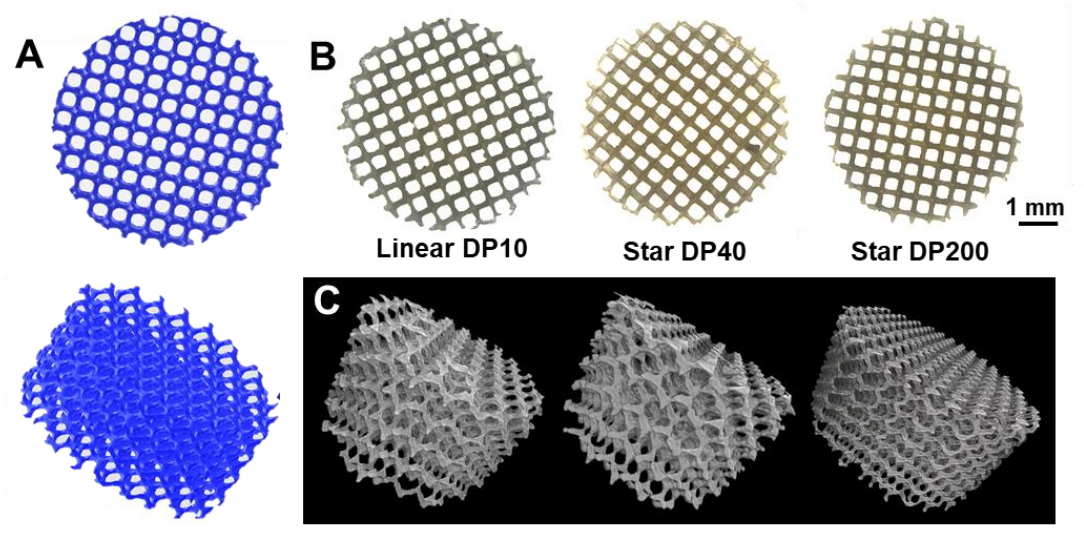

Figure S14. (A) CAD file was created in Matlab using the Schoen gyroid triply periodic minimal surface with 140 μm strut size, 489 μm pore size, and 88.2% porosity. (B) Optical micrographs of the top of the scaffolds obtained from the different PPF (from left to right: linear PPF DP10, star PPF DP40, star PPF DP200). (C) μ-CT images of the scaffolds obtained from the different PPF (from left to right: linear PPF DP10, star PPF DP40, star PPF DP200).

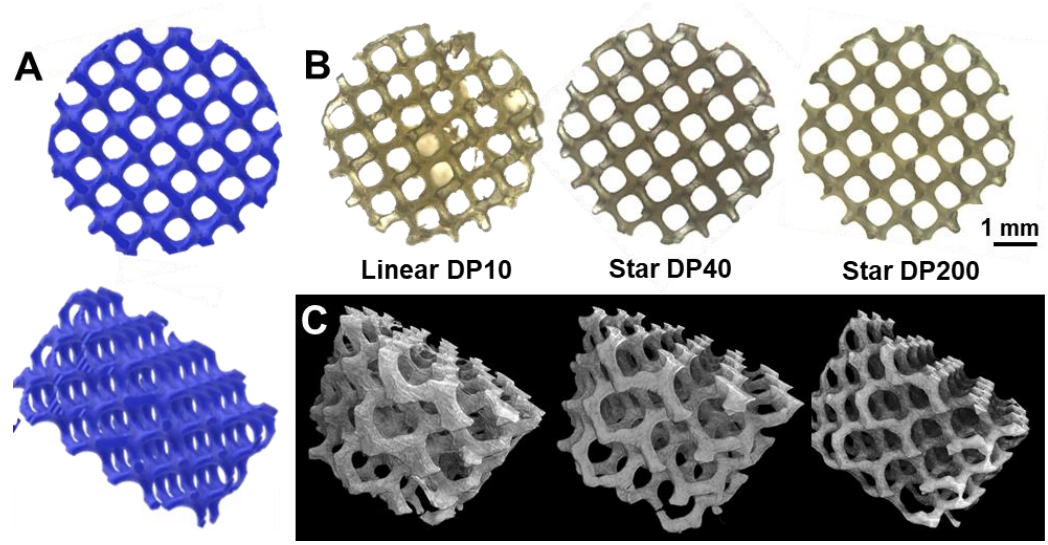

Figure S15. (A) CAD file was created in Matlab using the Schoen gyroid triply periodic minimal surface with 240 μm strut size, 838 μm pore size, and 88.2% porosity. (B) Optical micrographs of the top of the scaffolds obtained from the different PPF (from left to right: linear PPF DP10, star PPF DP40, star PPF DP200). (C) μ-CT images of the scaffolds obtained from the different PPF (from left to right: linear PPF DP10, star PPF DP40, star PPF DP200).

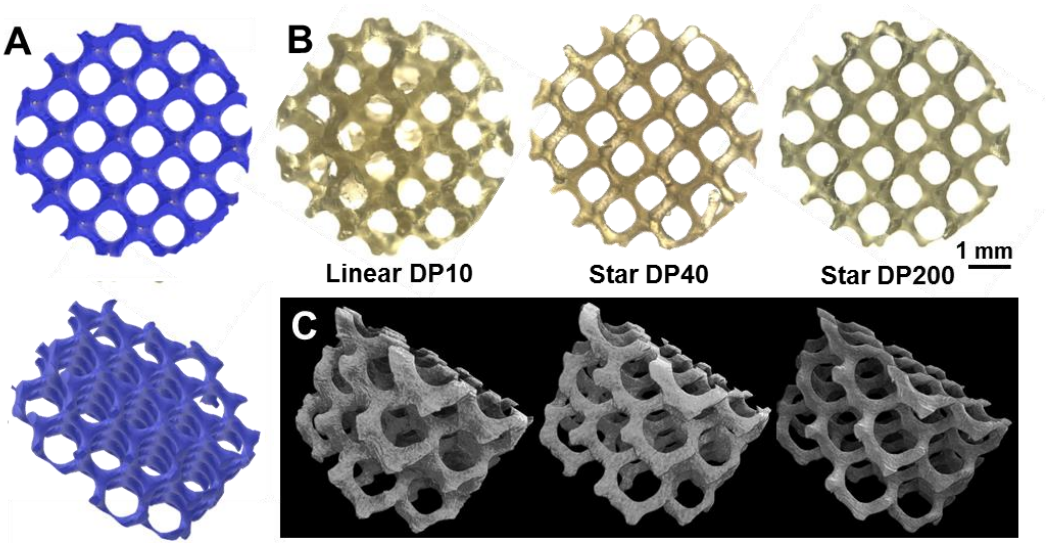

Figure S16. (A) CAD file was created in Matlab using the Schoen gyroid triply periodic minimal surface with 280 μm strut size, 978 μm pore size, and 88.2% porosity. (B) Optical micrographs of the top of the scaffolds obtained from the different PPF (from left to right: linear PPF DP10, star PPF DP40, star PPF DP200). (C) μ-CT images of the scaffolds obtained from the different PPF (from left to right: linear PPF DP10, star PPF DP40, star PPF DP200).